Chemical Vapour Deposition of Large Area Graphene

Larsen, Martin Benjamin Barbour Spanget

Publication date:
2015

Document Version
Publisher's PDF, also known as Version of record

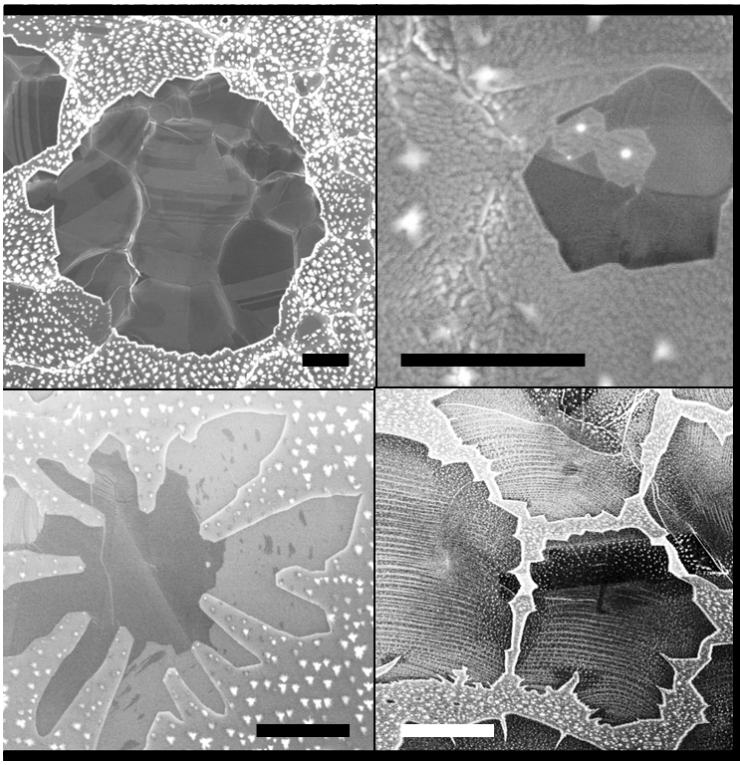

Chemical Vapor Deposition of Large Area Graphene

Martin Benjamin Barbour Spanget Larsen
PhD Thesis June 2015

DTU Nanotech
Department of Micro- and Nanotechnology

Technical University of Denmark

PhD Thesis

Chemical Vapor Deposition of Large Area Graphene

Martin Benjamin Barbour Spanget Larsen

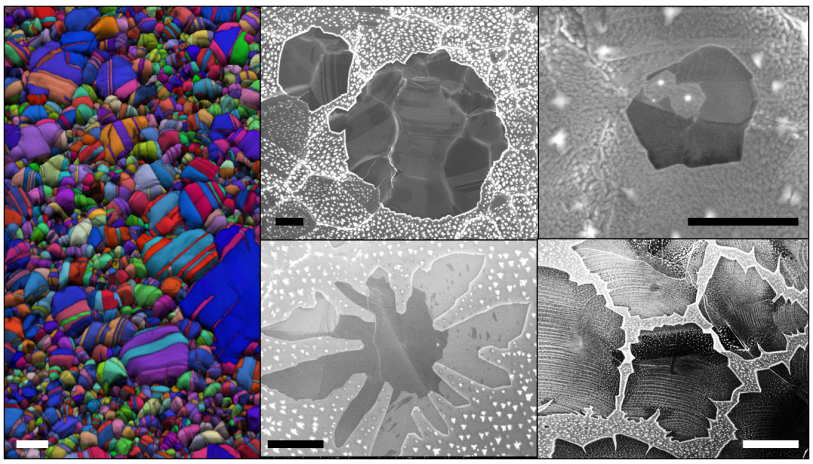

Supervisors:
Peter Bøggild
Timothy J Booth
Anders M Jørgensen

DTU Nanotech
Department of Micro- and Nanotechnology

Preface

This thesis has been written as a partial fulfillment of the requirements for obtaining the PhD degree at the Technical University of Denmark. The PhD project has been conducted at DTU Nanotech and DTU Danchip in the period from June 2011 to June 2014.

The project has been carried out in the NanoCarbon group and has been supervised by the following people:

Professor, PhD Peter Bøggild Main supervisor for the duration of the project

Researcher, Dr. Timothy John Booth Co-supervisor for the duration of the project

Vice Director of DTU Danchip, PhD Anders Michael Jørgensen Co-supervisor for the duration of the project

This thesis encompasses an introduction to optimization of chemical vapor deposited graphene, the characterization techniques used, and a summary of the results obtained during the project. The results are partially based on the submitted manuscripts, but also includes unpublished results.

The project has been financed by DTU Danchip and DTU Nanotech, as a technological PhD.

Abstract

Chemical Vapor Deposition (CVD) is a viable technique for fabrication of large areas of graphene. CVD fabrication is the most prominent and common way of fabricating graphene in industry. In this thesis I have attempted to optimize a growth recipe and catalyst layer for CVD fabrication of uniform, single layer, and high carrier mobility large area graphene.

The main goals of this work are; (1) explore the graphene growth mechanics in a low pressure cold-wall CVD system on a copper substrate, and (2) optimize the process of growing high quality graphene in terms of carrier mobility, and crystal structure. Optimization of a process for graphene growth on commercially available copper foil is limited by the number of aluminium oxide particles on the surface of the catalyst. By replacing the copper foil with a thin deposited copper film on a SiO_2/Si or c-plane sapphire wafer the particles can be eliminated. Further opportunities arise when exchanging the copper foil for copper thin film on a wafer e.g. better integration with current cleanroom processing of devices and better control over the copper crystallinity.

Typical strategies for controlling the temperature during CVD fabrication of graphene are proportional, integral, and derivative (PID) controllers. The PID controller in a CVD system works off feedback temperatures from a thermocouple. The thermocouples used in this work suffer from degradation at the temperatures and the hydrogen gasses needed for high quality graphene growth. The degradation of thermocouples leads to large variations in the grown graphene. This was solved by controlling the temperature through applying a set power to the heat source, resulting in a more stable temperature from process to process.

Micro Raman spectroscopy is used to characterize the structural quality of the grown graphene on the copper surface as well as after a transfer process

to a SiO_2 substrate. Raman mapping is especially suited for uniformity characterization on a scale of a few to hundreds of microns. In this work the ratios of the 2D- and G-peak, and the ratio of the D- and the G peak are used as measures of crystalline quality of the CVD grown graphene.

I have also used spatially resolved micro Raman spectroscopy to map the full width at half maximum (FWHM) of the graphene G-band and the 2D and G peak positions, for as-grown graphene on copper catalyst layers, for transferred CVD graphene and for micro-mechanically exfoliated graphene. This was done to characterize the effects of a transfer process on the graphene properties. The FWHM(G) to indicate the doping level of graphene, and the ratio of the shifts in the 2D and G bands as an indicator of strain. The transfer process introduces an isotropic, spatially uniform, compressive strain in graphene, and increases the carrier concentration.

Copper foil was found to exhibit a polycrystalline surface with a predominantly Cu(001) orientation, through electron backscatter diffraction mapping. Copper thin film deposited on a SiO_2/Si wafer display a polycrystalline nature with the Cu(111) orientation dominating, when the crystals increase in size. Copper thin film sputtered on a c-plane sapphire wafer shows almost single crystal formation of Cu(111) across a 4 inch wafer.

The polycrystalline nature of a thin copper film on a SiO_2/Si wafer was investigated through annealing. A variation in the annealing temperature was found to have a significant effect on the crystal size, while the annealing time was found to have little effect on the crystal sizes.

Electronic hall-bar devices were fabricated from CVD graphene grown on copper foil, copper on SiO_2/Si wafers, and copper on sapphire wafers. Preliminary results show the highest carrier mobility was achieved from graphene grown on copper on sapphire, while graphene grown on copper foil showed the lowest carrier mobility.

List of appended papers

This thesis is based on the work contained in the following paper:

Transfer induced compressive strain in graphene : Evidence from Raman spectroscopic mapping. Larsen, Martin Benjamin Barbour Spanget; Mackenzie, David; Caridad, Jose; Bøggild, Peter; Booth, Timothy John.
Microelectronic Engineering, Vol. 121, 2014, p. 113-117.

Other papers that are outside of the scope of this thesis

The following papers are not included in this thesis because they are beyond the scope of this thesis:

Non-destructive Electrochemical Graphene Transfer from Reusable Thin-Film Catalysts. Filippo Pizzocchero, Bjarke S. Jessen, Patrick R. Whelan, Natalie Kostesha, Sunwoo Lee, Jonas D. Buron, Irina Petrushina, Martin B. Larsen, Paul Greenwood, Wu Joon Cha, Ken Teo, Peter U. Jepsen, James Hone, Peter Bøggild, Timothy J. Booth.
Carbon, Volume 85, April 2015, Pages 397–405
Contribution: Performed Raman experiments, as well as assisting in the writing of the article.

Plasmon–Phonon Coupling in Large-Area Graphene Dot and Antidot Arrays Fabricated by Nanosphere Lithography. Zhu, Xiaolong; Wang, Weihua; Yan, Wei; Larsen, Martin Benjamin Barbour Spanget; Bøggild, Peter; Pedersen, Thomas Garm; Xiao, Sanshui ; Zi, Jian; Mortensen, N. Asger.
Nano Letters, Vol. 14, No. 5, 2014, p. 2907–2913.
Contribution: Performed Raman experiments, as well as assisting in the writing of the article.

CVD graphene growth on non-planar surfaces, a pilot investigation. Stoot, Adam Carsten; Christiansen, Alexander Bruun; Larsen, Martin Benjamin Barbour Spanget; Bøggild, Peter.

Proceedings of Graphene 2014.
Contribution: Assisted with Raman measurements, fabrication ideas, as well as assisting in the writing.

Large area THz imaging of electrically controlled graphene conductance. Møller, Morten; Buron, Jonas Christian Due; Larsen, Martin Benjamin Barbour Spanget; Bøggild, Peter; Mackenzie, David; Pizzocchero, Filippo; Booth, Tim ; Jepsen, Peter Uhd.
Abstract from International Workshop on Optical Terahertz Science and Technology (OTST 2013), Kyoto Terrsa, Japan.
Contribution: Provided CVD graphene samples, performed Raman experiments, as well as assisting in the writing.

Contents

Chapter 1

Introduction

In 2004 the discovery of the one-atom thin and thermodynamically stable single layer graphene [87] started many new theoretical and experimental studies, including measurements of room temperature quantum Hall effect [89]. The high mobility and ballistic transport [88] [133] of electrons and holes in graphene makes it a great candidate for future nano-electronic devices [15] [42] [66] [105]. Furthermore graphene has outstanding mechanical strength, chemical stability, and optical transparency. By exploiting the weak Van Der Waals forces between graphene layers in graphite it is possible to isolate a single layer of graphene in a process called micro-mechanical exfoliation or the Scotch tape method. These sheets of graphene can be on the order of 10's to 100's of µm across. In order to exploit these fantastic properties we need to be able to mass produce large areas of uniform graphene with predictable characteristics. Prototype devices with small flakes made from exfoliation, are a valuable method for examining the intrinsic properties of perfect graphene. Micro-mechanical exfoliation is still the best way to fabricate near perfect graphene flakes, and devices. Large area fabrication techniques are the best in terms of cost, with some techniques gaining momentum in terms of quality, specifically chemical vapor deposition (CVD). Graphene has the potential to be ground breaking in many applications such as transparent electronics as a much cheaper alternative to the expensive and relatively rare indium tin oxide (ITO), high speed electronics as a replacement for silicon or III-V semiconductors due to increased mobility, flexible electronics, where metals and silicon are not suited, robust transparent membranes due to its high strength and transparency, as well as industrial coatings for corrosion resistance due to its chemical inertness

etc. [105]. But for all of these applications to come to fruition one major challenge has to be overcome, which is size and reproducibility of a sheet of graphene. Without these two major points, graphene doesn't stand a chance of replacing e.g. silicon for electronic components or indium tin oxide as a transparent electrode.

For high quality graphene (continuous sheet with no defects) to be fabricated on a large scale via e.g. CVD processing, a catalytic substrate is needed. CVD fabrication of graphene has been proposed on a variety of materials, though most common metal substrates are copper[14] [68] [60], nickel [14] [80] [92], and platinum [37]. The different catalytic substrates have been found to promote two kinds of graphene growth processes. On copper the process is surface limited [122], due to the low solid solubility of carbon in copper. On e.g. nickel and platinum the solid solubility of carbon is much higher, giving rise to both a surface reaction as well as absorption/precipitation of carbon during the processing. It has been found that CVD fabrication of graphene on a copper surface is a self terminating process, meaning that once a mono layer of graphene is formed on the copper, the growth of graphene stops [135]. Introduction of surface roughness or particles on the surface of the copper substrate can be a source of few layer graphene regions [45].

Graphene grown for high speed electronic devices needs two important factors, high mobility of electrons/holes at room temperature and the presence of a band gap [105]. The band gap is needed for switching the device on and off. The carrier mobility is perhaps the most important measure of quality in graphene. The product of mobility and carrier concentration is proportional to the conductivity. A transistor needs a semi-conductor for switching the current on and off, and typically the number of available electrons in a semi-conductor is low meaning that the mobility needs to be high to compensate. The symmetric electron-hole band structure of graphene can be directly confirmed in the resistance versus gate voltage curve, see figure 1.1 (A). The gate voltage varies the Fermi level of graphene relative to the Dirac point, see figure 1.1 (B). The energy band has no gap since the conduction and valence bands touch at the Dirac point (also called charge neutrality point (CNP)), where effective carrier density is zero, see figure 1.1 (B) center. If the Fermi energy is above, electrons are the major carriers (n doping), in figure 1.1 (B) right, and if the Fermi energy is below the Dirac energy, the majority carriers are holes (p doping), in figure 1.1 (B) left. Characterizing carrier mobility in graphene is commonly done through

electrical devices, i.e. graphene field effect transistors (GFETs), see figure 1.2.

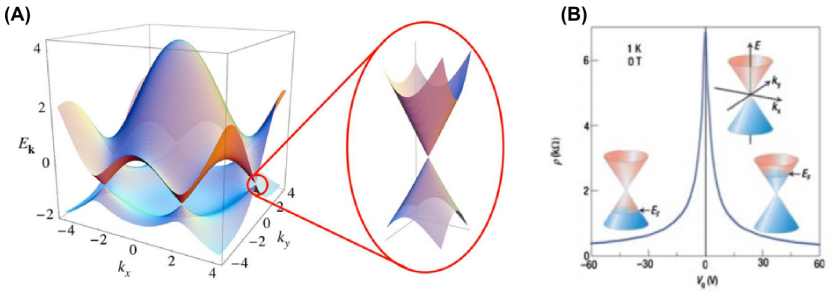

Figure 1.1: (A) Left: the band structure of graphene in the honeycomb lattice. Right: zoom-in of the energy bands close to one of the Dirac points (reprinted from Castro Neto et al, Rev. Mod. Phys. 81, 109 (2009)). (B) Ambipolar electric field effect in single-layer graphene. The insets show the position of the Dirac point and the Fermi energy E_F of graphene as a function of gate voltage (reprinted from A. K. Geim and K. S. Novoselov, Nat. Mater. 6, 183 (2007)).

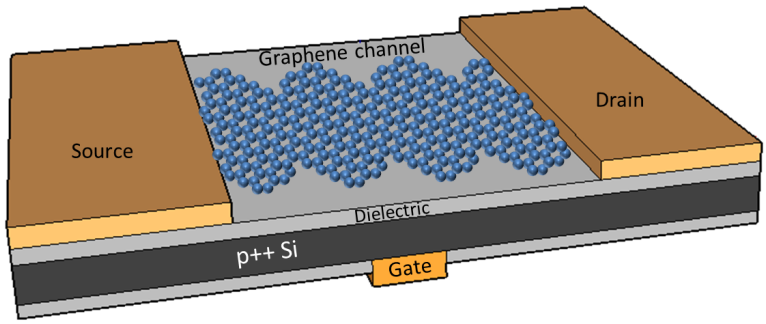

Figure 1.2: Schematic showing a theoretical back-gated graphene metal-oxide-semiconductor field-effect transistor (MOSFET).

A GFET device is characterized by applying a potential across the source drain electrodes (V_{DS}, and measuring the current (I_{DS}), while changing the gate potential (V_{gate}). The gate potential changes the the carrier density

in the devices material (in this case graphene). In order to get meaningful measurements a few obstacles have to be overcome. Growing single layer graphene via CVD on a copper substrate is the first task. Then the graphene must be transferred to an insulating substrate, in order to remove the electronic influence of the metal catalyst on which the graphene is grown. Then the transferred graphene has to be patterned by means of a lithographic technique e.g. photolithography, e-beam lithography, laser ablation. The typical process is very similar to the method used in [87], where exfoliated graphene is processed into multiterminal Hall bar devices on a SiO_2/Si substrate, but with CVD graphene instead of exfoliated graphene. Then metal contacts should be added to the patterned graphene, this is can be done by e.g. a lift-off process. Then a top- or back-gate must be added to the device. Finally the devices can be measured for carrier mobility. This device is analogous to a MOSFET, except graphene is ambipolar compared to silicon, which is bipolar. The change in resistance of the graphene as a function of back gate potential relates to the conductance of the graphene. The mobility μ_{FE} can be extracted from the conductance through the following equation for the intrinsic transconductance (g_m):

$$g_{\mathrm{m}} = \frac{dI_{\mathrm{D}}}{dV_{\mathrm{gate}}} \tag{1.1}$$

where $\frac{dI_D}{dV_{gate}}$ is the change in drain current divided by the change in gate potential for constant drain potential (V_D), and the mobility can be written as,

$$\mu_{\mathrm{FE}} = \frac{l\, g_{\mathrm{m}}}{w\, C_{\mathrm{G}}\, V_{\mathrm{DS}}} \tag{1.2}$$

Where l and w are the length and widths of the graphene channel, and C_G is the gate capacitance per unit area.

Fabrication of electrical devices through all the steps of the graphene growth optimization, is avoided. The optimization and characterization has been focused on the structural quality of the graphene rather than the complete device quality. For this reason the optimization is carried out using the following assumptions: 1. The lower the defect density the higher the potential mobility [52]. 2. Large graphene crystal sizes results in higher graphene coverage after transfer, as well as reducing the amount of negative effects grain boundaries have on the electrical properties [37]. 3. Point 1 and 2 can be characterized on the copper substrate using scanning electron microscopy

and Raman spectroscopy. Using these assumptions, provides a basis for optimizing graphene growth before having an optimized recipe for transferring graphene from a copper substrate to an insulating one. The fabrication of devices can be carried out once these two processes are optimized.

1.1 State of the Art Graphene Devices

Measurements of the electronic properties of graphene have shown electron mobilities of 40000 cm^2/Vs and high thermal conductivity of 600 $Wm^{-1}K^{-1}$, both much greater than typical semiconductors and metals, see table 1.1.

Material	Electron mobility [cm^2/Vs]	Hole mobility [cm^2/Vs]
Si	1417	471 [103]
Ge	3900	1900 [103]
GaAs	8800	400 [103]
Graphene	100.000	100.000 [78]
CVD Graphene	45000	45000 [93]

Table 1.1: Table showing a comparison of room temperature carrier mobility measurements for typical semiconductors used for high speed electronics and graphene.

A novel way of fabricating graphene devices negating a transfer process is shown in [67]. Here they build devices directly on the carrier wafer using the catalyst copper layer as an electrode. Devices are defined by patterning the copper with a lithographic procedure and etching away the unwanted copper, leaving copper where contacts are wanted. Individual graphene crystals up to 1.9 by 0.8 mm have been reported grown via CVD on Cu foil [116].

In 2013 Samsung debuted a flexible mobile phone with a few layer graphene based touch screen display at the Consumer Electronic Show (CES) [119]. This year Samsung fabricated a working mobile phone prototype using a CVD graphene touch screen display, comparable to a common Indium-Tin-Oxide (ITO) screen [100].

1.2 Motivation

Since the discovery of graphene there has been a desire to increase the area of flakes by either optimizing the exfoliation process, by thermal decomposition of SiC, via chemical vapor deposition, or using a chemical approach. By increasing the area of graphene, large scale production of devices would be possible, thereby reducing cost per device and making graphene a viable candidate for high speed electronic components, transparent conducting layers and high strength membranes etc. Using chemical vapor deposition for fabrication of these large area sheets of graphene has already been shown possible in 2010 for making transparent electrodes from a 30 inch sheet of graphene [4]. This shows that scaling up of graphene is obtainable using CVD processing. I will show that by using the Black Magic (BM) 4" CVD system it is possible to grow full coverage, single layer graphene on copper thin films on both SiO_2/Si and sapphire (0001) wafers. Growing graphene on thin metal films, on wafers, is an important step towards high quality large area graphene films. This is because it solves some of the issues found in graphene growth on copper foils e.g. particle contamination and surface roughness.

Growing graphene via CVD on a copper foil/film has shown that a polycrystalline film is grown on the Cu surface. This raises a few questions about the surface morphology of the Cu such as: Does the graphene crystal size depend on the Cu crystal size? Does the growth rate and defect density, depend on the Cu crystal facet as described in [122]? The study claims that Cu(111) produces pristine monolayer graphene with higher growth rate than Cu(100) containing facets.

If the crystal structure of the copper surface plays an important role in the growth mechanics of CVD graphene, then it is necessary to be able to control this parameter. In this project I will describe a few techniques for controlling the crystal structure of a copper film by either controlling the annealing parameters or changing the support wafer for a copper thin film.

Hypotheses

The outset for this project was to answer the following hypotheses:

1a. *It is possible to grow large area graphene via CVD on copper with a carrier mobility approaching that of mechanically exfoliated graphene.*

2a. *The defect density and growth rate depend on the different crystal orientations of the copper catalyst.*

3a. *It is possible to change the shape of the CVD grown graphene flakes by changing the growth conditions.*

4a. *The size and shape of CVD grown graphene flakes depend on the catalyst nucleation site (edge/plane/particle).*

It was found out through optimization of graphene films on copper foils that the surface morphology and cleanliness would not provide the best surface for graphene growth. Instead the main objective of this project was changed to growth of graphene on copper thin films on 4-inch SiO_2/Si and sapphire wafers. Copper thin films do not pose the same issues as copper foils in terms of particles and surface roughness, since the copper is deposited using a high purity source forming a smooth film. Cu thin films on Si wafers integrate well with current wafer scale device fabrication, since they can be scaled to fit with every size of wafers. Growth of graphene on thin copper films on wafers pose other hypotheses:

1b. *The copper grain sizes and orientation depends on the surface energy between the carrier wafer and the deposited copper thin film and the annealing temperature.*

2b. *The defect density of CVD graphene is dependent on the growth parameters e.g. temperature and gas flow.*

3b. *The graphene crystal size depends on the catalyst domain size.*

4b. *The defect density and growth rate depend on the different crystal orientations of the copper catalyst.*

1.3 Fabrication techniques

Since graphene has such a variety of outstanding properties, from mechanical strength, optical transparency, to electrical mobility etc, exfoliation of graphite to graphene might not always be the optimal fabrication scheme for a particular device or purpose. In this section I will describe the most common methods for fabrication of graphene: Mechanical exfoliation, epitaxial growth from SiC, chemical vapor deposition, and chemical production of reduced graphene oxide.

1.3.1 Mechanical Exfoliation

Mechanical exfoliation, colloquially known as the Scotch Tape method, is a technique, where graphite layers are peeled apart using an adhesive tape and placed on a substrate [38]. This technique exploits the weak van der Waals interaction between the graphite layers and the repeated splitting of the layers to form a single layer on a substrate. This method makes graphene one of the most expensive materials per kilogram on Earth (Graphene-supermarket.com). Mechanical exfoliation works on a very small scale with random placement as seen in figure 1.3, but has the highest crystal quality of the different kinds of fabrication methods, due to the high quality graphite used and lack of a transfer procedure. Mechanical exfoliation produces graphene on insulator, which allows for a relatively simple fabrication scheme (without the need for a transfer procedure), when making electronic devices.

Mechanical exfoliation is still used today as the basis for prototype devices, such as gas sensors [128] [72] [102], high speed transistors [16] [104] [70], etc, where single devices can be fabricated using electron beam lithography and metal deposition for contacting the device. In order to achieve high mobilities with exfoliated graphene both the flatness to avoid the graphene to be corrugated, as well as absence of charge traps, as well as absence or low level of electron phonon interactions is important to avoid scattering and diminishing of graphenes otherwise high mobility. A special substrate e.g. hexagonal-boron nitride (hBN), or no substrate at all as in suspended graphene can help achieve the highest carrier mobility. The cleanliness of the graphene also plays a large role in the achievable mobility, where polymer residues can affect the doping level.

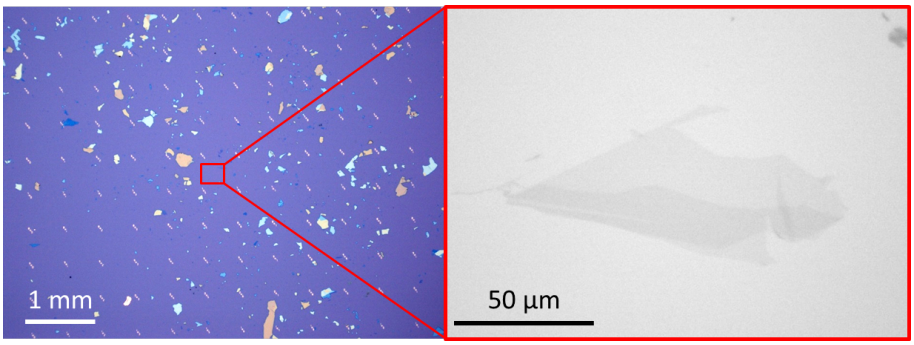

Figure 1.3: Optical microscope images of exfoliated graphite and graphene on a 100 nm SiO_2/Si substrate, at 10x (left) and 100x (right) magnification. Courtesy of Timothy J Booth.

1.3.2 Epitaxial Growth

Epitaxial growth is a technique which involves thermal desorption of silicon, from a silicon carbide substrate at very high temperatures (above 1500 ^{o}C [91]) and ultra high vacuum (UHV) ($5 \cdot 10^{-9}$ mbar)[49], which then forms a graphene layer on the surface [98]. The high temperature and low pressure makes this technique very expensive for production, and the mobility does not come close to that of mechanically exfoliated graphene. Due to the high temperature it is not possible to incorporate in to CMOS fabrication, and the graphene has a very high stiction to the underlying silicon carbide substrate, which makes transfer of the graphene complicated.

Graphene field-effect transistors (FETs) from SiC have reached a frequency of 100 GHz, which is more than twice that of Si based FETs (40 GHz) with the same channel dimensions [70]. The SiC based graphene can achieve mobilities of μ = 29.000 cm^2/Vs at T = 25 K when gated near the charge neutrality point [55], though often observed between 2000 and 10000 cm^2/Vs [91] [55] [43]. The observed mobilities of graphene from SiC are even lower than what can be achieved from CVD graphene on hexagonal boron-nitride at room temperature conditions in ambient atmosphere (μ = 40.000 cm^2/Vs at T = 300 K) [25].

1.3.3 Chemical Vapor Deposition of Graphene

Chemical vapor deposition is a semiconductor micro-fabrication technique for depositing high quality and high purity solid thin films on wafers substrates. In a typical CVD process the substrate is exposed to one or more

volatile precursor gasses, which form a solid layer by either reacting with or decomposing on the surface. By using a CVD process it is possible to deposit amorphous, poly- or single crystalline or epitaxial thin films on a wafer surface. There are many kinds of CVD processes, ranging from low pressure to atmospheric pressure to plasma enhanced deposition. In this thesis low pressure (1 - 100 mbar) CVD is used to deposit graphene on metal catalysts by introducing a carbon containing precursor gas at high temperatures to the catalyst material. The system used for this process is the cold wall Aixtron Black Magic Pro 4 inch CVD system (BM). A schematic showing the CVD graphene growth process is found in figure 1.4. More details concerning the graphene growth kinetics can be found in section 1.7 and details about the BM system is found in chapter 2 (Chemical Vapor Deposition).

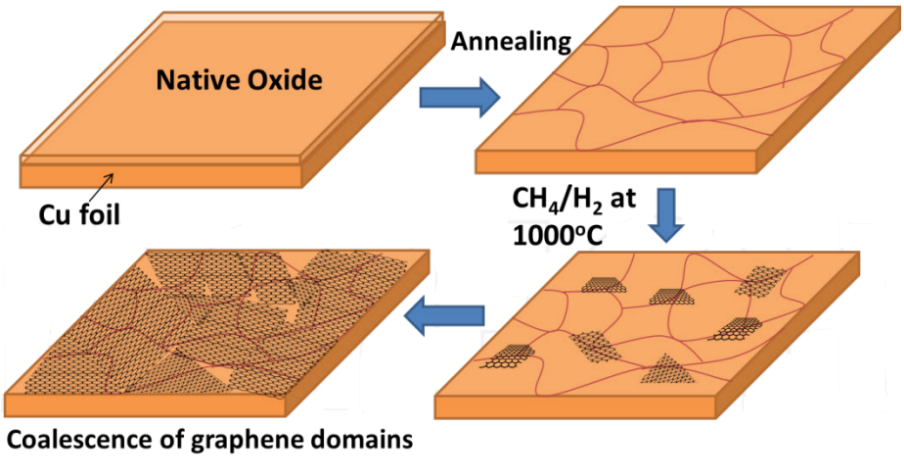

Figure 1.4: Schematic of proposed model growth of chemical vapor deposited graphene [64][77]. Amorphous Cu with a native oxide layer is annealed in a hydrogen rich atmosphere at 1000 °C. The hydrogen gas is reducing the native oxide layer and the high temperature increases the Cu domains in the poly crystalline foil. In the growth phase methane is introduced in the chamber, starting the nucleation and growth of graphene. The time of growth determines the size of the graphene domains.

1.3.4 Chemical Production

Chemical production of graphene works by oxidizing graphite to form graphene oxide (GO), then reducing graphene-oxide in a solution using harsh acids, or

heat treatment to reduced graphene-oxide (rGO) [134] [35]. The quality of chemically produced graphene is the lowest of the described techniques [28], but the cost per area is also the lowest. The chemically fabricated reduced graphene-oxide (rGO) is suspended in a liquid, and can be distributed on a substrate using a number of techniques such as spin coating, or a deposition method known as Langmuir Blodgett technique [22] [134] [71]. The Langmuir Blodgett technique is a way of depositing thin layers suspended in a liquid to the surface of a sample. A thin layer is adsorbed homogeneously on the substrate with each immersion or emersion step, due to surface energy and hydrophilic/hydrophobic interactions.

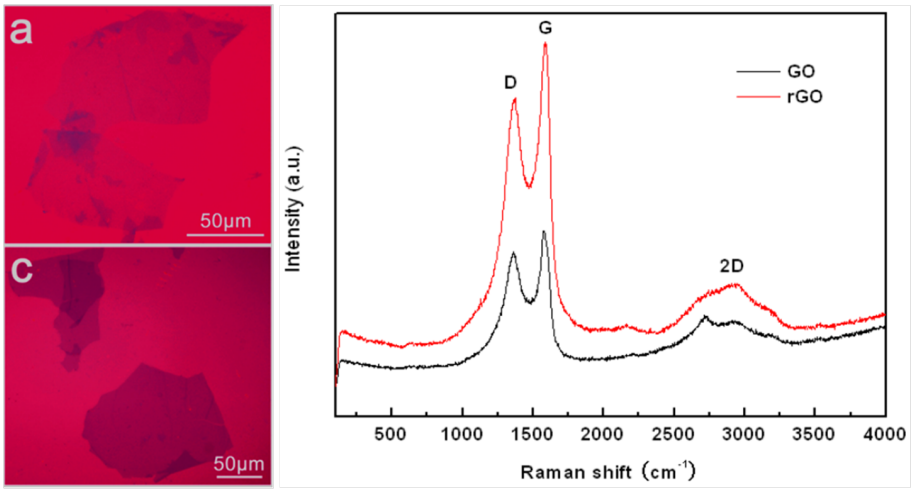

Figure 1.5: a) and c) Shows optical microscope images of chemically fabricated graphene-oxide (GO) and reduced graphene-oxide (rGO) [134], as well as Raman spectra corresponding to the two samples (right). Reprinted from [35].

1.4 Characterization Techniques

Here I have summarized the main characterization techniques used in this thesis entailing optical microscopy, scanning electron microscopy, Raman spectroscopy, electron backscatter diffraction, THz spectroscopy and transmission electron microscopy (TEM). THz spectroscopy and TEM are briefly mentioned as they are very important for graphene characterization, THz for large area electrical characterization and TEM for nanoscopic structural characterization.

1.4.1 Optical Microscopy

An optical absorption of 2.3% of light in single layer graphene makes it is problematic to observe with standard optical microscopy [84], though with a CCD camera and contrast enhancement, etc. it is possible. By tuning the material and thickness of the substrate on which graphene is situated, the contrast of 2.3% can be raised to 15% as found in [8], from optical interference in a thin glass layer, due to a high extinction coefficient of graphene, making it easily visible in an optical microscope, see figure 1.6 a. CVD graphene specifically, can be observed directly on the copper substrate on which it is grown, by growing a partially covering layer of graphene on a copper thin film substrate. The oxidation process of the copper will occur faster, where there is no graphene than where graphene is protecting copper surface, giving rise to a contrast between oxidized an un-oxidized copper, as seen in figure 1.6 b.

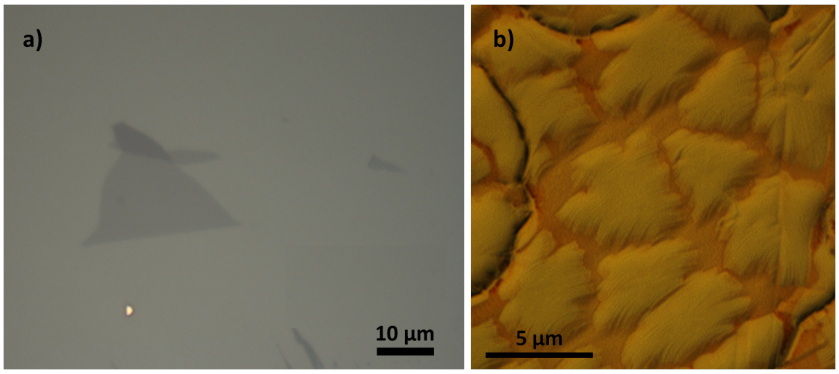

Figure 1.6: (a) optical microscope image of exfoliated graphene on 100 nm SiO_2/Si substrate, and (b) optical image of CVD grown graphene on a copper film.

1.4.2 Raman Spectroscopy

Raman spectroscopy is one of the most powerful and non invasive characterization techniques for investigating carbon materials [11]. Ranging from its three-dimensional form like diamond, graphite, diamond like carbon (DLC) and amorphous carbon, through the two-dimensional graphene, to the one-dimensional single walled carbon nanotubes.

It has been shown that Raman spectroscopy can be used as a fingerprint tool for single, bi and a few layer graphene [32] [33] [41] [40], as well as a method for determining the structural quality of the graphene. How to determine quality will be described shortly. Besides using Raman spectroscopy for fingerprinting and quality control of graphene, a multitude of characteristics can be extracted from the Raman spectrum e.g. uni-axial strain [82], bi-axial strain [26] [129], doping level [31] [53] [65], defect density [10] [23] [65], number of layers [32], as well as an estimate on the electron concentration [108]. A more detailed description of strain and doping characterization using Raman spectroscopy can be found in the appended paper in Appendix D.

By aiming a laser on to a sample, electrons are excited from their ground state to a virtual energy state. The electrons can then relax back to a ground energy state. If this state is a higher ground state than their starting point, the resulting in a loss of energy from the reflected laser light, called Stokes Raman scattering, see figure 1.8. Other types of scattering are shown in figure 1.8 as well. The Stokes Raman scattering provides detailed information about the sample. Graphene has its three most intense Raman features at 1585 cm^{-1} (G band), due to doubly degenerate, high frequency E2g mode at the Brillouin zone centre [34] (one component of the Davydov-doublet [85]), 1350 cm^{-1} (D band), from defect mediated zone-edge (near K-point) phonons, and 2700 cm^{-1} (2D band), from second order double resonant Raman scattering from zone boundary, K + ΔK phonons [108] [24]. Other secondary peaks exists [31], but these are not explained in detail in this work.

Raman spectroscopy is typically used as a single spot measurement, but can also be used to give more quantitative information of a complete sample by scanning the spot across the sample surface.

In this thesis a Thermo-Fisher Scientific DXR micro-Raman microscope was used in combination with different excitation lasers, such as 445 nm, 455 nm, 532nm and 633 nm wavelengths.

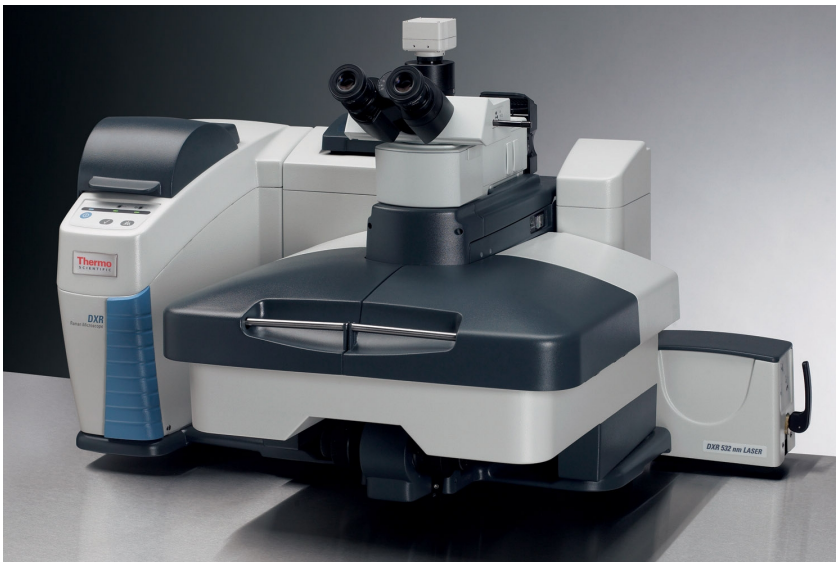

Figure 1.7: Image of the Thermo Scientific™ DXR Raman microscope. Used in this project for collecting single Raman spectra as well as micro-Raman mapping of graphene.

Graphene quality from Raman spectroscopy

Using Raman spectroscopy to determine the quality of a graphene film is a common and fast technique [31] [11]. As described above many of graphenes properties can be measured through the Raman spectrum making it an ideal way to probe the graphene without changing its properties [113]. The Raman spectrum sustain alteration, when graphene is placed on substrates. This is due to changes in the nature and density of the defects, surface charges and different strength of the graphene substrate interaction [9].

In order to determine the number of layers in graphene the relative intensity of the 2D/G peak ratio, as well as the shape and FWHM of the 2D peak can be used [31][118][32]. The relative intensity of the 2D/G peak ratio increases with decreasing layer numbers [31], though this method shows some uncertainty as shown in [41], where similar Raman spectra are reported for a varying number of layers. The evolution of the shape of the 2D peak is a more reliable method for determining the number of graphene layers (from 1 to 5 layers) [31].

The G peak position and I(2D)/I(G) ratio (2D/G) used to be taken as a finger print to identify a single layer graphene [112] [115], but was refuted in

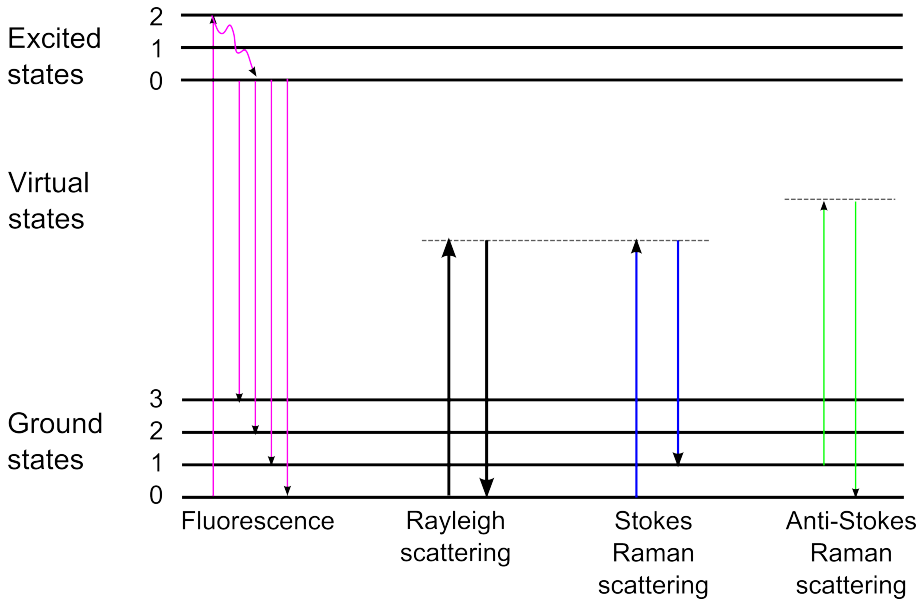

Figure 1.8: Schematic representation of Fluorescence, Rayleigh scattering, Stokes Raman scattering, Anti-Stokes Raman scattering. The numbers 0-3 corresponds to different ground and excited electronic states.

[126] and [31]. In chapter 3 (CVD graphene on Cu foils) the 2D/G ratio was used during the optimization procedure to mean higher coverage of single layer graphene.

Defects in graphene are seen as something, which breaks the symmetry in the infinite hexagonal lattice [27]. The nature of the defects and the amount of defects have an effect on the D peak [5]. The point defect density can be estimated from I(D)/I(G) ratio (D/G) and the laser wavelength to the fourth power [10]:

$$n_D(cm^{-2}) = (7.3 \pm 2.2) \cdot 10^9 \cdot E_L^4 \frac{I_D}{I_G} \tag{1.3}$$

where n_D is the defect density (cm^{-2}), E_L is the laser excitation energy (eV), and the I_D/I_G is the ratio of the intensities of the D and G peaks. The constants are estimated from plotting ${E_L}^4$(ID/IG) as a function of L_D (distance between defects).

Besides the D peak, defects also have an influence on the G peak position and FWHM, which blue shifts with the intensity of the D peak [23] and broadens with increasing number of defects [31]. Considering the average

interdefect distance, it is still possible to assume, that the higher the number of defects, the higher the D peak intensity. Though a complete theory for the Raman intensity of the D and G peaks is still lacking and is the subject of ongoing research [101]. This theory of the D/G ratio is based on Raman spectroscopic studies of graphite [30] [29]. In these studies a quantitative connection between the number or nature of defects was not investigated since the main interest was a rule of thumb estimation of disorder [29] [30] [31].

In this project I have used the D/G ratio as a measure of the defect density, and not discriminating between types of defects. For CVD grown graphene the most dominant defects are lattice defects from e.g. missing atoms or grain boundaries [50] [3] [7]. When optimizing the growth of graphene, the D/G ratio was used as a measure of the structural quality of the film.

Laser wavelength dependence

The Raman spectrum of graphene is dependent on the laser excitation frequency used, through a non-linear correlation. A linear relation between frequency of the 2D peak with the laser energy is expected as a double resonance process - this only counts for visible light, not UV. When a UV laser is used on single layer graphene, the shape of the 2D peak is no longer Lorentzian [21]. This is explained by the manifestation of the trigonal warping effect [113] in the dispersion of electrons and phonons around the Dirac point, which cancels out in the visible range due to opposite behavior in the dispersion of electrons and phonons. The Raman scattering efficiency of graphene shows a strong dependence on the type of substrate, the thickness of the substrate (in the case of SiO_2), number of layers, and the excitation energy of the laser [61].

To show the effect of the laser wavelength on the Raman signal, a single spectrum of CVD graphene on Cu was collected for each of the three wavelengths, see figure 1.9. Changing the excitation energy of the laser shows that increasing wavelength increases the amount of fluorescence from the copper surface underneath the graphene. The laser wavelengths are color coded corresponding to 445 nm for blue, 532 nm for green and 633 nm for the red spectrum.

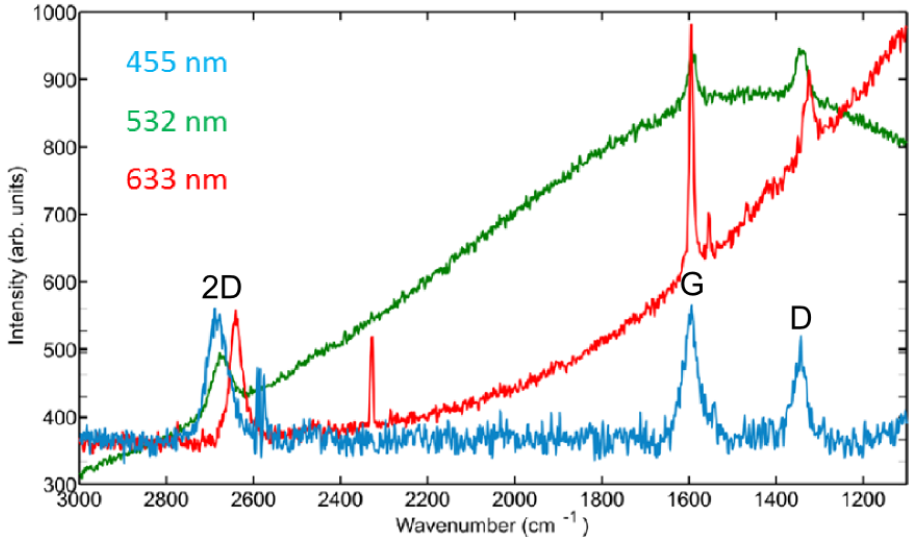

Figure 1.9: Raman spectra showing laser wavelength comparison (455 nm, 532nm, and 633 nm) of CVD graphene on a copper surface. Fluorescence is present for both 532 nm and 633 nm laser wavelengths, but is suppressed for 455 nm laser wavelength.

Raman peak fitting

For single layer graphene, see figure 1.10, the D, G, and 2D Raman peaks are fitted by a single Lorentzian curve, see figure 1.11. The fitting is done in Matlab using a script available in Appendix A. The script returns the height, width, area, FWHM, and position, as well as the fitting error of each of the three peaks in the graphene Raman spectrum.

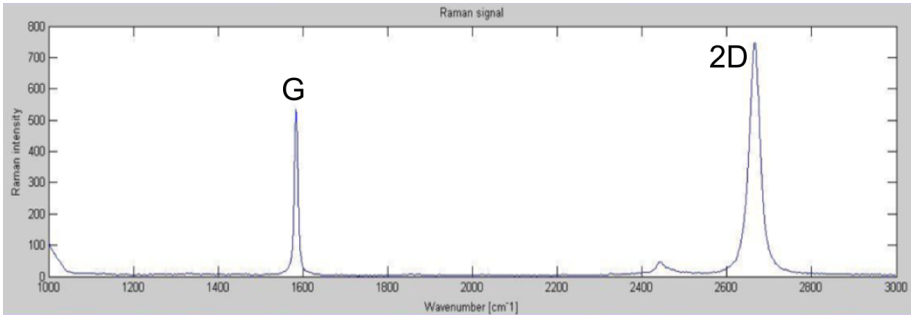

Figure 1.10: Example Raman spectrum of an exfoliated graphene sample.

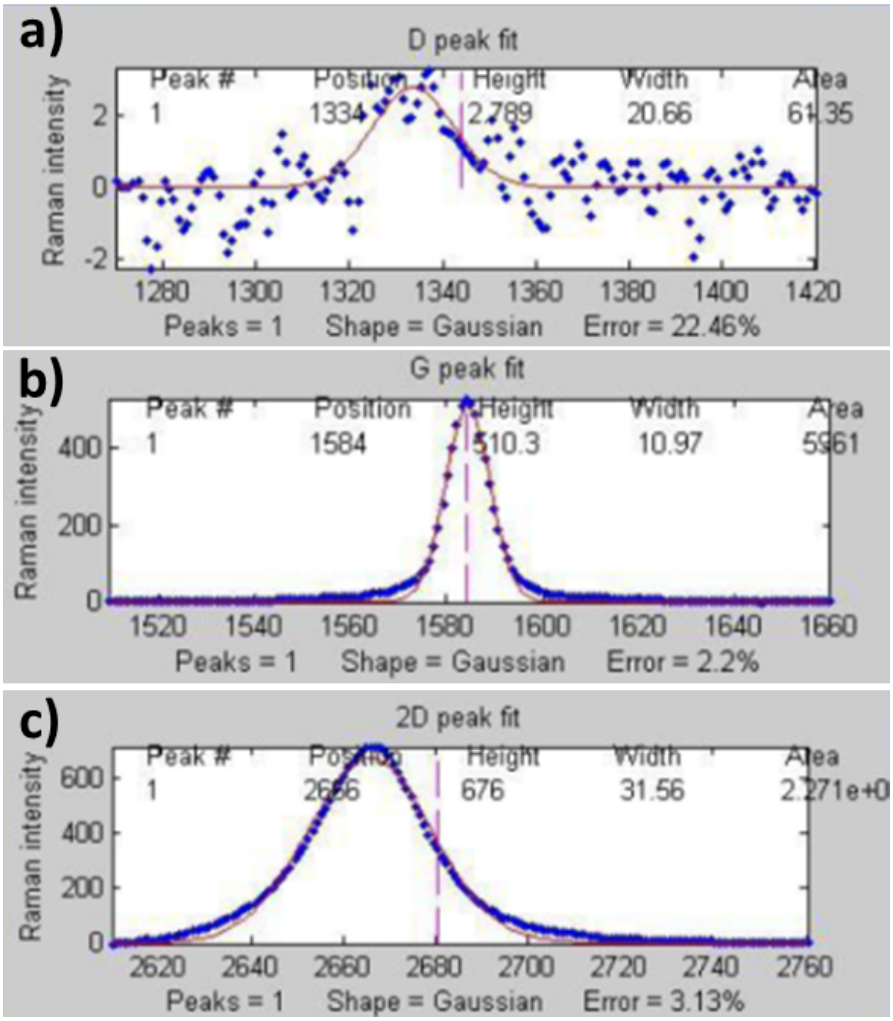

Figure 1.11: Lorentzian fits of the a) D peak, b) G peak, and c) 2D peak (including peak heights, widths, areas, and fitting errors).

1.4.3 Scanning Electron Microscopy

Scanning electron microscopy (SEM) is extensively used in this thesis for characterization of the micro-structure of surfaces such as the metallic catalyst substrate before and after annealing, as in figure 1.12. SEM is also used to characterize the shape and size of graphene crystals grown via CVD in the BM system, seen in figure 1.13. By scanning the sample surface with high energy electrons (1-30 keV), and monitoring the secondary and backscattered electrons returning from the surface, an image of the morphology can be obtained with very high resolution. Three SEMs, a FEI Nova 600 NanoSEM, FEI Helios NanoLab, and a FEI QuantaFEG SEM, has been used to characterize the surface of the catalyst substrates and the size and shape of the graphene flakes.

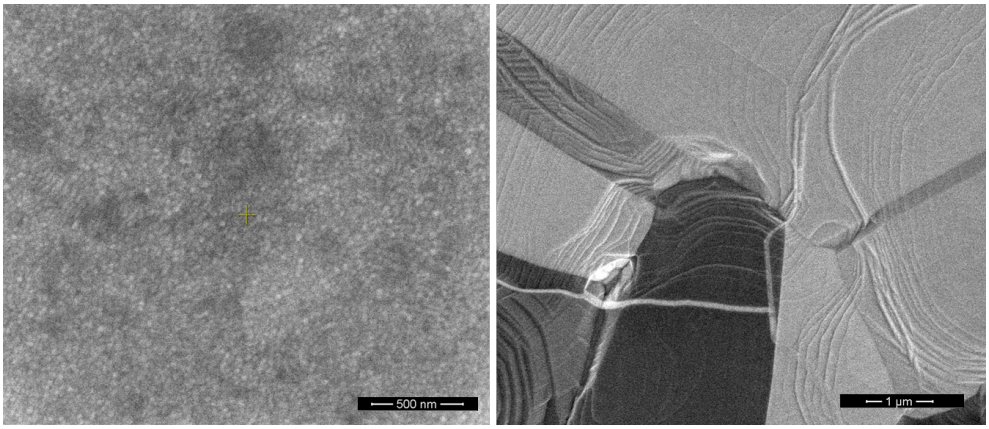

Figure 1.12: SEM images of a copper substrate before (left) and after (right) annealing (during a graphene growth recipe). Before annealing the copper is amorphous, while poly-crystalline after annealing.

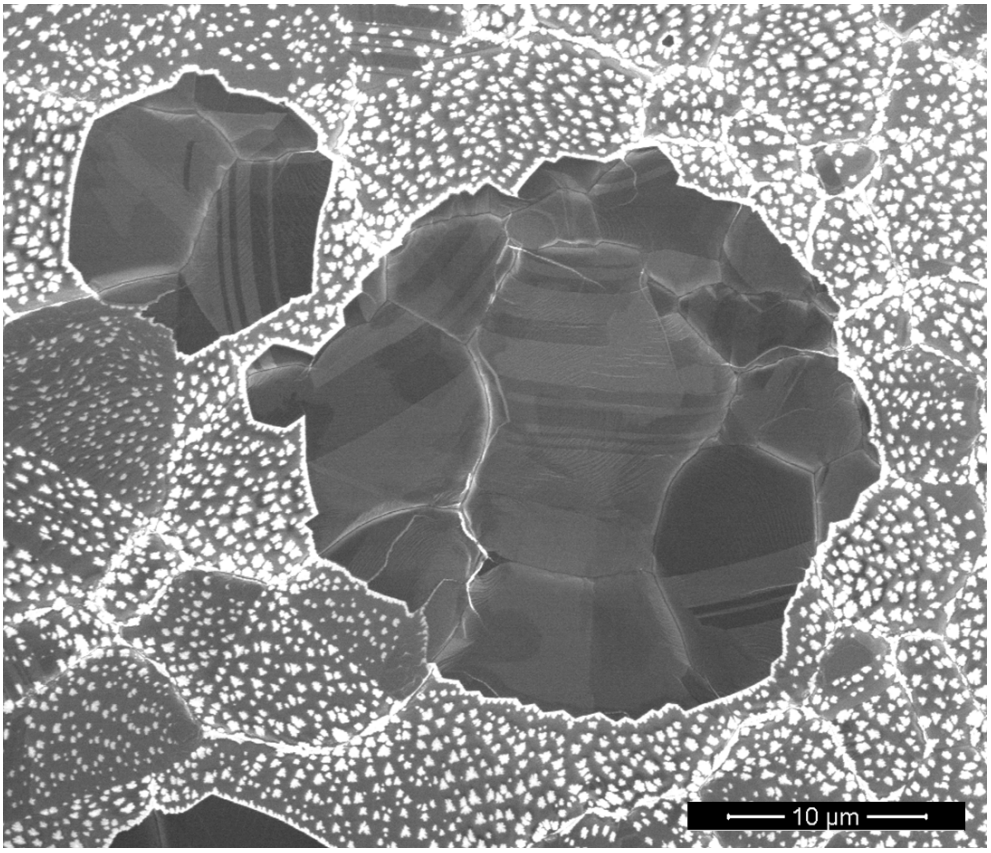

Figure 1.13: SEM image of partially grown CVD graphene on a copper thin film. The bright spots are copper oxide particles forming on the surface surrounding the two partially grown single layer graphene flakes in dark grey.

1.4.4 Electron Backscatter Diffraction

Electron Backscatter Diffraction (EBSD) is an electron microscopy microstructural crystallographic technique, where the sample is visualized by the backscattered electrons coming from the surface. It is used to examine the crystallographic orientation of materials. By indexing and identifying the crystal lattice it is possible to do defect studies, phase identification, grain boundary and morphology studies as well microstrain mapping. In this project I have used EBSD as a detection method for the distribution of crystal orientations of the catalytic materials used in the thesis, e.g. copper foil, copper films, and platinum films.

The EBSD Image quality (IQ) maps are constructed from electron backscatter diffraction data. IQ maps provide useful visualizations of microstructure. The contrast in these maps originate from sources, including phase, strain, topography, and grain boundaries [123]. IQ maps are created by setting the minimum IQ value in the scan to black and the maximum value to white and the rest of the gray values are linearly scaled between these two extremes.

The inverse pole figure (IPF) maps are orientation maps using a particular coloring scheme for the primary EBSD display. The IPF maps show the crystal orientations of the measured substrate, using a color corresponding to a crystal direction, as seen in figure 1.14(C).

EBSD is a complementary technique to studies usually carried out by x-ray diffraction, and/or electron diffraction in a transmission electron microscope. EBSD is a simple technique for studying the evolution of the crystal structure of a metallic film, and as a tool for characterizing the growth of different crystallographic orientations.

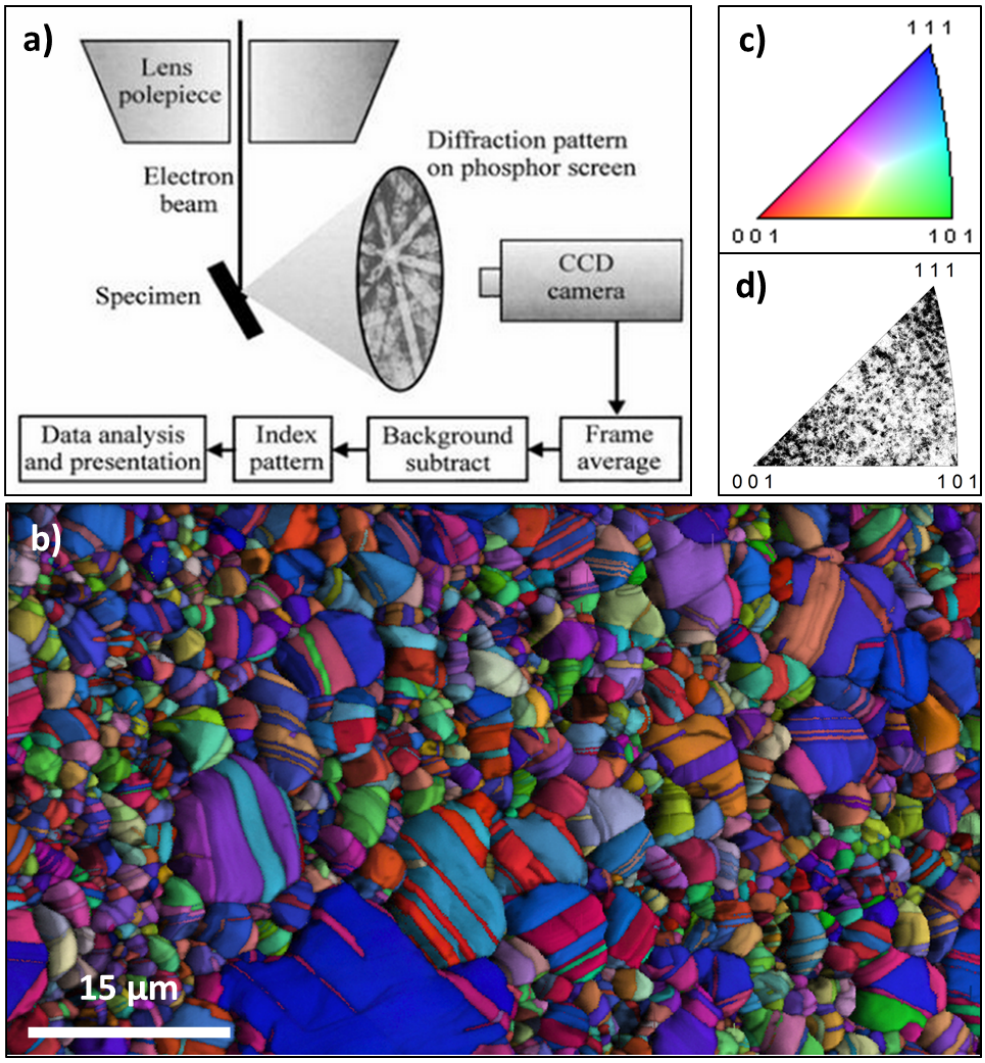

Figure 1.14: a) Schematic showing a typical EBSD setup in an electron microscope, reprinted from [51]. b) IPF image overlayed on the IQ image of a copper thin film after annealing. inset c) shows the color map corresponding to the different grain orientation of copper. The inset d) shows the distribution of grain orientations of the copper thin film after annealing.

1.4.5 Other Characterization techniques

Transmission electron microscopy (TEM) is closely related to SEM, but where the SEM observes emitted secondary and backscattered electrons from the surface of the sample, TEM observes the primary electrons passing through the sample. This means that in order to achieve an image the sample has to be very thin, on the order of 200 nm or thinner. Atomic resolution images of graphene, detection of number of layers as well as detection of atomic defects can be obtained using this technique.

THz spectroscopy is a technique similar to Raman spectroscopy. Where Raman spectroscopy probes the structural composition of the material, THz spectroscopy probes the electrical properties of the material. The THz field causes intraband transitions contrary to Raman interband transitions. The THz electric field accelerates carriers in a conducting thin film (graphene) on a dielectric substrate, causing a loss of field amplitude and a phase change in the THz pulse, which can be translated to the sheet conductance of a thin film.

Low energy electron-diffraction (LEED) is a technique for the determination of the surface structure of single-crystalline materials. The sample surface is bombarded by a collimated beam of low energy electrons (20–200 eV). The electrons interact with only the very top surface of the sample, from which a diffraction pattern can be extracted. Low energy electron-microscopy (LEEM) is used to image atomically clean surfaces, atom-surface interactions, and thin (crystalline) films. The LEEM system is similar to the LEED system, but the LEEM system can be used to produce a real-space image showing the crystallinity of the sample, instead of just the diffraction pattern.

1.5 Design of Experiments

In chapter 5 (CVD Graphene on Cu films on Sapphire) optimization of a BM growth recipe was carried out using design of experiments (DOE) [83]. As will be clear from chapters 3 and 4, the optimization of a graphene growth recipe is a complicated procedure with many variables (chapter 2), that have an influence on the process. The change one separate factor at a time (COST) approach also assumes that the effect of each variable is completely independent of each other, this is often not the case [1]. The number of experiments needed for this method increases dramatically with the number of parameters, whereas DOE is a way of gathering the greatest possible volume of information about a system using the fewest experiments possible [39].

Optimization of CVD growth of graphene and carbon nanotubes using DOE, has a benefit to a conventional COST approach by the fact that fewer experiments are needed to obtain an optimized process [63] [1] [121], and a true global optimum can be found. In this work I want to improve recipes by using DOE and fitting the response surface (methodology by G. E. P. Box and K. B. Wilson in 1951) on the basis of a screening design. Some controllable parameters were excluded to keep the number of experiments reasonably low (19 in this case).

The software package SAS JMP is used to generate the experimental screening designs. After completion of the experiments, data analysis is carried out in SAS JMP. The response surface is calculated by the software for a wanted response, e.g. nucleation density or coverage. The corresponding level of significance (P-value) of the model is provided by the software.

1.6 Ostwald Ripening

Ostwald ripening is a phenomenon observed in solid solutions or liquid sols, which describes the evolution of an inhomogeneous structure over time i.e. small crystals dissolve, and redeposit onto larger crystals. The process occurs because smaller particles have a higher surface energy, hence a higher total Gibbs energy, than larger particles, giving rise to an apparent higher solubility [54].

In this work the focus is on the crystallographic evolution of thin copper films as a function of annealing. The copper film is fabricated via physical sputtering on to the surface of a SiO_2/Si wafer. The resulting crystal structure of the film is either amorphous or nanocrystalline, with a unimodal distribution (a normal distribution is an example of a unimodal distribution) of cluster sizes depending on the deposition conditions. Growth of these clusters happen during annealing. This chapter is based on the text book "Recrystallization and Related Annealing Phenomena" by F. Humphreys [99].

An abnormal growth model describes how clusters of domains grow from a unimodal distribution to grains displaying a bimodal log-normal distribution when annealed. This bimodal distribution happens because the atoms of the smaller grains aggregate on the larger grains, due to decreased surface energy, in a process called Ostwald ripening [90].

During abnormal grain growth, two energy models compete to determine, which crystal orientation will become the dominant one [136] [111]. 1) When surface and interface energy dominates: An energy minimization occurs, when the crystal orientation with the lowest energy (Cu(111)) is parallel to the interface of the film/substrate. 2) When strain energy dominates: The the minimum energy plane direction will typically be Cu(100) planes. For annealing temperatures near the deposition temperature and for thin films, the surface and interface energy minimization dominates, while for thicker films strain energy minimization dominates.

A detailed description of the relationship between the mean grain radius and time and temperature, can be found in [81].

1.7 Graphene Growth Kinetics

The overall growth mechanics of CVD graphene on a copper surface, comprises (1) mass transport of the carbon species through the bulk gas flow to the surface of the catalyst. This happens through a boundary layer, which is an interphase layer between the bulk gas flow and the surface of the substrate, see figure 1.15. (2) Adsorption of the carbon species on the surface. (3) Decomposition of inactive carbon species, e.g. CH_4 which doesn't react with other species, to form active carbon species, e.g. CH_3, CH_2 and CH_1, which readily react in order to fulfill the octet rule. (4) Active carbon species diffuse across the surface binding to other carbon atoms forming small graphene clusters. (5) The clusters grow to form a single-/polycrystalline film covering the surface. (6) Desorption of inactive species i.e. H_2 and diffusion from the surface to the bulk gas flow [6]. An important secondary process is the preferential etching of graphene crystals by hydrogen radicals [131] [132]. 4 Hydrogen atoms can bind to "dangling" carbon atoms, leaving zigzag edges behind in the graphene [132].

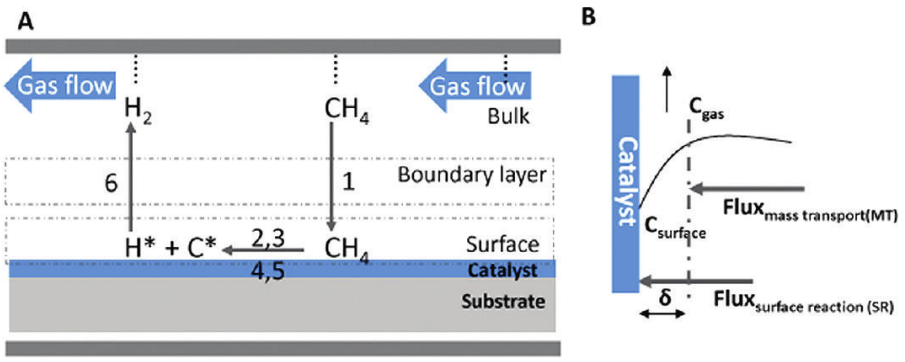

Figure 1.15: A) Schematics of a horizontal CVD furnace, showing the growth kinetics of graphene on a low solid solubility catalyst e.g. Cu. B) mass transport and gas fluxes under steady state conditions. Reprinted from [6].

Figure 1.15 (A) shows the graphene growth steps described previously for a horizontal flow tube furnace CVD system. The bulk gas flow is, where the majority of the gasses mix and reside from the inlet to the outlet of the system in a laminar flow. The boundary layer is a region close to the surface of the sample, where the gas flow is stagnant and not a horizontal laminar flow. The mass transport of the boundary layer is dependent on the gas species concentration in the bulk, the concentration on the surface and

a mass transport coefficient [6]. Figure 1.15 (B) shows the mass transport through the bulk flow and the boundary layer. The solid line represents the gas fluxes through each layer.

The boundary layer is thicker for low pressure chemical vapor deposition (LPCVD) than for atmospheric pressure chemical vapor deposition (APCVD), but the diffusivity coefficient is significantly larger for LPCVD than APCVD leading to an overall increase in the diffusion coefficient, when lowering the background pressure [6]. This leads to a higher growth rate for LPCVD compared to APCVD.

Dehydrogenation of methane to atomic carbon and four hydrogen atoms is not likely, due to small carbon clusters being more stable than atomic carbon, leading to the conclusion that the growth would start without a nucleation step. This is not what is seen experimentally in [130].

The growth intermediates from methane encompasses a large variety of carbon clusters i.e. carbon rectangles, carbon dimers, carbon triangles and carbon chains. When these saturates the surface of Cu(111), defective graphene is made [86]. The defective graphene can be healed to vacancy-free graphene, after thermal annealing above 800 ^{o}C in the presence of CH_4 at 10^{-7} mbar pressure [86].

By tuning the graphene growth parameters it is possible to change the shape of the graphene crystals for atmospheric pressure CVD [124]. Here they show that by changing the ratio of $Ar/H_2/CH_4$ they can vary the shape of the graphene crystals from hexagonal to spherical. In another study they show orientation control of APCVD grown graphene domains on a copper film on sapphire, by controlling the $Ar/H_2/CH_4$ ratio [46].

Two regimes for CVD growth of graphene exists, (1) diffusion limited growth and (2) kinetically limited growth. In (1) the graphene crystal is determined by a high growth rate, leading to dendritic graphene flakes. In (2) the growth is determined by a slower growth rate than (1), leading to hexagonal or circular graphene flakes [124].

Challenges in CVD growth

In the following I have listed a few critical challenges that needs to be overcome in order for growth of perfect graphene via CVD to become a reality:

1. Selecting the right catalytic substrate for graphene growth
2. Choosing the right carbon precursor gas
3. Increasing the graphene crystal domain size, in order to reduce the amount of grain boundaries
4. Controlling the number of graphene layers, since the electronic properties are highly dependent on this
5. Control over the graphene growth conditions. This is a necessity for points 3 and 4

1.8 Graphene Field Effect Transistors

In this thesis graphene field effect transistor (GFET) measurements are electrical measurements of photolithographically patterned graphene on a highly doped silicon wafer with a thermally grown oxide layer of 300 nm thickness. The graphene is patterned to form a Hall bar device structure, which is connected to the measurement setup via thermally deposited chromium/gold electrodes, as shown in fig 1.16. A detailed fabrication scheme of the graphene devices is described shortly. The Hall bar devices are 18 µm long and 2 µm wide between the source and drain contacts. The voltage probes are 1 µm wide with a 7 µm pitch, see figure 1.16. The gate contact is made by mechanically removing the SiO_2 and adding an electrode using a conducting carbon paint.

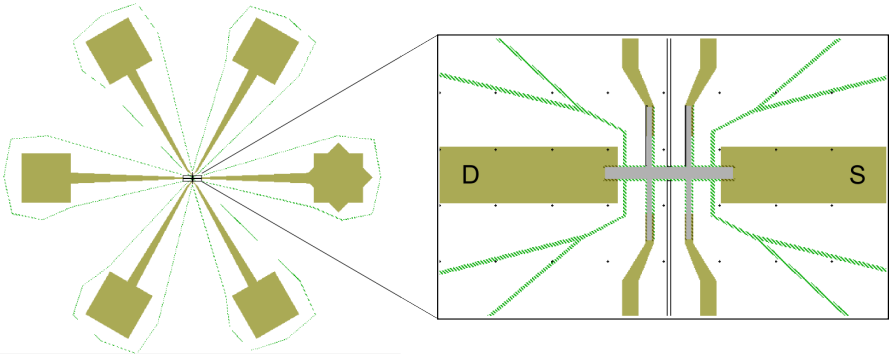

Figure 1.16: Graphene Hall bar device structure (light grey area), gold contacts design (solid yellow areas). The green dashed lines define, where graphene will be etched away in order to electrically isolate devices from each other. Drawn in L-Edit.

The electrical measurements were carried out using a Linkam stage, which allows up to 8 electrical connections, see figure 1.17. The stage contains heating and cooling elements, while keeping the sample in a controlled nitrogen atmosphere (or low vacuum). A LabVIEW program is used to both sweep the back gate (V_{gate}), while measuring the source/drain current (I_{DS} as a function of the gate voltage). The Hall bar electrodes are tested before the measurements as well as the gate to ensure the device is properly contacted and does not have leakage currents.

The samples are annealed at 250 ºC for 30 minutes before measurements are carried out, in a nitrogen atmosphere. Annealing is performed in order to remove any contaminants from the surface of the graphene device e.g. water

and other unwanted adsorbants (which evaporate from the surface). The annealing also causes a decrease in the overall doping level of the graphene, due to the removal of adsorbants. Measurements are then carried out, with the gate sweep set to 100 ms/V_g, at temperatures ranging from -196 ºC to 156 ºC using liquid nitrogen for low temperature measurements and the built in stage heater for high temperature measurements.

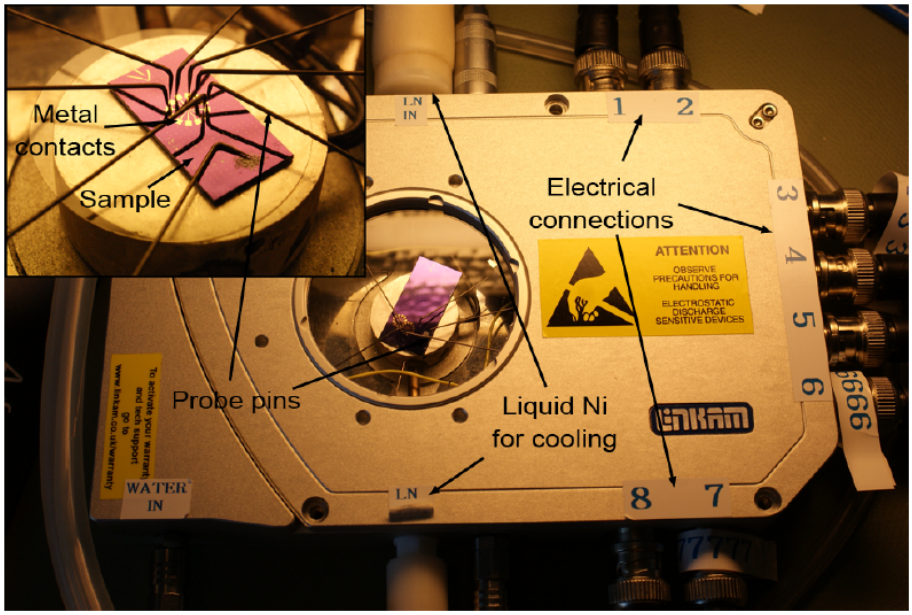

Figure 1.17: Photograph of a graphene sample mounted in the Linkam stage in a nitrogen atmosphere. Inset shows a close up of a graphene sample. Reprinted from [62].

Graphene FET measurements are shown in chapter 6 for CVD graphene grown on Cu foil, Cu film on SiO_2/Si, and Cu film on sapphire respectively.

1.9 Fabrication of GFET Devices

Fabrication of GFET devices is necessary to measure e.g. the conductance and the carrier mobility of a CVD grown graphene film. In this section I will describe the process of fabricating these devices.

1.9.1 Growth and transfer of graphene

This work was carried out in collaboration with David A Mackenzie who was in charge of the e-beam lithography and device measurements and Patrick Whelan who was in charge of the graphene transfer. I was in charge of growing the CVD graphene and other cleanroom fabrication steps, as well as played an active role in e-beam lithography, device measurements and transfer parts.

Graphene was grown in the BM system using a recipe developed for graphene growth on copper thin film on a sapphire wafer, found in appendix B. The recipe uses 30 % power on the bottom heater and 75 % power on the top heater. The Ar, H_2, and CH_4 flow rates were 1000 sccm, 100 sccm, and 5 sccm respectively, at 15 mbar pressure. Annealing time was 30 minutes, in a hydrogen (1000 sccm) and argon (1000 sccm) atmosphere at 15 mbar pressure, while the growth time was kept at 2 minutes.

Samples of Cu foil, Cu film on SiO_2/Si, and Cu on sapphire were placed on the sample holder in the BM system and graphene was grown on all the substrates simultaneously. This removes any process to process variation there might be in the BM system.

The graphene on the three substrate types were then transferred using three different techniques, chemical etching of the copper substrate, electrochemical bubbling of the graphene from the copper substrate [37], and an electrochemical method, called oxidative decoupling transfer (ODT)[95]. The polymer used for all of the graphene transfers was cellulose acetate-butyrate (CAB). The target substrate was a 300 nm SiO_2 on a highly doped silicon wafer. All of the transferred graphene was placed on the same wafer.

Optical microscopy was used to identify promising regions (without visible holes or cracks) in the transferred graphene samples for the GFET devices, see figure 1.18. Hall bar devices (as described earlier) were placed in all of the identified graphene regions on the wafer using a lithography mask design software (L-Edit). About 100 devices were planned on one wafer.

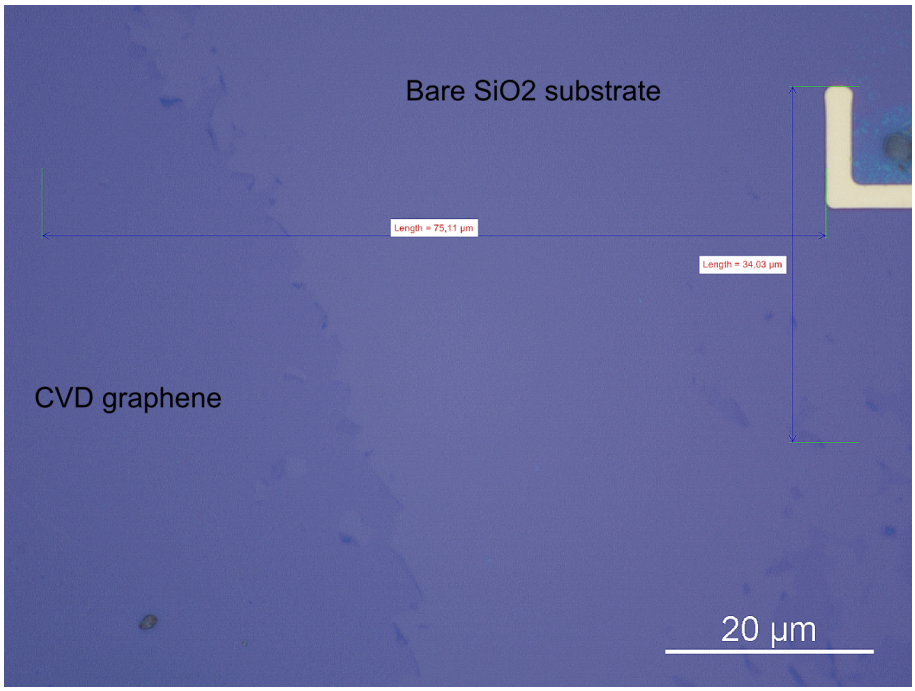

Figure 1.18: Optical microscope image of CVD graphene area to be used for GFET device. An index mark (yellow) on the wafer is used as a guide for placing the Hall bar design during the e-beam lithography step.

1.9.2 Cleanroom fabrication of devices

Following the transfer of CVD graphene to a 300 nm SiO_2 on silicon wafer, Hall bar devices were fabricated in the DTU Danchip cleanroom, using electron beam (e-beam) lithography, metal lift-off, and reactive ion etching (RIE) of the graphene.

1 - cleaning The wafer (containing CVD graphene) is cleaned in Triton x-100 diluted in DI water, followed by a soak in acetone, and a rinse in 2-propanol (IPA). Then the wafer is baked on a hotplate at 200 ^{o}C for 5 minutes to remove any excess water on the wafer.

2 - electrode deposition The wafer is then spin coated in a double layer of poly-methyl-methacrylate (pmma), using two different solvents (anisol and MIBK) to help ease the lift-off process. A thin layer of thermal aluminium is deposited on the pmma to decrease any charging effects from the

e-beam processing. The metal contact patterns are exposed in a JEOL-9500 e-beam lithography system. The exposed pmma is then developed in MIBK:IPA (1:3) for 90 seconds and rinsed in IPA. A bi-layer of 3 nm Cr and 30 nm Au is deposited using e-beam deposition in an Alcatel system. The thin chromium layer is added to improve the adhesion of the gold electrode to the substrate. The excess metal is lifted off using 40 ^{o}C hot acetone overnight.

3 - Hall bar definition The shape of the graphene Hall bar is then fabricated by deposition of one layer pmma(in anisol) and thermal aluminium as before. The graphen/pmma is exposed in the green dashed regions as shown in figure 1.16, using e-beam lithography and developed in DI water:IPA (3:7) solution. The bare graphene is then etched in a RIE system for 23 seconds, isolating the graphene Hall bar device from the rest of the devices, while leaving the SiO_2 intact (this is necessary to avoid leakage currents). The remaining pmma is then removed in 40 ^{o}C hot acetone overnight.

Chapter 2

Chemical Vapor Deposition

Chemical vapor deposition (CVD) is a fabrication technique involving deposition of a chemical in the vapor phase to solid phase on a solid substrate. In this thesis a carbon precursor gas, i.e. methane, is used to deposit carbon atoms and hydrocarbon compounds on a catalytic metal substrate, in this thesis copper is used. The carbon atoms cluster and form graphene crystals on the surface of the copper substrate. For this reaction, methane to graphene on copper, to work a few other factors needs to be involved. The reaction of methane to graphene, occurs through dehydrogenation of methane to atomic carbon and four hydrogen atoms [130]. The carbon atoms diffuse on the surface of the copper, through surface mobility which increases with increasing temperature, to form small graphene clusters, that grow in size [6]. This phenomenon is caused by atomic carbon on the Cu surface being less stable than small carbon clusters [13] [125].

A smoother copper surface is achieved through atmospheric pressure chemical vapor deposition (APCVD) of graphene compared to low pressure chemical vapor deposition (LPCVD), due to a higher evaporation of copper atoms at lower pressures. This leads to higher activation energies of graphene nucleation (9 eV) for APCVD compared to (4 eV) for LPCVD [114]. Graphene grown at lower than 1000 ^{o}C has a higher nucleation density on Cu (111) than (100) and (101) for LPCVD [114]. This temperature effect on nucleation density is not observed for APCVD [114]. At temperatures above 1000 ^{o}C the effect on nucleation density is not observed.

The nucleation density is as well affected by the surface mobility of the carbon species and the desorption rate, which varies with temperature. The growth rate for graphene on different copper crystal orientation varies very

little, with a slightly faster rate on Cu(111) compared to Cu(100) [122]. The nucleation density is affected by the rates of nucleus growth by adatom capture, surface diffusion of carbon species, and desorption of carbon adatoms. Two regimes exist: one below 870 °C, where nucleaus growth by carbon adatom capture dictates the nucleation density, and one above 870 °C where the desorption rate of carbon species controls the nucleation density [60].

In this work I have grown graphene at LPCVD conditions rather than near APCVD conditions, which the Black Magic CVD system is capable of. This is due to the fact that the Black Magic CVD system is limited to 100 mbar pressure, while using argon gas, and 700 mbar using nitrogen gas. This is a manufacturer imposed limitation, since a high pressure test is needed to run at higher than 100 mbar pressure. This pressure test can only be executed using nitrogen gas. Nitrogen gasses are known to cause an increased doping level of CVD grown graphene [73] [74] [120], while argon does not cause increased doping. In order to achieve CVD graphene with quality, which resembles that of exfoliated graphene, a low doping level is important.

2.0.3 CVD growth methods

Growth of graphene requires a carbon source, a substrate and heat. The carbon source can be e.g. external in the form of gasses, liquids or solids, as well as internal in the form of carbon contamination of the substrate.

Using methane (CH_4) as the carbon precursor gas requires hydrogen dilution for growth at temperatures above 1000 °C to maintain a reduced copper surface during growth and yield high quality graphene. The CH_4 provides the carbon necessary for growth, where CH_4 molecules adsorb on the surface. The process of reducing CH_4 to atomic hydrogen is too expensive in terms of binding energy needed to remove all of the hydrogen atoms before forming graphene from the carbon atoms [130]. Though maintaining a balanced CH_4/H_2 ratio is crucial because the hydrogen acts as an etchant of the graphene.

Changing the precursor gas to C_6H_6 negates the need for H_2 during fabrication of graphene and consistently provides high quality graphene at temperatures 100-150 °C lower than for CH_4 [57].

A simple annealing process of carbon contaminated Cu can be used for

growing graphene. Graphene is grown on carbon contaminated sputtered Cu on Al_2O_3, by a simple annealing step without additional carbon added to the processing at atmospheric pressure and a gas flow of 20 sccm of hydrogen and 400 sccm of argon. In this study the growth of graphene is highly dependent on the annealing temperature, where temperatures below 800 °C result in amorphous carbon, while graphene is produced for temperatures above 800 °C [48].

2.1 Growth of graphene in a cold wall CVD system

The Aixtron Black Magic 4" CVD (BM) system (schematic in figure 2.1 and 2.2) a cold wall system, was used throughout this project for growth of graphene. In a cold wall CVD reactor the sample is heated through a heating holder, instead of being heated by the entire system. This method leads to cooler chamber walls than the sample, giving rise to the name cold wall reactor. This is opposite to a hot wall system, where the chamber walls are heated and the sample is heated through heat radiation, rather than by direct contact with the heater as in the cold wall system. The main difference between these two kinds of systems, from a catalytic reaction point of view, is that in the hot wall system more reactions will occur in the gas phase compared to the cold wall system, where reactions are suppressed due to the lower temperature of the bulk gas flow. In the cold wall system ideally all of the preferred reactions happen on the surface of the intended catalytic material, in this case a copper substrate.

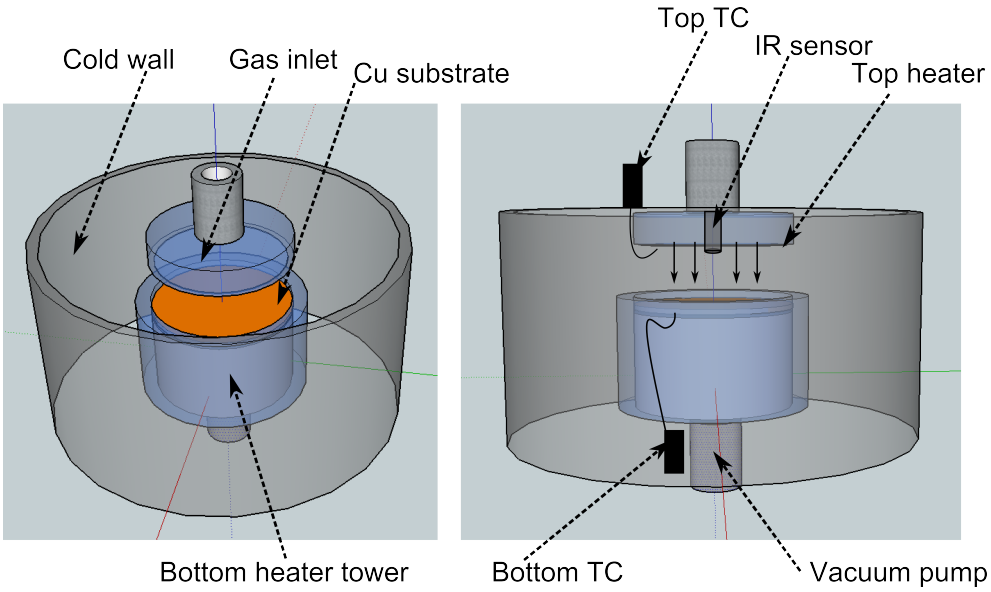

Figure 2.1: Figure showing a schematic of the Black Magic CVD system, in 3D view (left) and side view (right). Top and bottom heaters/thermocouples, shower head for gas inlet, IR temperature sensor, Cu substrate and vacuum pump are labelled.

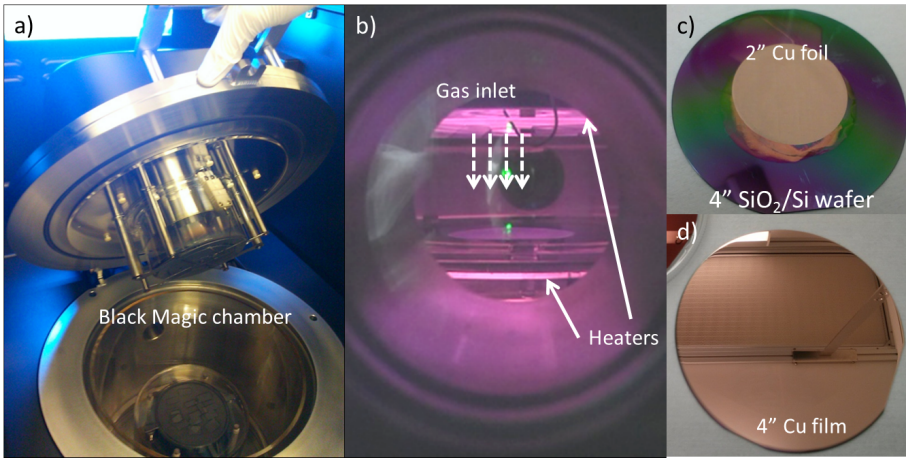

Figure 2.2: Shows the inside of the Black Magic while the chamber is, a) open and ready for sample loading/unloading. b) An optical image of the chamber while running a process at high temperature. c) A 2" copper foil disc laying on a 4" SiO_2/Si wafer after growth of graphene, and d) a Cu film on a 4" SiO_2/Si wafer.

In the BM system gasses are let through a shower head, see figure 2.3(left) directly above the sample heater plate (figure 2.4, a top heater is also installed (figure 2.3 (right)) to obtain a more uniform temperature gradient vertically. The temperature of the heaters is measured using K-type thermocouples [20]. The gasses are sprayed directly onto the substrate in a vertical flow, and then pumped out of the bottom end of the chamber beneath the sample heater tower. In a hot wall tube furnace the gasses are flowed parallel to the substrate in a laminar type flow (figure 1.15). These systems usually have more active species, i.e. hydrocarbon- and hydrogen radicals, available near the inlet of the system compared to near the outlet of the system, leading to a decreasing concentration gradient of active species throughout the chamber [6] [18] [117].

A hot wall system is usually made as a horizontal quartz tube with a coil heater surrounding the tube, and gasses let in in one end and pumped out in the other end. This set-up provides benefits in the form of quick heating and cooling of the gas flow and sample. The disadvantages of this type of system lies in the concentration gradient of hydrocarbon and hydrogen gasses in the chamber, and the limited sample sizes, which can be accommodated.

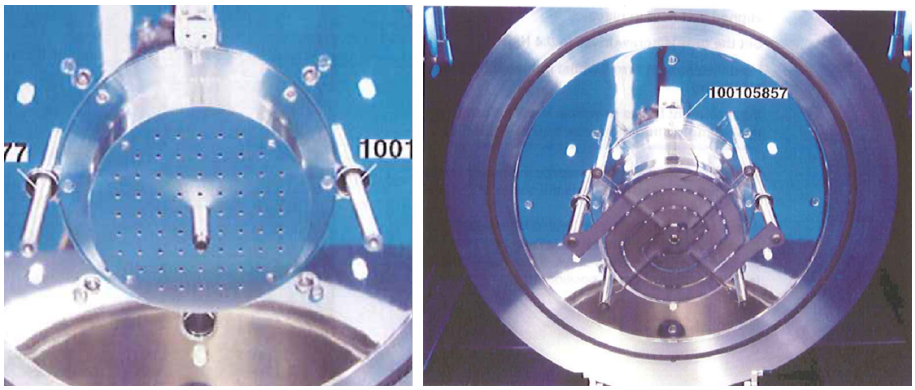

Figure 2.3: (left) Photograph of the top gas inlet shower head, and (right) graphite spiral heating element beneath second shower head element. The center cylinder in both images show the IR temperature sensor. Reprinted from [2]

Figure 2.4: Photograph of the bottom heater- element and tower. The sample holder is placed directly above the heater. Modified from [2]

2.2 Temperature Control

For the first part of this thesis growth of graphene in the Black Magic system was completed using a built-in temperature controller. The temperature is controlled through a PID controller. For the temperature the PID controller calculates an error value as the difference between the measured temperature and the desired setpoint temperature. The PID controller attempts to minimize the temperature error by adjusting the power applied to the heater. Temperature measurements coming from two thermocouples placed directly on the heaters, see figure 2.1 (right) completes the feedback loop. This system works by applying a power to the heaters and measuring the temperature and adjusting the power according to the set ramping rates and set temperatures. In principle this system can provide control over the desired temperatures by controlling the applied power to the heaters individually. This system requires stable thermocouples, that do not change over time, with high temperatures, or gas flows to maintain a consistent temperature. It was found that the thermocouples do degrade over time and therefore do not provide the same power/temperature as expected. PID temperature control can also be provided through an infra-red (IR) temperature sensor, which is located in the center of the top heater, as seen in figure 2.3. The IR sensor has been calibrated from the factory to accurately measure the temperature on silicon. This means that, when a copper sample is placed dead center on the sample holder, the IR sensor is reading the IR radiation of copper and not silicon resulting in inaccurate temperature measurements. A correction factor for copper could be implemented, though evaporation of copper was observed leaving patches of bare silicon.

In this thesis, growth of graphene on Cu films was carried out using a constant applied power, instead of the PID controller. By applying a constant power to the heaters, the temperature of the chamber will stabilize over time. The stabilization period is implemented in the annealing step in the recipes, and achieved within 10 to 15 minutes. Since a fixed power is applied through the growth recipe the thermal fluctuations and variations over time can be avoided. This technique requires calibration of the temperature as a function of the applied power to the heaters. In the following section, I have created recipes and a work flow to calibrate the Black Magic system for constant power control over the temperature.

2.2.1 Constant Power Calibration

In order to determine the sample surface temperatures in the Black Magic CVD system at various power inputs, a calibration recipe was developed. This recipe requires a silicon wafer or a silicon wafer with an oxide layer, in order to get consistent and accurate measurements from the infra-red (IR) temperature sensor. An IR temperature sensor works by detecting the infra-red radiation emitted from a sample, in this case calibrated to silicon, and translates this radiation information to a temperature. The recipe includes a stable gas flow of H2 and Ar and a constant pressure. First the top heater is kept constant while the bottom heater is varied and then vice versa. This recipe creates two curves containing the temperature as a function of applied power on both of the heaters. From these curves a formula for the actual temperature can be extracted using linear regression analysis.

$$T_{IR} = A \cdot BP(\%) + B \cdot TP(\%) + C \tag{2.1}$$

Where A, B, and C are constants relating to the slope of the bottom heater, the top heater, and the y-axis intersection respectively. BP and TP are the power percentages of the bottom heater and the top heater respectively. From the two curves the values of A, B, and C can be found, see figure 2.5, giving:

$$T_{IR} = 4.88 \cdot BP(\%) + 2.46 \cdot TP(\%) + 588.5 \tag{2.2}$$

As well as measuring the temperature using the IR sensor, an extra thermocouple (TC) was added to the Black Magic system, this TC was coupled to an external temperature meter. The TC probe was then placed on an oxidized silicon wafer near the edge of the wafer and near the center. Then the recipe for power versus temperature was run and the temperatures measured with the external TC was noted, first while the probe was near the edge and second while the probe was in the center, see figure 2.6. As is seen, the temperature measured using the external TC varies by 50 degrees from the center to the edge over the temperature range investigated.

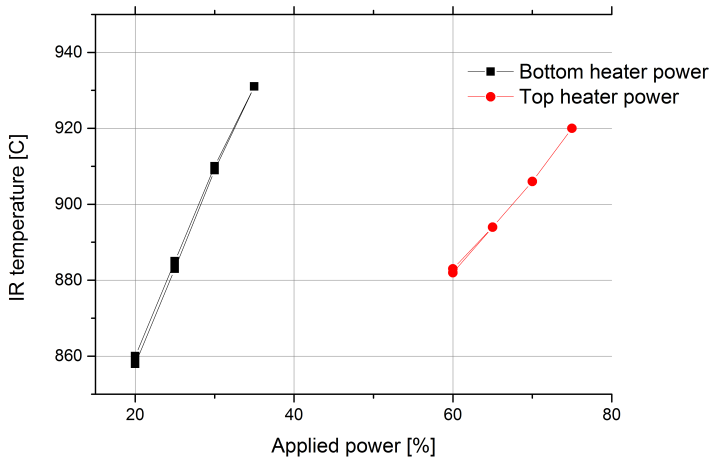

Figure 2.5: Graph of IR temperature versus applied power on both the top and the bottom heater. While the bottom heater was changed, the top heater was held constant at 70 % power. The Bottom heater was held at a constant 30 % power while the top heater was varied.

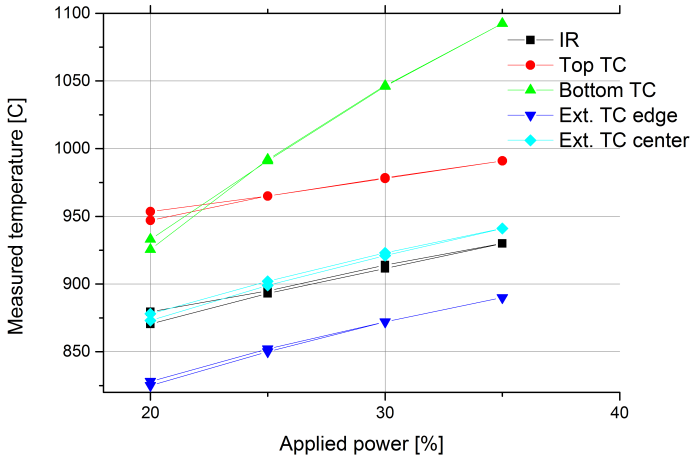

Figure 2.6: Graph of temperature versus bottom heater power through the IR sensor, the top heater TC, the bottom heater TC, and an external TC positioned near the edge of the sample and near the center of the sample. The top heater is kept constant through this experiment at 75 % power.

2.2.2 Temperature and flow rates

In order to verify the influence of flow rates on the temperature, a recipe was written using the same concept as above describing the temperature as a function of the applied power. With typical growth recipes following a basic structure of - 1000 sccm of hydrogen, 1000 sccm of argon while only 1-10 sccm of methane - only the flow rates of argon and hydrogen are considered to have an influence on the temperature. This is due to the fact that typical flow rates of these two gasses, during graphene growth, are 100s to 1000 times greater than the flow of methane in the system. First the flow rate of argon was varied from 50 sccm to 1000 sccm, while keeping the pressure constant and the flow of hydrogen turned off. Then this procedure was done for the hydrogen flow rate as well, over the same range of flow rates. The resulting measurements are shown in figure 2.7, where it can be seen that the argon flow rate has a negative impact on the temperature, while the H_2 flow rate doesn't influence the temperature. Though it can also be seen that adding hydrogen to the chamber greatly reduces the temperature measured by the IR sensor. The specific heat capacity of H_2 gas is more than 25 times greater than that of argon gas. The observed influence of the hydrogen gas must mean that at the flow rates used in this experiment, the heat exchange of the H_2 gas is saturated, while it is not for the argon gas. The very low heat capacity of the argon gas also means a much lower effect on the temperature.

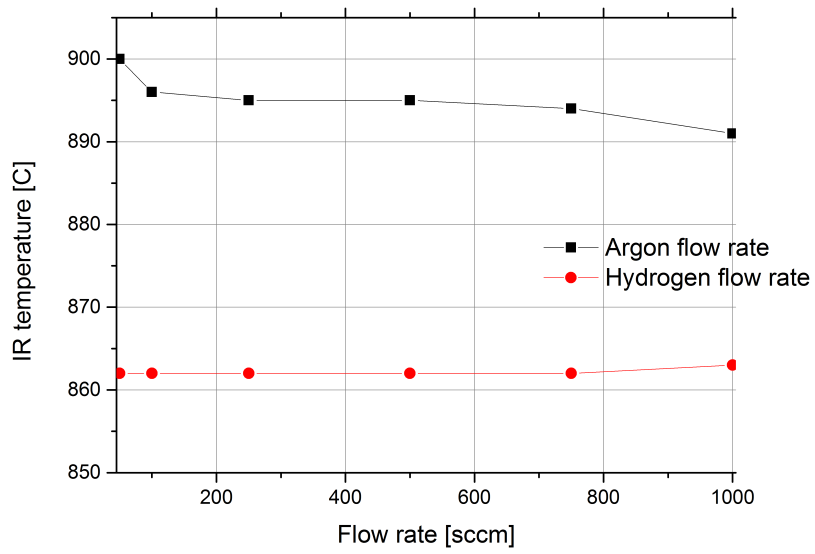

Figure 2.7: Graph of the IR temperature as a function of the flow rates of hydrogen and argon. No significant changes in temperature is seen for varying flows of hydrogen, while the temperature decreases for increasing flow rates of argon.

2.2.3 Temperature and Pressure

To gauge the relationship between the chamber pressure and temperature a recipe with fixed flow rates was used, and the pressure varied from 15 mbar to 90 mbar. The corresponding temperature was measured, see figure 2.8. From this study a very small temperature variation was seen.

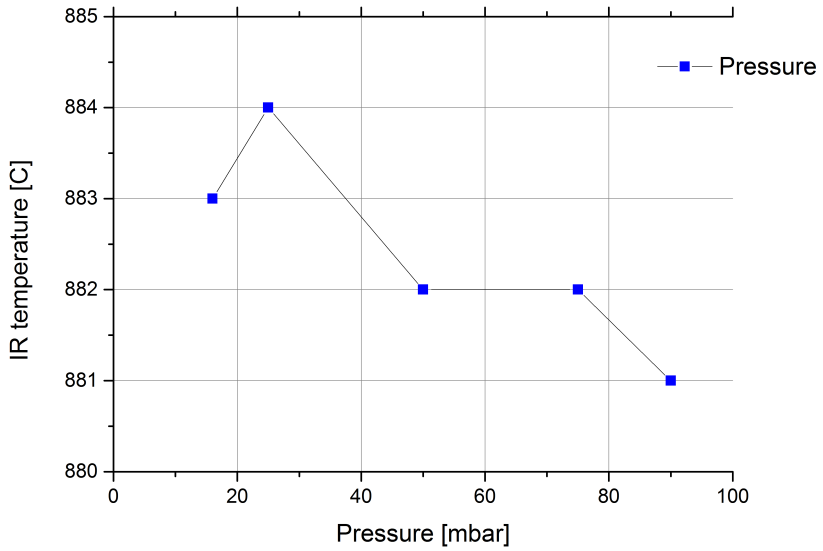

Figure 2.8: Graph of the IR temperature as a function of the total pressure. No appreciable change in temperature is observed for different pressures.

2.2.4 Parameter space

The Black Magic CVD system is built such that there is control over the temperature and ramp rates of the two heaters, top heater and bottom heater, the total pressure of the chamber, and flow rates of individual gasses, H_2, Ar/N_2 and CH_4, etc. With these control parameters in mind recipes are written to satisfy certain conditions needed for CVD graphene growth. A basic recipe contains the following steps:

Preconditioning phase Where the chamber is purged to get rid of unwanted material from the sample loading phase. Gasses, H_2 and Argon/Nitrogen, and pressures are set to desired values.

Annealing phase Where the chamber temperature controllers are loaded with PID values and the temperature is raised to the desired set point and maintained for the set annealing time.

Growth phase Where CH_4 gas is let into the chamber for at set amount of time. At the end of the growth phase CH_4 and H_2 gas flow rates are turned off.

Cooling phase The temperature is lowered at a set rate, the cooling rate, until a temperature, where the sample can be unloaded from the system. Gasses are turned off, e.g. CH_4 or H_2, to suppress further growth or etching during cooling.

For the Black Magic CVD system the range of each individual parameter is presented below for clarity:

Temperature The temperature can be varied from room temperature to 1200 ^{o}C. An automatic shut down of the system is activated, when the measured temperature exceeds 1200 ^{o}C.

Pressure The pressure ranges from 10^{-2} mbar to 700 mbar. The lowest pressure is at vacuum state, while the highest pressure can only be achieved with a nitrogen flow, not with argon (described earlier). The minimum total process pressure achievable in the system is dependent on the total flow rate into the chamber and the base pressure of the pump.

Gasses The following are set points of the flow rates of each gas used in this project.[1]

- Ar/N_2 ranges from 1 sccm to 2000 sccm.
- H_2 ranges from 1 sccm to 1000 sccm.
- CH_4 ranges from 1 sccm to 50 sccm.

[1]Each mass flow controller has an error on the high and low end of the flow range of $\sim$10 %. This means that the achievable flow rates for e.g. methane is between 5 and 45 sccm.

An example process for growing CVD graphene in the Aixtron Black Magic CVD system is seen in figure 2.10. Here the process is shown with all of variables. The process shown in figure 2.10 outlines a constant temperature through out annealing and growth. By implementing variable temperature and/or pressure it is possible to reduce copper evaporation during the long annealing phase of the process. This is achieved by having a lower temperature and a higher pressure during the annealing phase compared to the growth phase. The cooling rate in the process is not controlled, but simply provided by shutting down the heaters and letting the water cooling of the outer chamber work as a heat sink, providing a fast exponential decay followed by a slower exponential decay in temperature, as seen in figure 2.9. The temperature needed for growth ranges from 800 ºC to 1070 ºC, using methane as the precursor gas. The lower limit is caused by the energy needed for methane to decompose on the copper surface and the upper limit is from the melting/evaporation of the copper substrate. These limits can be expanded through changes in the carbon precursor gas and the pressure during processing.

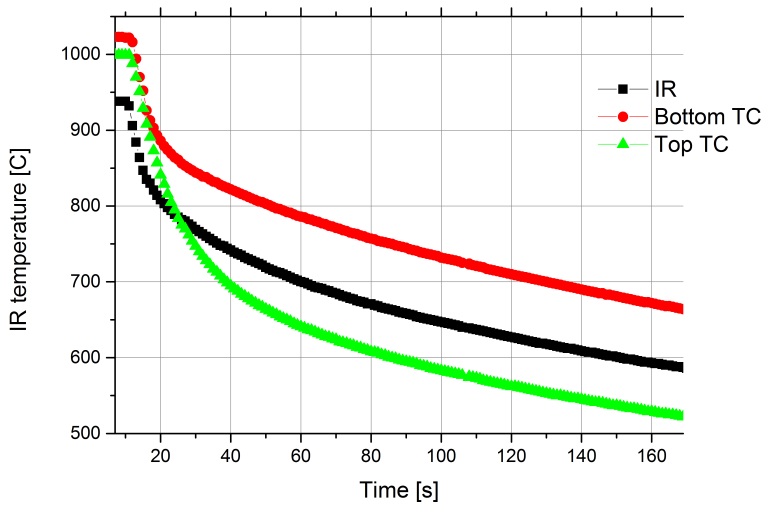

Figure 2.9: Temperature decay versus time, for bottom heater TC, top heater TC, and the IR sensor; as both heaters has been turned off and a stable flow of argon is running at a constant pressure.

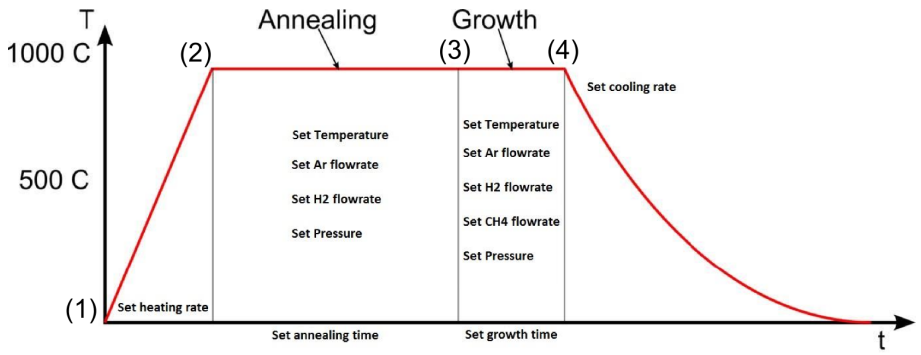

Figure 2.10: An example process showing the variables for graphene growth on a copper substrate. (1) The heating step, where the heating rate and annealing temperature is set, as well as gas flows and pressure can be set here. (2) The annealing step starts when the set temperature is reached. Gas flow rates and pressure can be adjusted. (3) The graphene growth step, which primary goal is the addition of methane. Gasses and pressure can be adjusted here as well. (4) The cooling step, where methane and hydrogen are turned off as well as turning off the heaters or setting a controlled cooling rate (not shown).

2.3 Summary

The Black Magic 4" CVD, cold wall, vertical shower head gas induction, dual heater system, was used in this thesis work. The benefits of this system compared to a hot wall tube furnace lies in the sample sizes which can be processed and the uniformity of the gas flows. Other notable features of this system includes a recipe based processing system which eliminates user based variations. A PID temperature control system is ideal for maintaining a set temperature, though this has been shown to cause problems due to the degradation of the built in thermocouples, due to hydrogen embrittlement and preferential loss of chromium, over time, at elevated temperatures, also causes a downwards calibration drift [20]. With a variable control over the pressure, from a base pressure of 10^{-3} mbar up to 700 mbar processing pressure in N_2, the system is capable of LPCVD recipes and near APCVD recipes.

An equation for temperature calibration has been determined. This will provide users with power levels needed to achieve desired temperatures for annealing and growth of graphene, without relying on PID control. A description of how the argon and hydrogen gas flow rates influence the temperature has been measured. A flow of hydrogen reduces the chamber temperature independent of the flow rate, while an increasing argon flow rate decreases the temperature in the chamber.

The temperatures measured on the built in thermocouples are more than 50 ^{o}C higher than the temperatures measured using the IR sensor and an external thermocouple placed in the center of the chamber. The slope of the temperature measured on the bottom TC is far steeper than the rest of the temperature measurements. This could be due to degradation of the thermocouple, or poor calibration. From the external TC measurements it is seen that the temperature varies by close to 50 ^{o}C from the center to the edge of the sample. This variation a cross a wafer will greatly affect the growth of graphene which is highly dependent on the temperature, as will be described in later chapters of this thesis.

Changing the temperature control from the built in PID controller (using the TCs) to a constant power control over temperature leads to better wafer to wafer reproducibility. A tight control over temperature is needed for industry scale fabrication of CVD graphene.

Chapter 3

CVD graphene on Cu foils

CVD graphene grown on copper foil has the potential to be scalable to any size. Copper foil of many square meters can easily be produced, and a roll-to-roll [4] CVD chamber can grow graphene continuously with large foil samples. This means that centimeter size copper foils can be used for prototyping, which then can be scaled accordingly. In this project I have tested CVD graphene growth on copper foils from two major companies (Goodfellow and AlfaAesar), with varying degrees of purity and cleanliness. Due to contamination of the foils in the form of aluminium oxide particles, from the manufacturers polishing procedures, optimization of a graphene growth recipe for large graphene crystals had limited success. Aluminium oxide particles act as a source of nucleation sites for graphene growth, resulting in many smaller graphene domains, rather than few larger ones. The aim of this work is to (1) grow graphene on a cheap and well established substrate with a quality comparable to exfoliated graphene, and (2) to describe the process of optimization of a recipe for single-layer graphene growth on copper foils with minimum defect density (D/G ratio).

Hypotheses

2a. *The defect density and growth rate depend on the different crystal orientations of the copper catalyst.*

3a. *It is possible to change the shape of the CVD grown graphene flakes by changing the growth conditions.*

4a. *The size and shape of CVD grown graphene flakes depend on the catalyst nucleation site (edge/plane).*

3.1 Growth on Foils

2" Copper foil discs with a thickness of 12.5 µm from Goodfellow with 99.95 % purity, in figure 3.1 (a), as well as copper foil (Alfa Aesar, 10950 - 25 μm Puratronic®, 99.999% (metals basis)) seen in figure 3.1 (b), were ordered. The copper foil from Goodfellow looks to be heavily oxidized or covered in a dark film, which is not the case for the foil from Alfa Aesar. Foil choise was based on visual inspection and SEM, in figure 3.1, as well as EDX measurements before and after graphene growth (appendix C). SEM images show how the surface of the Goodfellow foil is more rough than the Alfa Aesar foil, figure 3.1 c and d. EDX measurements show aluminium oxide particles on the Alfa Aesar foil before growth, while the foil from Goodfellow shows regions with silicon and calcium after growth of graphene, appendix C. Due to lower surface roughness and no amount of silicon or calcium, copper foil from Alfa Aesar was chosen for the optimization of a graphene growth recipe in the BM CVD system.

This section will describe the first attempt at optimization of a graphene growth recipe on copper foil (Alfa Aesar, 10950 - 0,025 mm Puratronic®, 99.999% (metals basis)), using the BM CVD system. Micro Raman point spectroscopy was used as the characterization technique. The 2D/G ratio was used as a measure of layer numbers, with higher ratio meaning closer to single layer graphene. The D/G ratio was used to detect the defect density of the graphene film, with a lower ratio meaning lower defect density. The micro Raman spectra of the graphene was collected, while still situated on the copper foil.

The Raman characterization is supplemented with SEM images of the graphene grown on the copper foil. Optimization was carried out by sweeping one input parameter while keeping the rest constant, and measuring the output signal, as described above. The input value of the swept parameter giving the best output signal was chosen, in this case highest 2D/G ratio and lowest D/G ratio. This was done for the following parameters: Temperature, methane flow rate, hydrogen flow rate, argon flow rate, pressure, and time. The parameter space explored in this chapter can be seen in table 3.1. The graphene growth recipe used for this optimization has the form shown in figure 3.2. The recipe has a fixed heating rate of 200 °C/min up to the annealing temperature in a vacuum atmosphere, and a constant total flow rate of 600 sccm of a mixture of Ar, H_2 and CH_4 during the growth phase. The annealing step contains hydrogen for cleaning the surface through removal of both native copper oxide and hydrocarbons on the surface.

Parameter	minimum value	maximum value	optimum value
Temperature	970 °C	1050 °C	1000 °C
CH_4 flow rate	2 sccm	50 sccm	10 sccm
H_2 flow rate	0 sccm	100 sccm	20 sccm
Ar flow rate	0 sccm	200 sccm	0 sccm
Pressure	5 mbar	75 mbar	20 mbar
Time	15 s	600 s	600 s

Table 3.1: Table showing the parameter space investigated in the optimization of graphene growth via CVD on copper foils in the BM. The ranges were chosen based on recipes from Aixtron and Jie-Sun from Chalmers University.

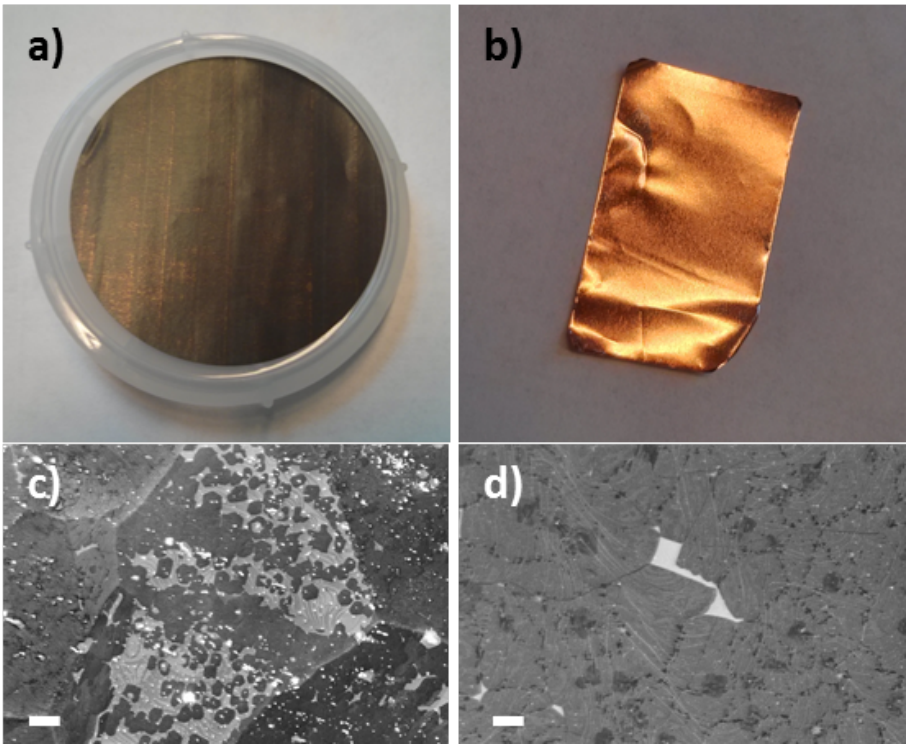

Figure 3.1: a) 2" Cu foil disc from Goodfellow (99.95% purity). b) a piece of Cu foil from Alfa Aesar (99.999 % purity). c) SEM micrograph of Goodfellow copper foil after a graphene growth recipe. d) SEM micrograph of Alfa Aesar copper foil after the same graphene growth recipe. Scale bars corresponds to 2 μm.

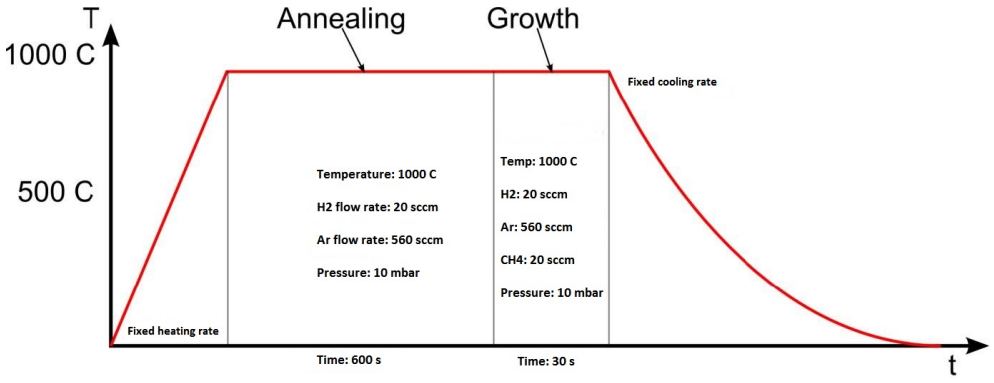

Figure 3.2: Example recipe in the BM, for graphene growth on copper foil. Parameters are set in the recipe before the process begins. Typical process length of graphene growth on Cu foil is 2-3 hours depending mostly on annealing time and heating/cooling rates.

3.2 Raman characterization

Raman characterization of CVD graphene on copper foil was carried out using single spectra, rather than maps. This was due to the large surface roughness of the copper foil, induced by the polishing process during the fabrication of the foil, leading to intensity variations in the Raman maps. The built-in optical autofocus system of the Raman microscope was not able to correct for this issue, because it tries to focus the entire field of view, not taking in to account the variations within this region. The system also has the capability of using the Raman signal for autofocusing. This technique requires a strong peak signal, large enough for the software to pick up during live spectrum recording. The live signal of graphene, with the 532 nm laser and 50x objective was not sufficient for this task.

In the following optimization of a graphene growth recipe the 2D/G ratio as well as the D/G ratio are used as measurements of crystal quality. The error bars correspond to one standard deviation, with the smallest sample size being 3 measurements, though generally . The Raman spectra are all collected using a 532 nm excitation laser and a 50x objective giving a spot size of about 1 µm.

3.2.1 Temperature

First the temperature was varied from 970 °C to 1050 °C with all other parameters held constant. This yielded the results shown in figure 3.3 providing the defect density. A slight increase in mean 2D/G value is seen with increasing temperature. The defect density shows no variation with temperature. The measurements collected on the sample grown at 1040 °C show an anomalously low 2D/G ratio, and high D/G ratio compared to the other temperatures. This will be explained in the SEM characterization. Following the temperature optimization step a limit of 1000 °C was imposed to limit the evaporation of copper into the chamber.

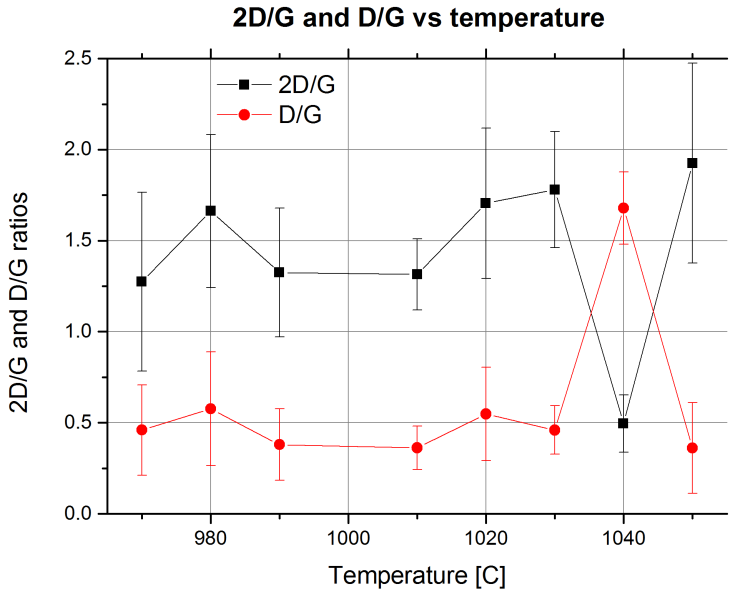

Figure 3.3: Raman 2D/G and D/G peak ratios plotted as function of temperature. The 2D/G ratio above 1 approximately corresponds to single layer graphene.

3.2.2 Methane flow rate

Setting the temperature at 1000 °C and all other parameters constant; the methane (CH_4) flow rate was dialed from 2 - 50 sccm showing no significant change in the mean 2D/G ratio, seen in figure 3.4. For 15 and 20 sccm of CH_4 there is a significantly lower variation in the measured ratio. The D/G ratio has a minimum value at 10 sccm. Increasing or decreasing the methane flow rate from this value increases the D/G ratio, seen in figure 3.4. A larger variation is seen in the defect density for very low flow rates of CH_4.

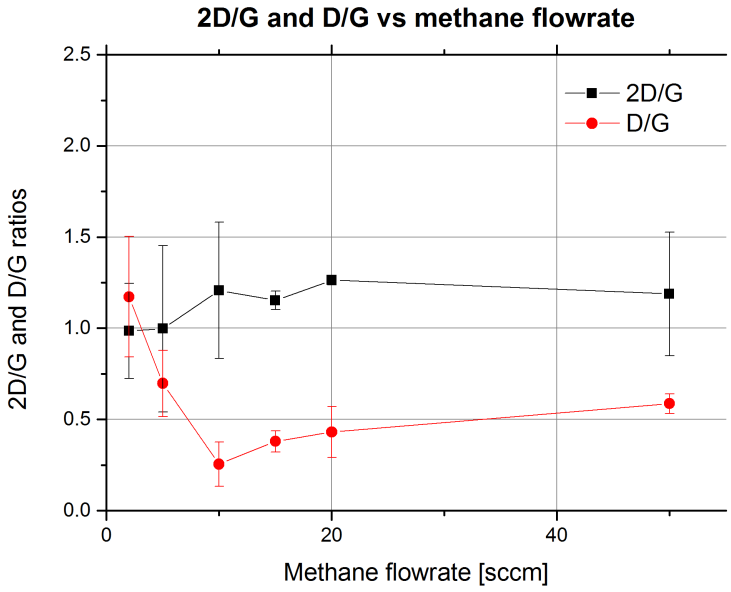

Figure 3.4: Raman 2D/G and D/G peak ratios plotted as function of CH_4 flow rate.

3.2.3 H_2 flow rate

The hydrogen flow rate was varied from 0 - 100 sccm, and the intensity ratios can be seen in figure 3.5 left graph shows the 2D/G ratio as a function of hydrogen flow rate, the right shows the D/G ratios. The measurements show no change in either the 2D/G or the D/G ratio as a function of H_2 flow rate.

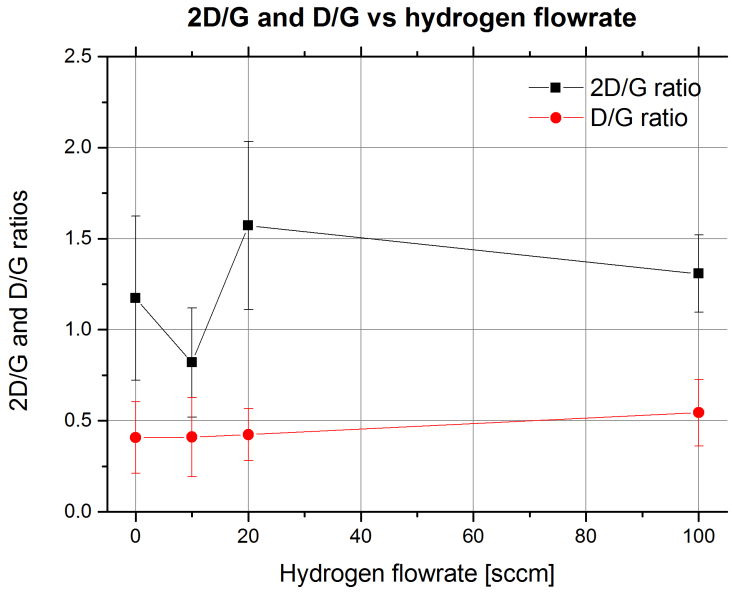

Figure 3.5: Raman 2D/G and D/G peak ratios plotted for four different H_2 flow rates.

3.2.4 Argon flow rate

The role of the argon flow is as an inert carrier gas, as well as another way of varying the partial pressures of the hydrogen and methane without having an influence on the doping level of the graphene. Changing the argon flow rate during the growth phase from 0-200 sccm, shows a high 2D/G ratio for no flow of argon. The mean D/G ratio increases with increasing flow of argon as seen in figure 3.6. During the optimization of the argon flow rate the total flow rate was also changed, instead of increasing the hydrogen and methane flow rates to compensate.

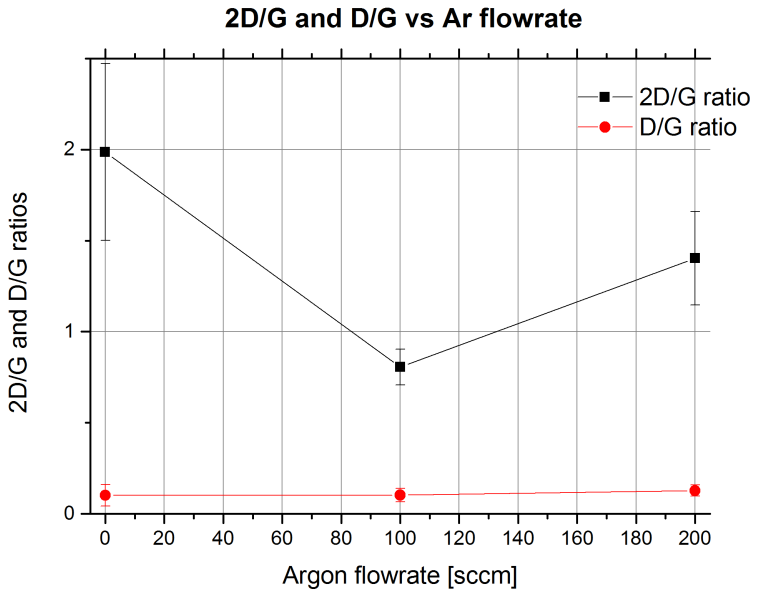

Figure 3.6: Raman 2D/G and D/G peak ratios plotted for three different argon flow rate.

3.2.5 Pressure

Changing the chamber pressure during growth from 5 to 75 mbar yielded the results shown in figure 3.7. The left graph shows the 2D/G ratios, the right shows the D/G ratios. The 2D/G ratio shows a maximum at 20 mbar pressure, while the D/G ratios shows a minimum at 40 mbar pressure. The D/G ratio has two outliers at 30 mbar and 75 mbar, which could be due to fitting issues of the D peak on these samples.

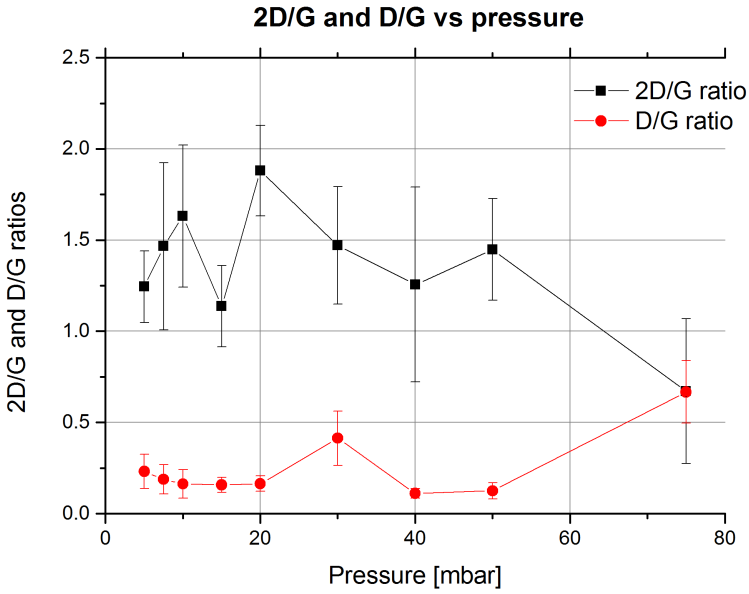

Figure 3.7: Raman 2D/G and D/G peak ratios plotted as function of pressure.

3.2.6 Time

By varying the growth time of the recipe from 10 to 600 seconds a slight increase of the 2D/G ratio is seen in figure 3.8. The D/G ratio shows very slight decrease with increasing growth time as seen in figure 3.8. A very high D/G ratio is seen for 60 s growth time which doesn't fit with the rest of the measurements.

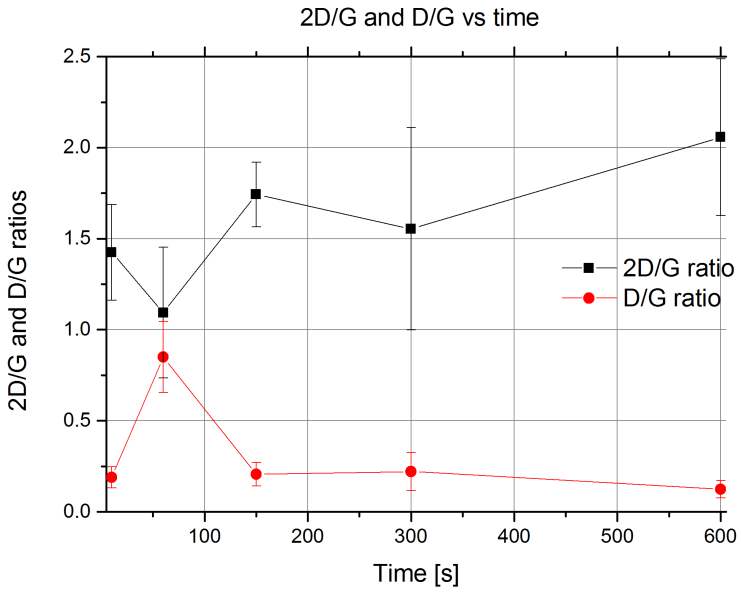

Figure 3.8: Raman 2D/G and D/G peak ratios plotted as function of time.

3.2.7 Summary of Raman characterization

To sum op the optimization I found that the methane flow rate showed a minimum defect density (D/G ratio) at 10 sccm. The hydrogen flow rate was found to not affect the 2D/G or the D/G ratios for the chosen range of flows. By turning off the flow of argon during the growth phase the highest 2D/G ratio a the lowest D/G ratio was found. The optimum growth pressure was found to be 20 mbar, and 600 seconds growth time gave the highest 2D/G and lowest D/G ratios. As for temperature, higher temperatures does seem to produce the highest 2D/G ratios, while no change was seen in the D/G ratio. Though with the variations seen in all of the measurements a definite conclusion of the maxima for the parameters was not found.

3.3 SEM characterization

Characterizing the surface of the copper foil after annealing, a few things become apparent right away - the surface of the copper foil is littered with particles, as seen in figure 3.9 (right), and the surface has polishing marks seen as straight lines running over the sample, in figure 3.9 (left). As for the graphene grown on the foil, figure 3.10 (top) shows low resolution SEM of graphene grown at 970 °C, 1020 °C, and 1050 °C (set point temperatures) and figure 3.10 (bottom) shows higher resolution micrographs of the same samples. In the low temperature growth the graphene does not cover the entire surface of the foil. Separated graphene domains can be seen in the high resolution image. For the high temperature growth the surface of the foil is completely covered with graphene.

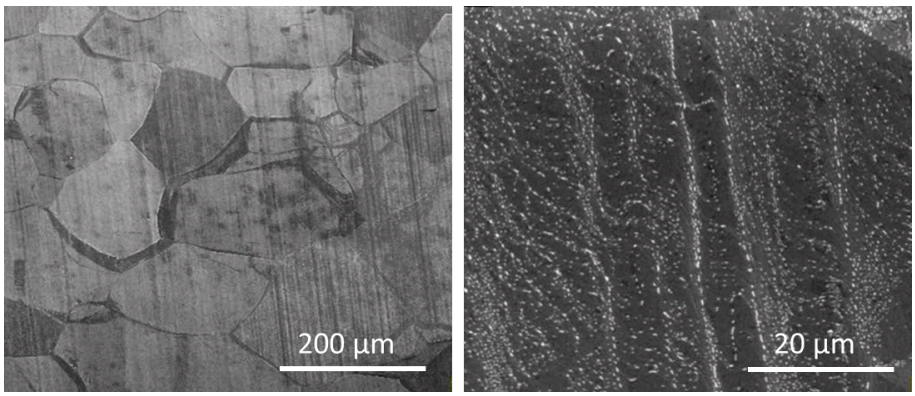

Figure 3.9: SEM images showing copper foil after annealing at high temperature. Left: Copper domains are seen as regions with different contrast, the vertical lines in the image are polishing marks from the fabrication process. Right: The bright spots are aluminium oxide particles from the polishing procedure.

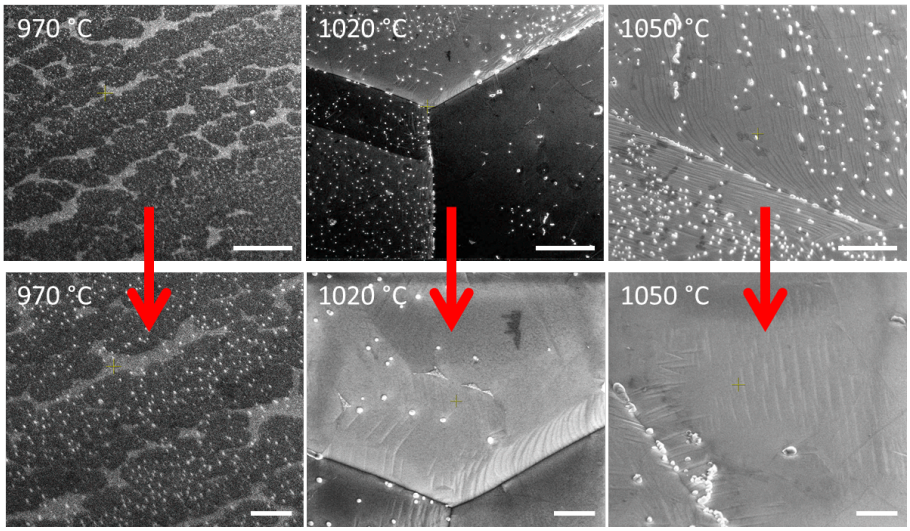

Figure 3.10: Top row(left to right): SEM images showing graphene growth on copper foil at three different temperatures, 970 °C, 1020 °C, and 1050 °C (the scale bar represents 3 μm). Bottom row(left to right): SEM images showing graphene growth on copper foil at three different temperatures, 970 °C, 1020 °C, and 1050 °C (the scale bar represents 500 nm).

Graphene grown at 1000 °C for 10 and 600 seconds can be seen in the figure 3.11. These images show that with these growth conditions, 10 seconds of growth lead to an incomplete coverage of graphene, while 600 seconds growth lead to full coverage. This result fits with the observed Raman measurements showing high 2D/G ratio and a low D/G ratio.

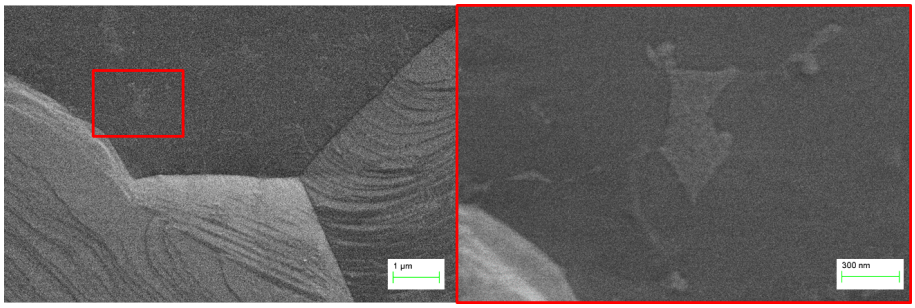

Figure 3.11: Left: SEM image showing partial coverage of graphene grown at 1000 °C for 10 seconds. Right: A zoom in, showing a bare copper patch (light grey region) surrounded by graphene.

The surface of the 1040 °C sample was investigated in SEM due to the very low 2D/G ratio and very high D/G ratio as described earlier. In figure 3.12 (left) it can be seen how the surface is littered with spherical areas of high density particle clusters. Figure 3.12 (right) shows a zoom in on the edge of one of these clusters, where different particle sizes can be seen. This phenomenon was witnessed everywhere on the sample surface and is very different compared to any of the other samples. All the copper foil samples were cut from the same master piece of foil. The particles observed are aluminium oxide as identified by EDX measurements, found in appendix C.

3.3.1 Particles

An investigation of the origin of the particles was carried out. This was done by folding a piece of copper foil to an almost sealed pocket and comparing the inside 3.13(right) and outside 3.13(left) of the foil. It was found that the inside of the foil did not have a reduced the number of particles, compared to the outside of the foil. This indicates that the particles found on the surface of the foil originates from the manufacturing process of the foil and not the CVD chamber.

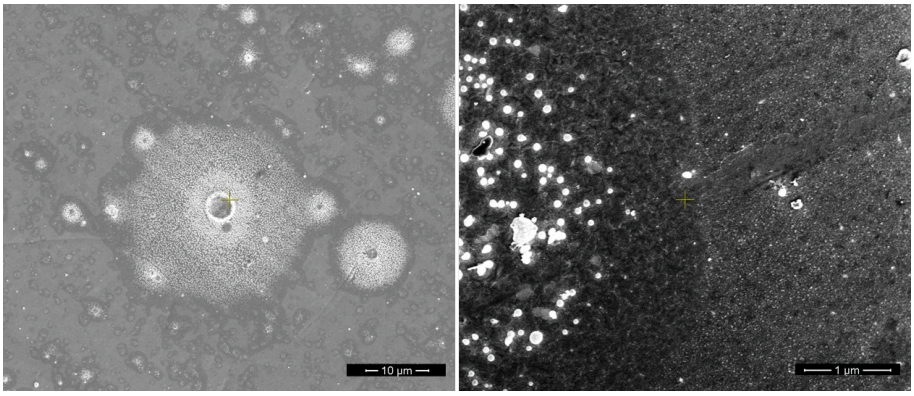

Figure 3.12: SEM images of the surface of a copper foil after graphene growth at 1040 °C. Left: The surface shows impact like craters. Right: an abundance of particles littered on the surface.

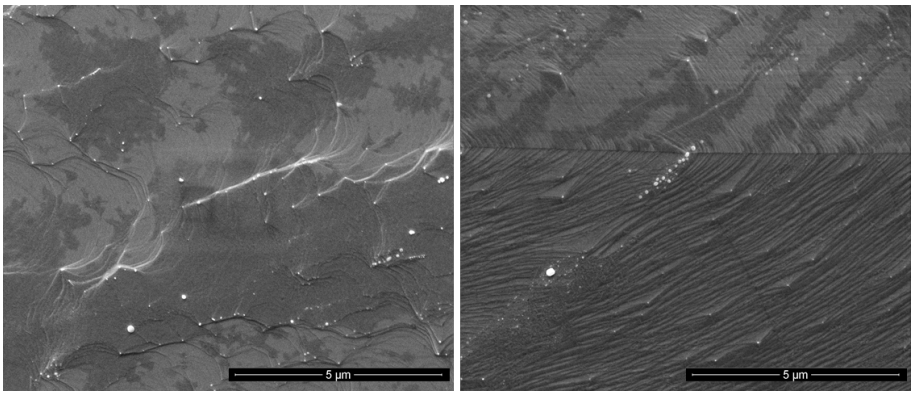

Figure 3.13: Left: SEM image of the outside of a folded piece of copper foil. Right: SEM image of the inside of a folded piece of foil after CVD graphene growth.

3.4 EBSD characterization

EBSD mapping is used to characterize the crystal orientation in the copper foil. A map of the image quality (IQ), and the inverse pole figure (IPF), shows the quality of the collected measurements and the calculated crystal orientation of the copper foil respectively, see figure 3.14. By overlaying the two maps it becomes relatively easy to get an overview of which crystal orientations have the best image quality, and thereby the flattest and cleanest surface. From the IPF map it is seen that the dominating crystal orientation of the copper foil is the (001) direction. This is known of this type of copper substrate due to the fabrication of rolling to a thin foil and annealing, which promotes the (001) orientation [58] [106]. The IQ map shows that many of the crystal domains in the foil have a poor signal, which is due to both the roughness and the contaminants/oxidation of the surface, as seen by SEM previously.

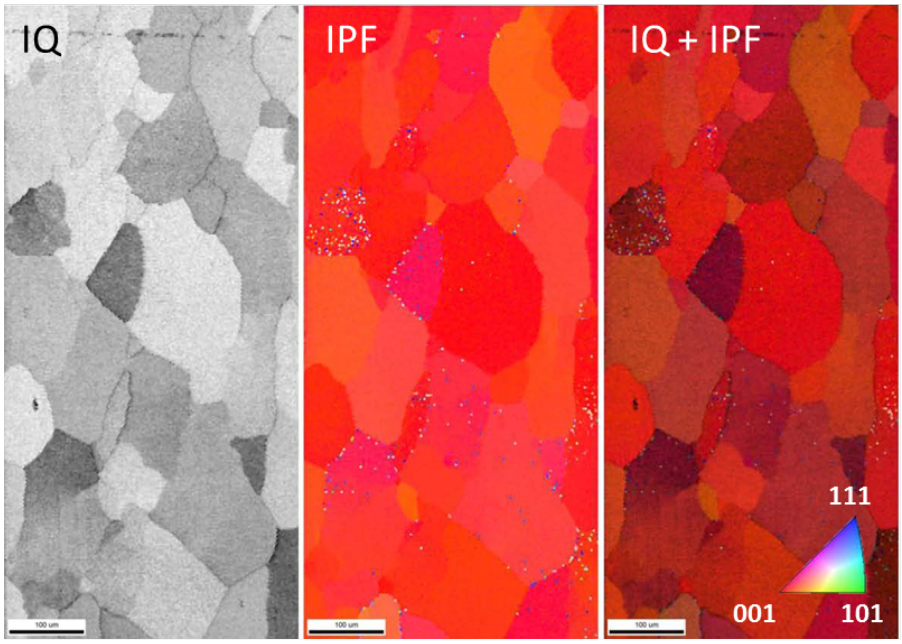

Figure 3.14: EBSD map of the IQ map, the IPF map and IQ with IPF overlay map of Cu foil. (001) is the dominant crystal orientation.

3.5 Discussion

In this work I optimized a recipe for growing single layer graphene on copper foil. The goal of the optimization was to establish a recipe, which resulted in graphene with a high 2D/G ratio and a low D/G ratio (defect density).

Optimization of the graphene growth recipe showed an increase in the 2D/G ratio (higher likelihood of single layer graphene) and a slight decrease in the D/G ratio (defect density) as a function of temperature. This is supported by literature [114] [135] [12] [69], where higher growth temperature leads to lower defect density, which can be attributed to a lower nucleation density leading to fewer grain boundary defects. Within the range of methane flow rates tested, a slight increase in 2D/G ratio for increasing flow rates is observed. The D/G ratio showed a minimum value for a methane flow rate of 10 sccm. From a previous study, it was found that a high ratio of the partial pressures of hydrogen and methane (P_{H2}/P_{CH4}), results in smaller graphene grains [114]. Therefore it is expected that a higher methane flow would result in larger graphene grains leading to lower D/G ratio, which was not the case here. Here it is observed that the lowest D/G ratio is found for a P_{H2}/P_{CH4} ratio of 5. In another study they find, that decreasing the flow rate and partial pressure of methane, decreases the nucleation density [69]. For a fixed growth time, a low flow rate would lead to lower graphene coverage, resulting in an increased D/G ratio.

When changing the background pressure from 5 to 75 mbar, it was found that a pressure of 20 mbar yielded the highest 2D/G and lowest D/G ratios. In [114] they found LPCVD conditions leading to lower nucleation density and higher coverage compared to APCVD conditions.

The measurements show no change in either the 2D/G or the D/G ratio as a function of H_2 flow rate. This is counter to what is expected, where increasing H_2 flow rates should decrease the D/G ratio as increased preferential hydrogen etching should occur with increasing flow.

Particles on the surface of the copper film act as a nucleation site for graphene growth. I proved that the particles originate from within the copper foil and not from the BM chamber. This was demonstrated by comparing two pieces of copper foil, one was folded to a sealed pocket, the other was not. The inside of the folded piece of foil showed a similar amount of particles than foil without folding after growth of graphene.

The success of the optimization of a graphene growth recipe was ultimately limited by the reproducibility of results mainly contributed by the poor temperature control (described in chapter 2), as well as the inconsistency of the studied copper foils, in terms of roughness and contamination.

That being said, the tendencies are that higher temperature, long growth time and low partial pressure of argon leads to higher quality graphene. When edges are present they can act as sites for phonon scattering, resulting in an increased D peak in the Raman spectrum. The D peak intensities for high temperature or long growth times are most likely reduced, due to larger graphene grains at high temperatures or higher coverage of graphene during long growth times. The high coverage results in a lowering of the number of edge sites available for scattering, if the graphene grains are larger.

The contamination from aluminium oxide particles of the copper foil has had such an impact on the growth of graphene, that the obtained results do not compare with what has been found in literature [114] [68] [19] [116], where they use extensive cleaning methods to obtain a usable copper surface. Chemical and electrochemical pre-cleaning of copper foil are methods described in literature, as ways to circumvent the issue of the contamination [114] [59] [17] [127]. Some of these methods have the drawback of etching the copper foil (in nitric acid), thereby releasing the contaminations, this can lead to roughening of the surface (another source of nucleation sites).

Growth of graphene on thin copper films deposited on a SiO_2/Si wafer, has been shown to yield high quality graphene [109] [36] [44] [67]. Growth of graphene on copper films on wafers, is still a new area for fabrication of CVD graphene. There is a lot of potential for CVD graphene on wafers i.e. graphene on wafers will scale with the current industry fabrication of electrical devices, such as transistors, touchscreens and micro-electro-mechanical (MEMS) devices like gas sensors etc if a reliable transfer method is developed. In the following chapter I will describe the process of optimizing a graphene growth recipe on copper thin films on SiO_2/Si wafers.

Chapter 4

CVD graphene on Cu films

The main objective of the work described in this chapter was optimization of growth of graphene on copper thin films on 4-inch SiO_2/Si (and sapphire wafers detailed in chapter 5). Copper thin films do not pose the same issues as copper foils in terms of particles and surface roughness. They do however integrate well with current wafer scale device fabrication, since they can be scaled to fit with every size of wafers.

Growing graphene on copper thin films on wafers avoids the particles observed on the copper foils, as well as reducing the surface roughness. Graphene grown on wafers also integrates well with other standard cleanroom equipment e.g. lithography and reactive ion etching tools. Copper is known to form a eutectic with silicon forming a copper silicide if the copper comes in contact with the silicon wafer at elevated temperatures. The copper silicide has a very different expansion coefficient than silicon and in several instances shattered a wafer. This was seen after the processing when the CVD chamber was opened. Copper silicide particles are also a source of nucleation sites for the CVD graphene, which was shown previously to diminish the quality of the graphene grown. These negative effects of the copper silicides can be avoided if the underlying SiO_2 layer is thick enough that the copper does not diffuse through it. If Cu binds to silicon, forming copper silicides, and resurface on top of the copper layer it increases the surface roughness [94]. Different expansion coefficients of silicon and copper silicides increases the likelihood of shattering the carrier wafer when cooling down from a high temperature. In my project a thickness of 1 µm was found to be sufficient, to negate copper silicides from forming.

A graphene growth recipe was adapted from [110], where CVD graphene

is grown in a similar system to the BM system used in this project. Key differences in the processes is the thickness of oxide used on the silicon wafers, where a 300 nm oxide is used in [110]. I have used a 1 µm thick oxide to avoid diffusion of copper atoms into the silicon wafer. The copper silicide structures reported in [94] was not seen with this oxide thickness. Another reason for increasing the oxide thickness was to remove the possibility of silicon atoms diffusing to the surface of the copper creating more nucleation sites for the graphene growth [44]. Particles on the surface of the copper was one of the main problems with poor quality graphene growth on copper foils.

Hypotheses

1b. *The copper crystal size and orientation depends on the interface between the carrier wafer and a deposited copper thin film, and the annealing temperature.*

2b. *The defect density of CVD graphene is dependent on the growth parameters e.g. temperature and gas flow.*

3b. *The graphene domain size depends on the catalyst domain size.*

4b. *The defect density and growth rate depend on the different crystal orientations of the copper catalyst.*

4.1 SEM characterization

Figure 4.1(top) shows a single layer hexagonal graphene flake, which has grown across a copper grain boundary without any change in geometry. This was also reported in [127]. Figure 4.1(bottom) shows how the geometry or the growth rate is not affected by crystal twinning in the copper catalyst surface. Flakes of varying sizes and shapes are found growing equally on crystals and their corresponding twin planes, on facets as well as on grain boundaries.

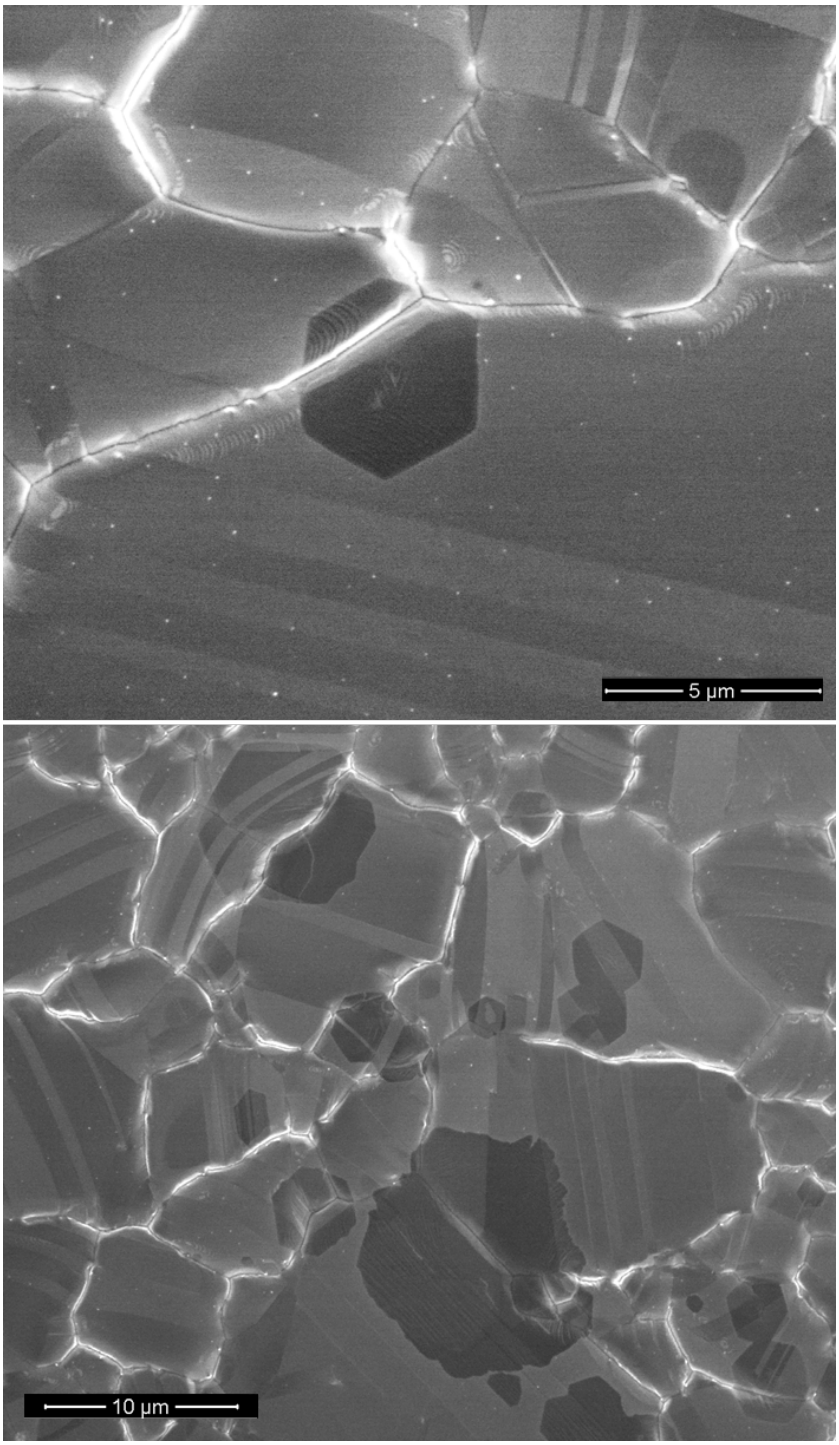

Figure 4.1: Top: SEM micrograph a single layer hexagonal graphene flake on a Cu thin film. Bottom: SEM micrograph of single layer graphene flakes grown on different crystal orientations and twin planes. Graphene flakes are capable of growing across copper grain boundaries.

4.2 Raman characterization

The quality of the graphene film grown on copper thin films is investigated using Raman spectroscopy, see figure 4.2. Defects, strain, doping level, edge type, etc of the graphene can all be extracted with Raman spectroscopy. By utilizing the micro-Raman mapping technique it is possible to determine the uniformity of the film, in terms of the strain, doping, and defect density etc [65]. Mapping of as grown CVD graphene on the copper thin film catalyst can potentially provide information in terms of the effect of the catalyst crystallinity and roughness.

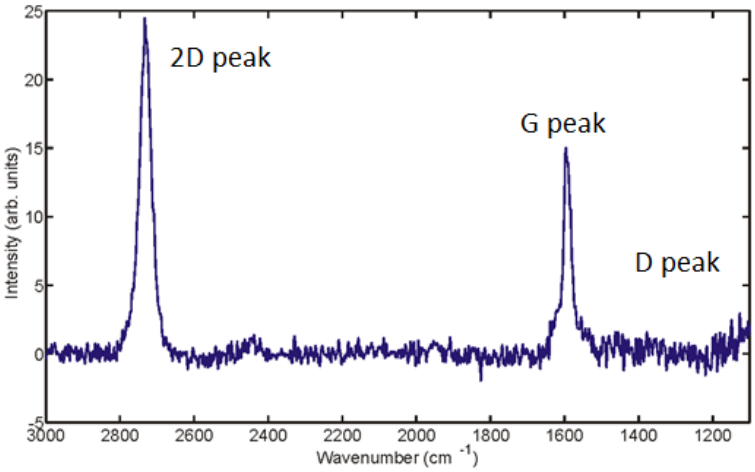

Figure 4.2: Raman spectrum of CVD graphene on copper film on a SiO_2/Si wafer. The 2D, G, and D peaks are indicated. Distinct lack of a D peak in the spectrum is observed (very few to no defects).

As described in the introduction, one measure of the crystal quality of a graphene film is the defect density, which describes the density of lattice defects through the Raman I(D)/I(G) ratio, as seen in figure 4.3 and 4.4. The two graphene samples were grown to form isolated graphene crystals (partial coverage) at different pressures, 75 mbar and 50 mbar respectively. The graphene was grown to a partial coverage in order to be able to visualize individual graphene crystals, and the copper grains on which they were grown. It can be seen by comparing the I(D)/I(G) ratio of each graphene flake on either of the two samples that the defect density does not depend on the crystal face on which it is grown. The sample shown in figure 4.4 shows as well no change in growth rate on different crystal grains. The

sample in figure 4.3 shows that the nucleation density for this particular growth to some degree depend on the crystal orientation. The large center grain has fewer nucleation sites than its surrounding neighbor grains. The sample in figure 4.4 shows a very low 2D/G ratio in one half of the left crystal compared to the other half of the same crystal. The D/G and the FWHM(G) maps do not show any variations for this particular part of the graphene flake.

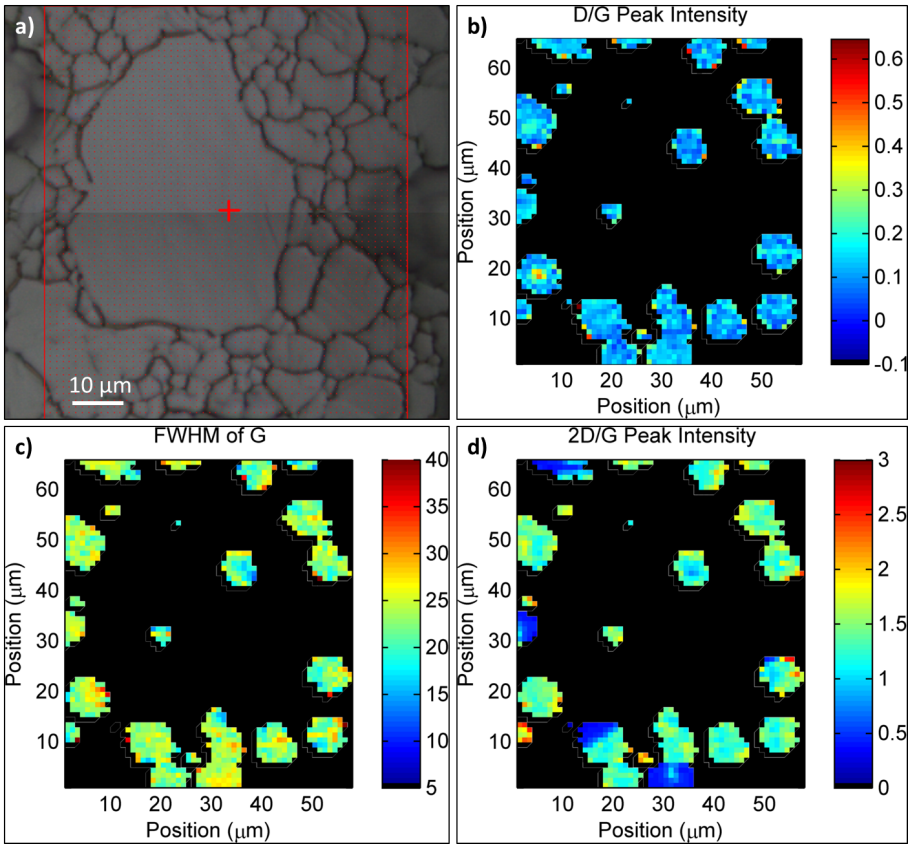

Figure 4.3: Graphene grown at 75 mbar pressure and short growth time to achieve partial coverage of graphene. a) Optical image of the Cu surface, where the Raman map was collected. b) Raman D/G ratio showing no significant change in defect density of the graphene flakes grown on different copper grains. c) FHWM of the G peak showing low doping level. d) 2D/G peak ratio showing how the left graphene crystal is split into two regions. Black corresponds to no signal/no graphene.

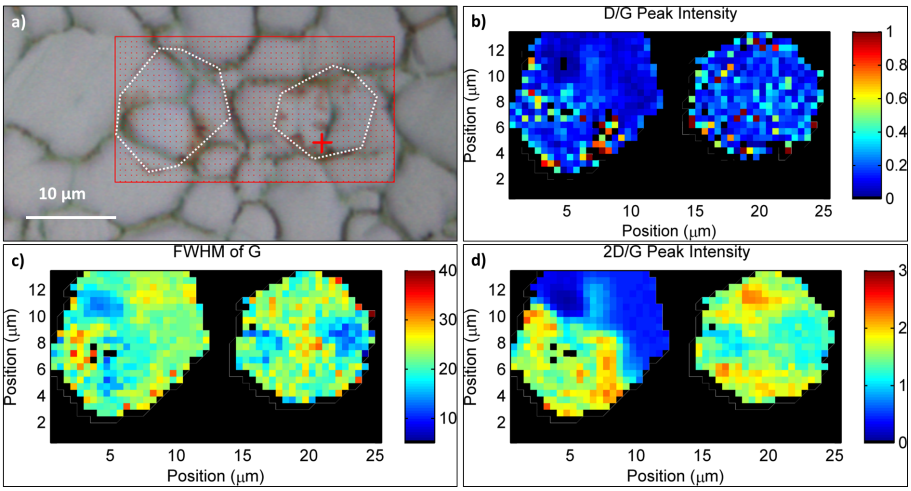

Figure 4.4: Graphene grown at 50 mbar pressure and short growth time to achieve partial coverage of graphene. a) Optical image of the copper surface, where the Raman map was collected. b) Raman D/G ratio showing no significant change in defect density of graphene flakes from one copper crystal to another. c) FHWM of the G peak showing low doping level. d) 2D/G peak ratio shows how some graphene crystals are split into two regions, maybe due to variations in the Cu surface. Black corresponds to no signal/no graphene.

4.3 EBSD characterization

EBSD characterization of annealed Cu thin films on an SiO_2/Si substrate can be used to determine the crystallographic orientations on the surface. Figure 4.5 shows two inverse pole figure maps (IPF) overlayed on image quality maps (IQ) at high temperature (left) and low temperature (right) temperature. The maps show the temperature dependence on the grain sizes and the area fraction of different copper crystal directions. From the figure it can be seen that the larger the grains become the greater the probability of Cu(111) orientation of the crystals (blue corresponds to Cu(111)). The growth of the crystals in the film follows an Ostwald ripening process, where larger crystals consume the smaller crystals, changing their orientation to the dominant one, in this case (111). In figure 4.6 the IPF map is split into the three major orientations, (100), (101), and (111), and the graph shows how (100) and (101) orientations are nonexistent beyond grain areas greater than 70 μm^2.

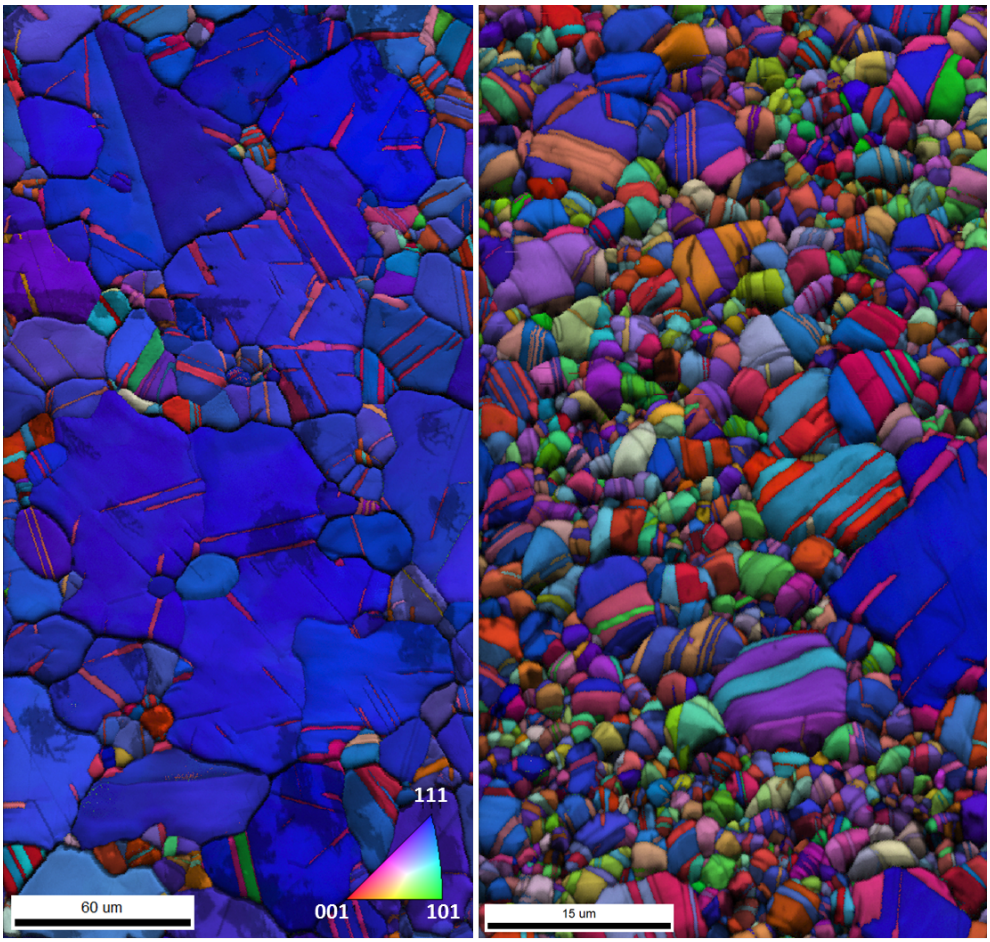

Figure 4.5: EBSD of the IPF map overlayed on the IQ map, showing the temperature dependence of the area fraction of Cu(111) on a SiO_2 wafer. Copper annealed at high temperature (left) and low temperature (right). Larger grains are observed at high temperature as well as a higher area fraction of Cu(111) compared to low temperature, where grains are smaller and the Cu(111) area fraction is significantly lower.

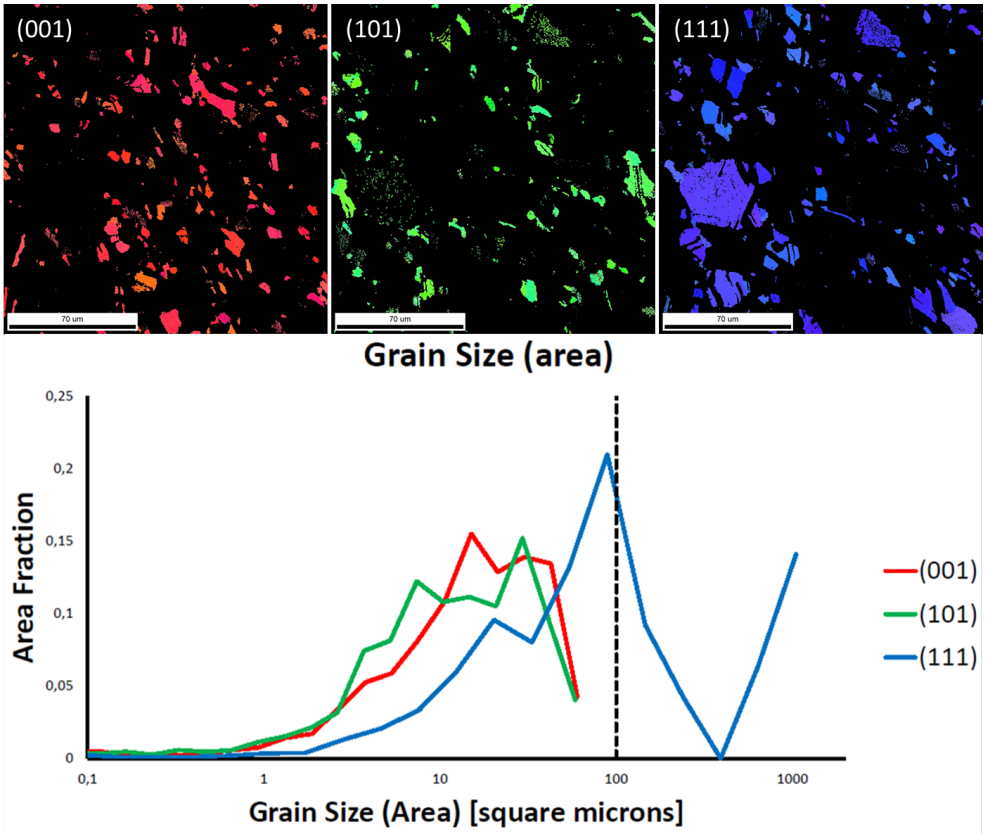

Figure 4.6: IPF showing the area fractions of (100), (101), and (111) on a copper thin film after growth of graphene involving a high temperature annealing. Bottom graph shows the area fraction as function of grain size of the three orientations. It is seen how the Cu(111) orientation dominates, when grain area increases beyond 70 microns^2. Continuous lines are used to represent discrete data points in the EBSD software.

Direct EBSD measurements of graphene is not possible due to the high acceleration voltages generally needed for EBSD (15 keV). At this high voltage the backscatter electrons readily pass through the graphene sheet, which in turn do not contribute to the EBSD signal used for analyzing the crystal structure of the material. By conducting an EBSD study on a polycrystalline copper film with a partial growth of graphene, seen in figure 4.7, it was found that graphene becomes visible due to the reduced copper oxidation process, beneath the graphene and thereby increasing the image quality in the IQ maps. The IQ or IPF maps do not provide any crystallographic information, but it can provide insights into graphene crystal size as a function of the catalyst substrate crystal orientation. In figure 4.7 it is seen how the graphene crystals are smaller on Cu(111) oriented grains compared to Cu(101) and Cu(100) oriented grains.

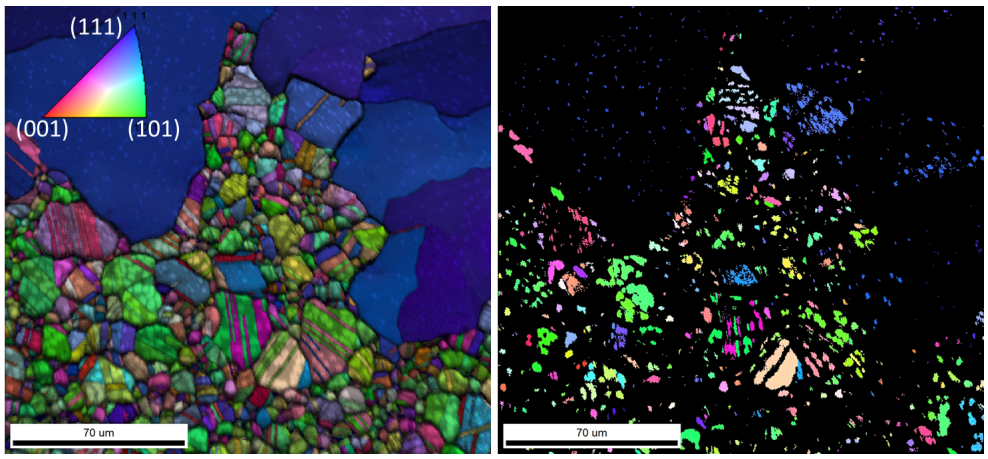

Figure 4.7: IPF map overlayed on IQ map (left) and IPF map with better than 50% filtered IQ map (right). This shows how the signal in the IQ map is increased, when graphene is covering the surface of the copper.

4.4 Optical characterization

This work was carried out in collaboration with Mathias Mølgaard, where I played a supervisory role.

In this section, optical characterization is used to give an estimation of the distribution of the poly-crystalline copper grain size. The copper grains are analyzed by recording optical microscope images of the copper surface and using an image processing software (ImageJ) to convert the images to area data. First the images are converted to binary (black and white), and then using a Voronoi script, see figure 4.8 (making the grain boundaries one pixel thin) followed by an inversion and a particle analysis script. This routine gives an estimation of the size distribution of the crystal grains. This is done on three to four images per region to minimize artifacts in the microscope images.

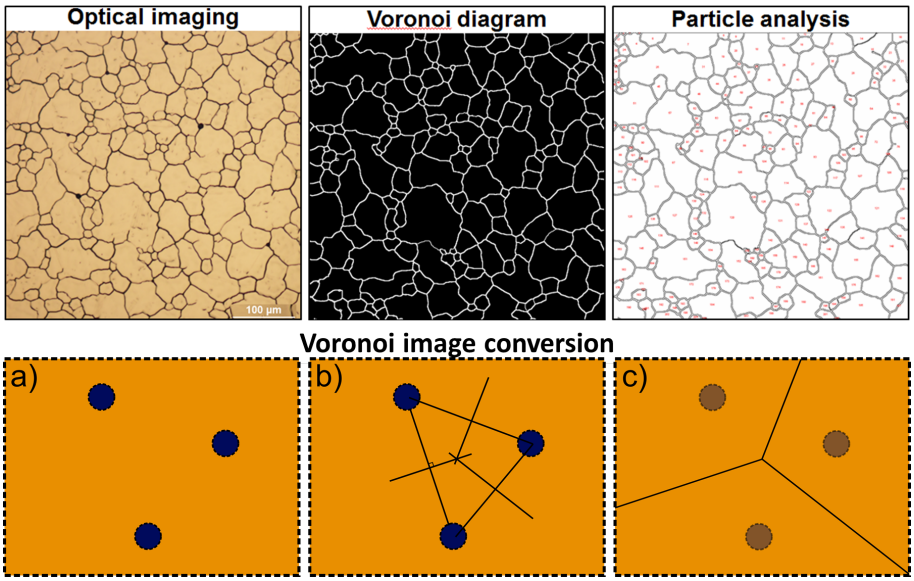

Figure 4.8: (top) Visual representation of the particle analysis routine using ImageJ software. From left to right, optical image, Voronoi diagram, particle count. (bottom) Schematic showing a Voronoi diagram. a) depicts an image of three particles, b) shows how the image is divided into Voronoi cells, and c) shows the final Voronoi cells.

The size distribution is plotted as histograms (logarithm of the area) for

different growth temperatures in figure 4.9 (left) and different growth times in figure 4.9 (right). The growth time was varied from 5 to 180 minutes (at 1000 °C PID controlled). The annealing temperature series ranges from 900 °C to 1000 °C in steps of 20 °C, in a hydrogen and argon atmosphere at 10 mbar pressure. The grain distribution represents the center of the wafers.

Since very small grains are not observed in the microscope a "resolution" limit has been chosen as 2 by 2 pixels. For images recorded at 20x magnification this resolution limit corresponds to an area of $1\mu m^2$. This is presented as a vertical red line in the histograms plotted in figure 4.9. The same approach is done for images recorded at 50x magnification resulting in a minimum threshold of -1.8 on the ln-axis. Since the copper grains has a large variation due to processing conditions, the optical images are recorded at different magnifications leading to varying resolution limits displayed in the histograms.

From a study of Ostwald ripening theory it is shown that the grain areas should be log-normally distributed [96]. Though in studies from 2001 and 2002 they argue that the cluster distribution approximates an exponential [76] [75]. The mean grain area for the time and temperature series is shown in figure 4.10 (bottom) and 4.10 (top) respectively. The data is fitted with a log-normal distribution, which fits the data to a high degree for small to medium sized grains, but does not fit well for larger grains. An exponential fit is included as a comparison.

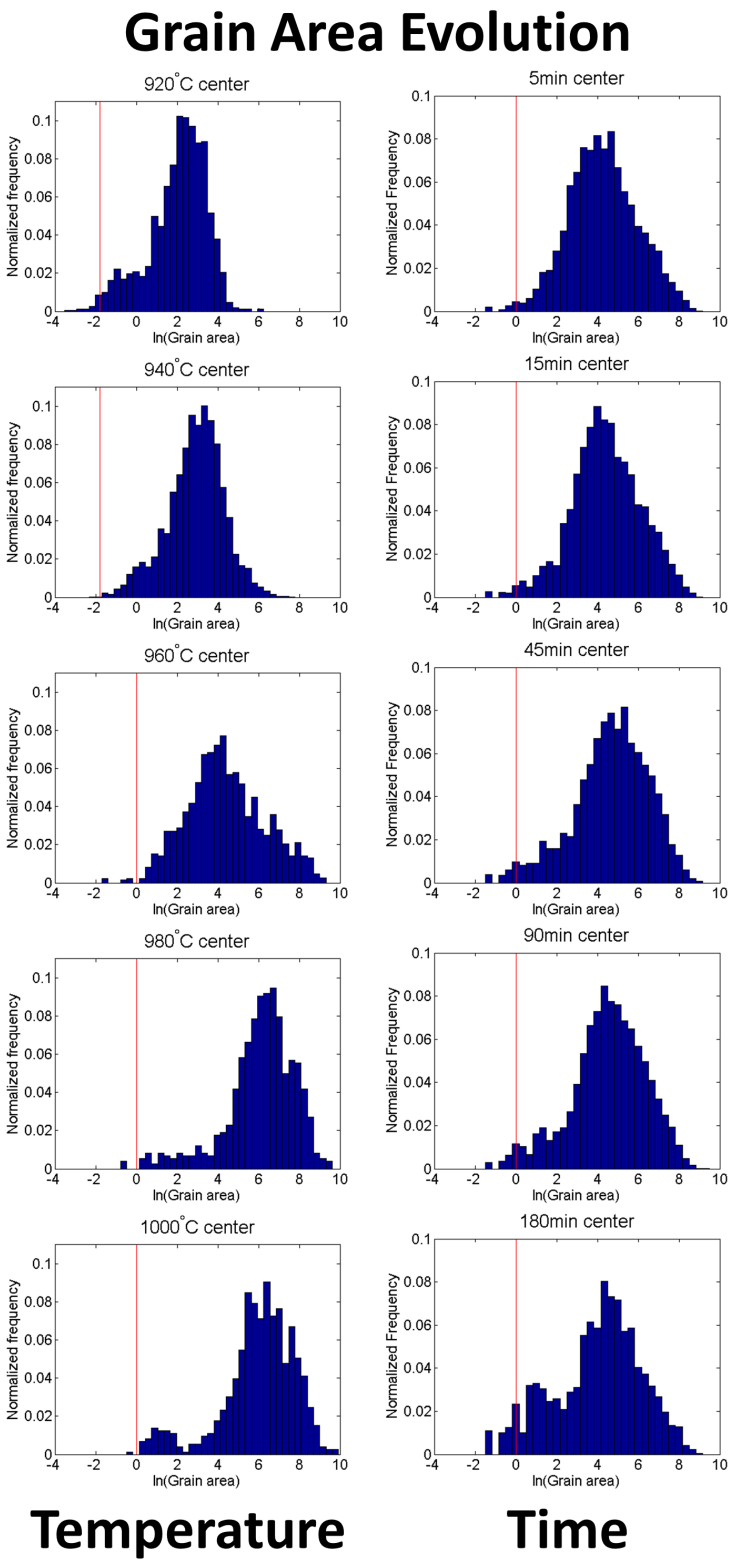

Figure 4.9: Grain area evolution as a function of temperature (left) and time (right). The red vertical line represents the minimum observable grain size, of 2 by 2 pixels, using the microscope.

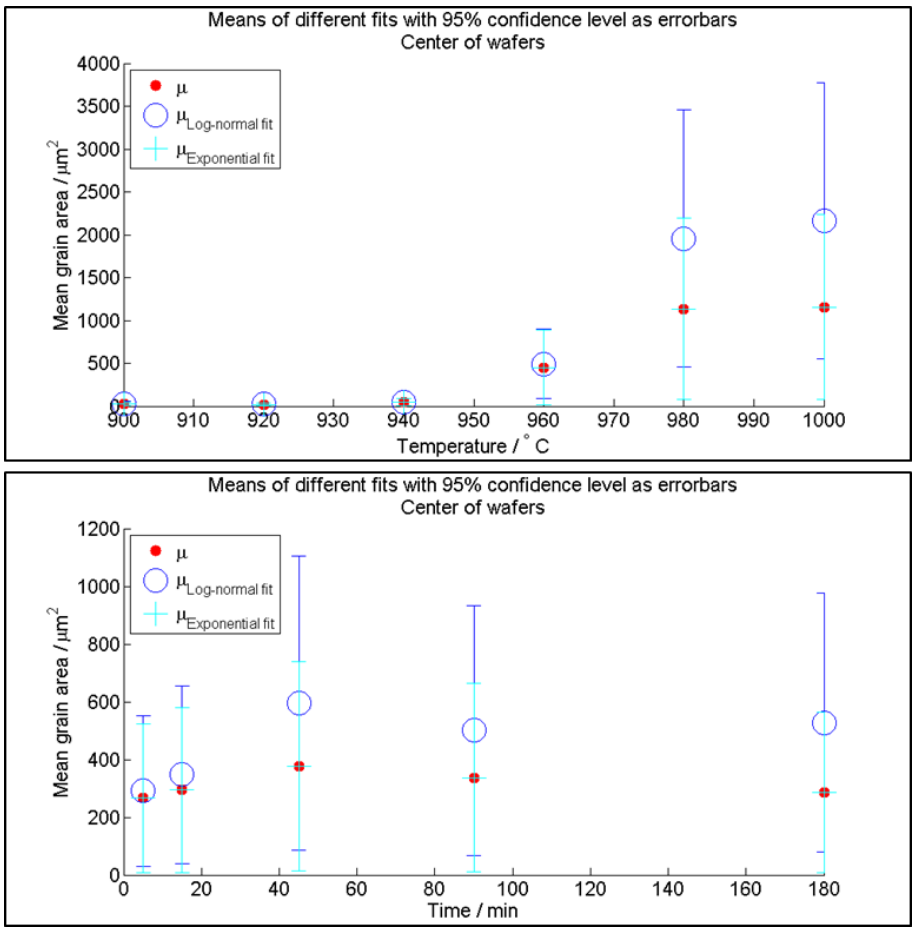

Figure 4.10: The mean grain area for different annealing temperatures (top) and annealing times (bottom). The grain area is fitted with a log-normal fit, and an exponential fit. The error bars represents the 95 % confidence interval for the fit-mean. Reprinted from [81].

4.5 Discussion

In this work I optimized graphene growth on copper thin film on silicon dioxide layers on silicon wafers. The characterization of copper grain growth during the annealing phase of graphene growth recipes.

Utilizing a copper thin film on a wafer, shows a reduction of the amount of contaminants present on the surface during growth of graphene. In chapter 2 it was found that particles on the surface of a copper foil, act as nucleation sites, which reduces the potential size of graphene crystals.

Through a combination of micro-Raman maps and EBSD maps, it was found that the graphene nucleation density depends on the copper crystal orientation, see figure 4.3 and 4.4 for Raman analysis and figure 4.5 and 4.7 for EBSD analysis. Graphene grown on Cu(111) was found to have the lowest growth rate compared to Cu(101) and Cu(100).

The decrease in 2D/G ratio from $\tilde{2}$ to $\tilde{0}.5$ observed in one half of a graphene crystal in figure 4.4, could be from a second layer of graphene forming on that Cu grain. This would explain the large change in the 2D/G ratio and lesser change in the D/G ratio and the FWHM(G). It may be possible that the Cu grains all share the same major orientation e.g. (100). This is highly unlikely, as was shown by EBSD in section 4.3. Very little variation in the defect density of the CVD graphene was seen from the Raman map analysis on different copper crystal orientations. This supports what was observed in a study from 2011, where they state that the graphene defect density does not vary with copper grain orientation for growth above 900 °C [122].

Analyzing the crystal grain in a polycrystalline copper thin film via optical microscopy was carried out. Smaller grains were not analyzed well due to the limitations of the microscope. Larger grains were typically handled without issue. Though large grains become difficult to analyze, when they become larger than the field of view of the microscope. Crystal twin planes are not included in this analysis, because the optical contrast is too small to be recognized by the microscope.

The area fraction of Cu(111) can be changed mainly through the annealing temperature, and to a lesser degree annealing time. This is also known from surface tension driven Ostwald ripening [96]. The log normal fit was found to deviate from the data with increasing grain area. The exponential fit handles the larger grains a lot better, as seen in figure 4.10. The overall evolution of the grain areas follows the general trend of higher temperature resulting in larger grains. The larger mean areas were found to be lower, than the predicted relation given by the Ostwald equation. The ripening process is mostly dependent on the temperature and the surface energy.

Chapter 5

CVD Graphene on Cu films on Sapphire

Growing graphene via CVD on copper thin film on a silicon wafer with a thermal oxide layer of sufficient thickness to avoid copper silicides, showed great promise as a substitute to growing graphene on a copper foil. Deposited copper showed no particles on the surface and a much smoother surface compared to copper foils. Going the next step would be to eliminate the crystal grain boundaries in the copper thin film all together. Earlier studies have shown how the best quality graphene, in terms of defect density, was grown on Cu(111) [97]. So rather than trying to optimize the surface of the copper thin film on silicon dioxide for area fraction of Cu(111), another substrate which promotes Cu(111) was chosen. Annealing of copper thin films on sapphire has been shown to enhance the Cu(111) direction up 95% of the surface area [48] [56]. The quality of the corresponding graphene grown on single crystal Cu(111) thin films on sapphire is very high [97] [48] [47]. In this chapter I will describe graphene growth via CVD on copper thin films deposited on a sapphire wafer.

Hypotheses

1b. *The copper crystal size and orientation depends on the interface between the carrier wafer and a deposited copper thin film, and the annealing temperature.*

2b. *The defect density of CVD graphene is dependent on the growth parameters e.g. temperature and gas flow.*

3b. *The graphene domain size depends on the catalyst domain size.*

4b. *The defect density and growth rate depend on the different crystal orientations of the copper catalyst.*

5.1 EBSD characterization

Copper sputtered on a 1 µm SiO_2/Si wafer yields a polycrystalline film after annealing. Grain sizes ranges from a few microns up to around 1 mm in diameter. Copper sputtered on to a c-plane (0001) sapphire wafer yields an almost single crystalline film of Cu(111) across a 4-inch wafer, this is shown in figure 5.2. This tendency of Cu(111) dominance on c-plane sapphire has been report in [48] [46] [56] [44]. The surface of the annealed copper film was analyzed in an optical microscope as well as SEM and EBSD. The copper film becomes an almost perfect mirror, which is very difficult to analyze in an optical microscope. SEM showed no grain boundaries as seen with copper on SiO_2, except for a few areas as seen in figure 5.1, near the edge of the wafer. In order to examine the crystal direction of the copper film EBSD was used, as seen in figure 5.2. This figure shows that the crystallinity is Cu(111), as already mentioned in literature.

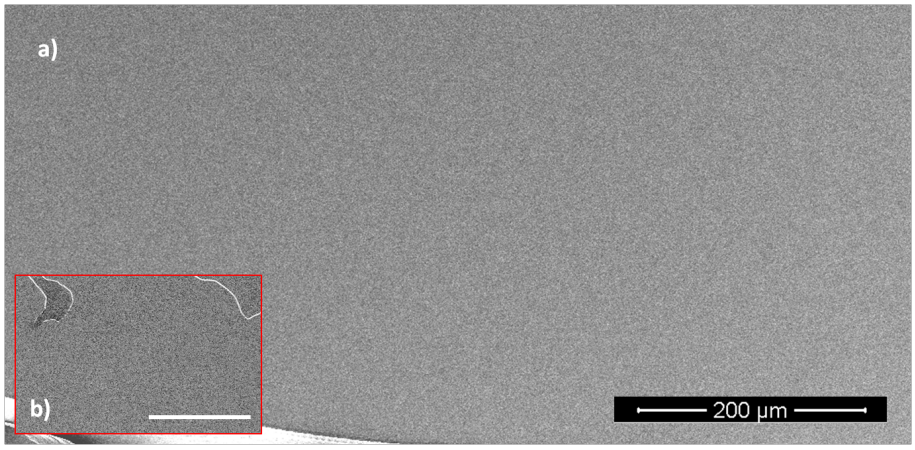

Figure 5.1: SEM image of large area single crystal copper on sapphire. Inset shows a rare grain boundary near the edge of the wafer, scale bar represents 40 µm. The dark spots are graphene crystals from a partial growth recipe in the BM, the bright lines arise from the boundary between two copper grains.

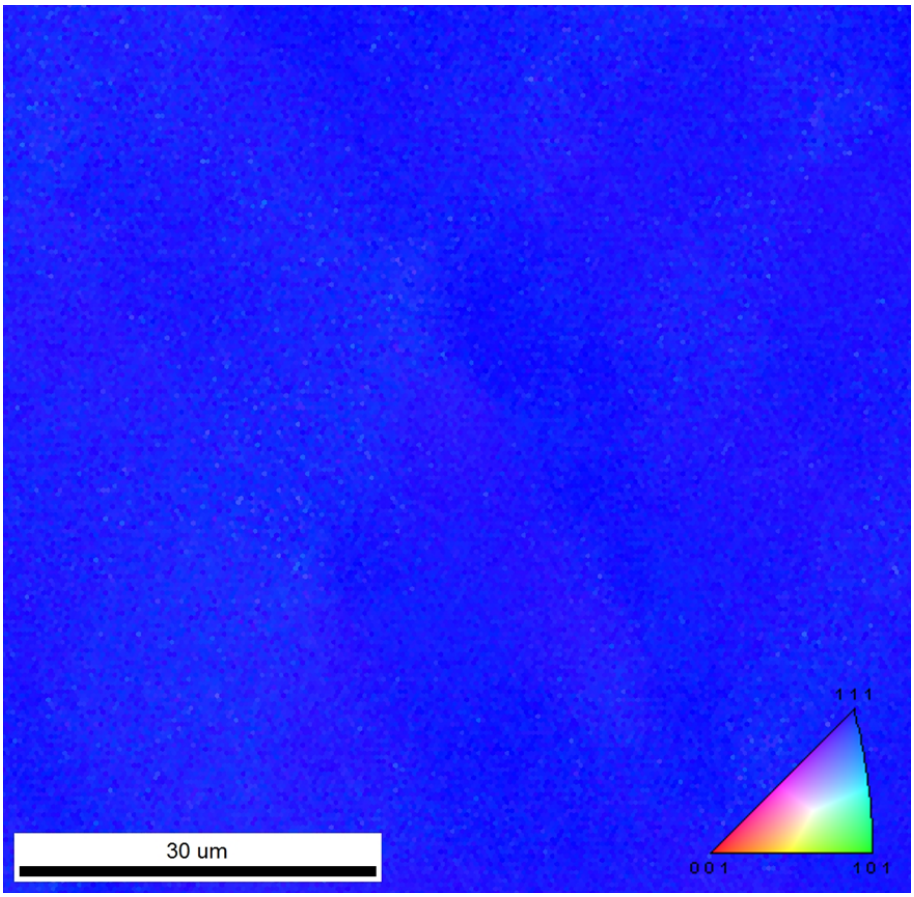

Figure 5.2: Inverse pole figure of sputtered copper on a sapphire (0001) wafer after annealing, showing how the copper surface is (111) oriented in the entire scanned area. This is true for most of the wafer surface except for few areas near the edge of the wafers.

5.2 Design of Experiments

In order to explore graphene growth on copper thin films on sapphire wafers to the fullest, statistical experiment planning: design of experiments (DOE) was utilized. It was assumed that the wafer to wafer variation would be negligible, and that day to day operation of the BM would not vary significantly. It was decided to keep the pressure constant at 20 mbar and the growth time constant at 5 seconds - to yield a partial growth of all of the experiments. These assumptions gave a screening design with five factors. This design was run through a fractional factorial with 16 number of runs plus three center points, giving a resolution of 5 with all 2-factor interactions estimable. The five factors used in this design were, top heater power %, bottom heater power %, argon flow rate, hydrogen flow rate, and finally methane flow rate. The run order was randomized and gave the table of experiments seen in table 5.1, with minimum, maximum and center values. Center points are used to measure the process to process variation, since the same experiment is carried out three times. The values given in parentheses are nucleation density estimates due to either full coverage or nucleation site counting. The estimates are based on an estimation of the graphene grain size, from a visual inspection of the SEM images.

#	Bottom Power %	Top Power %	Ar flow rate sccm	H2 flow rate sccm	CH4 flow rate sccm	Area μm^2	N. D. μm^{-2}
1	30	75	1000	0	5	80.20	0.31
2	30	65	0	1000	45	95.32	(0.1)
3	30	75	0	0	45	99.78	(0.17)
4	30	65	0	0	5	99.99	(0.27)
5	20	65	0	0	45	53.26	0.7
6	**25**	**70**	**500**	**500**	**25**	**84.23**	**0.33**
7	30	75	1000	1000	45	99.94	(0.19)
8	20	65	0	1000	5	0.43	0.16
9	**25**	**70**	**500**	**500**	**25**	**75.87**	**0.23**
10	30	75	0	1000	5	33.48	0.03
11	**25**	**70**	**500**	**500**	**25**	**66.44**	**0.17**
12	20	75	1000	0	45	41.73	(3.63)
13	30	65	1000	1000	5	74.89	0.54
14	20	75	0	1000	45	0.28	0.05
15	20	65	1000	1000	45	0.48	0.12
16	20	75	0	0	5	41.13	0.85
17	20	75	1000	1000	5	6.64	4.26
18	20	65	1000	0	5	3.05	0.17
19	30	65	1000	0	45	56.93	0.11

Table 5.1: Table showing the factors for DOE of partial graphene growth on copper thin film on sapphire wafers. The area column describes the % fractional area of graphene covering the wafers in the analyzed center regions. The nucleation density (N.D.) corresponds to number of nucleation sites per μm^2. Bold face corresponds to center points in the DOE. The values given in parentheses are estimates due to either full coverage or nucleation site counting.

5.2.1 SEM characterization

SEM was chosen as the characterization technique for the grown graphene. SEM was chosen because it is a fast and a simple technique for determining both the graphene nucleation density and the percentage of graphene covering the surface of the copper. Raman spectroscopy was used to validate the presence of graphene and to give an indication of the defect density (D/G), see figures 5.5, 5.5 and 5.7. Both nucleation density and coverage are important factors for growing large high quality graphene crystals, as mentioned in chapter 1 (Introduction).

The nucleation density was measured from the images collected in the center of the wafers at 20k x magnification and the nucleation density was measured as the number of graphene crystals per image. Each image represents an area of 150 μm^2. The graphene coverage is measured as the covered area divided by the total area of the image. ImageJ is used for processing the images and calculating the nucleation density and graphene coverage.

The responses of the experiments from the DOE are shown in figure 5.3, except the center points, shown in figure 5.4. The images in figure 5.3 are collected in the center of the wafers and labeled according to experiment number. A large variation is seen in the coverages, see table 5.1, from full coverage in experiment 4 and 7, to no coverage in 8 and 14. The nucleation density responses, in table 5.1, ranges from 4 to 639. In experiments 2, 3, 4, and 7 no measure of nucleation density could be extract from the images, due to the graphene fully or almost fully covering the surface of the copper. In experiment 12 no nucleation density could be measured due to the quality of the image and the shape of the graphene crystals. An estimate was on the basis of previous observations of CVD graphene.

In figure 5.4, the center points of the DOE design are shown. Very little variation is seen in terms of graphene crystal shapes in the center and halfway points of the three wafers, though the edge of wafer 11 varies quite significantly compared to wafer 6 and 9.

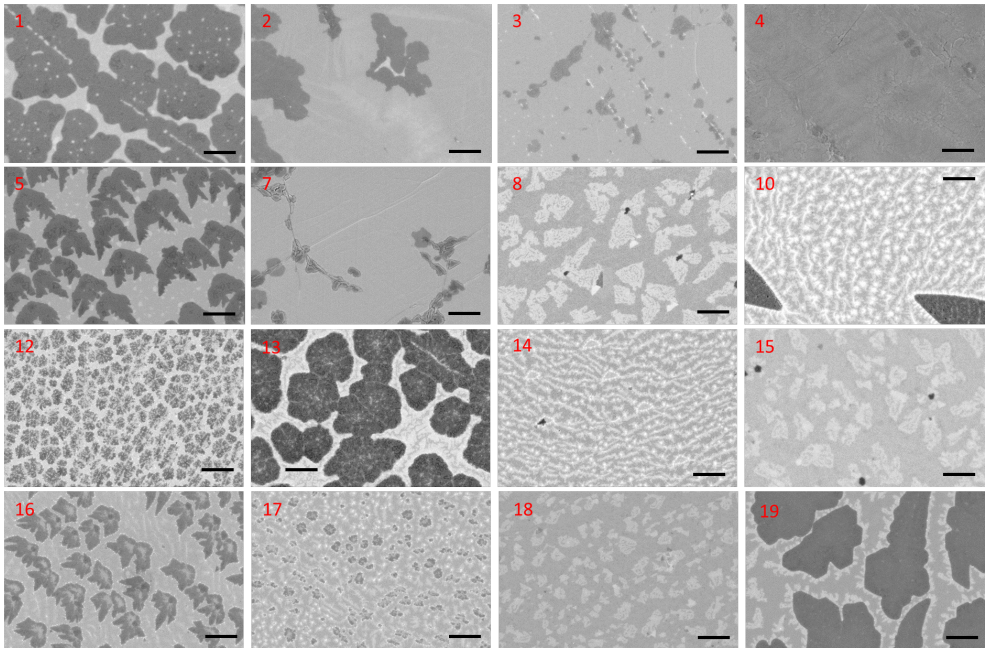

Figure 5.3: Shows SEM images of the center of the wafers of all the experiments carried out in the DOE (excluding the center points). Very different nucleation densities, area, and graphene edge roughness is seen. Scale bar is 1 μm. For full coverage of graphene the nucleation density is difficult to obtain.

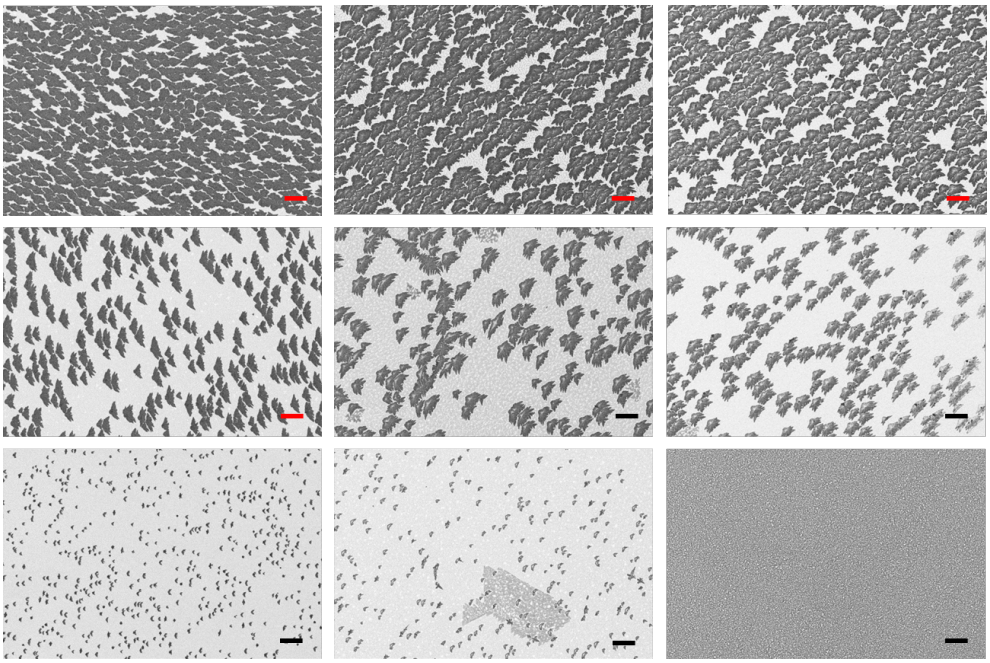

Figure 5.4: SEM micrographs of the graphene grown using the recipe for the three center points. a-c) shows experiment number 6, from center, halfway to the edge and edge of the wafer respectively. d-f) shows experiment number 9, from center, halfway to the edge and edge of the wafer respectively. g-i) shows experiment number 11, from center, halfway to the edge and edge of the wafer respectively. Scale bar represents 2 μm.

Copper mass change

Weighing the wafers before and after growth of graphene gives an estimate of the copper loss during processing, due to dewetting and evaporation. One of the concerns with copper on SiO_2 is that a very thick layer of copper is needed to avoid dewetting and evaporation of the copper layer resulting in a film with pinholes. With a 1.5 µm thin layer of copper on sapphire dewetting is not an issue. By estimating the copper loss during processing it is possible to investigate, whether a reduction in the deposited copper thickness is achievable, as seen from [97]. A reduction in thickness of the copper leads to a decrease in the processing time and a minimization of the material cost. In appendix E the changes in mass of the sapphire wafers with deposited copper is shown. Generally the mass loss is of the order 0.005 % of the total mass (sapphire wafer + 1.5 µm layer of copper). The average mass of a 1.5 µm layer of copper was previously measured at ∼102 mg (∼$9.67 \cdot 10^{20}$ atoms) meaning that the copper mass loss is of the order 1.1% corresponds to a loss of ∼$1.06 \cdot 10^{19}$ Cu atoms through evaporation.

Raman characterization

Single Raman spectra were performed on all of the 19 wafers in the same areas as the SEM micrographs were collected, shown for wafer center in figure 5.5. Center of the wafers, halfway to the edge, and at the edge of the wafers. Judging the spectra by the D/G ratio gives an indication of the nucleation density. Since the graphene was grown to partial coverage for the majority of the experiments, the laser spot was aimed at areas, where graphene was visible in the spectrum.

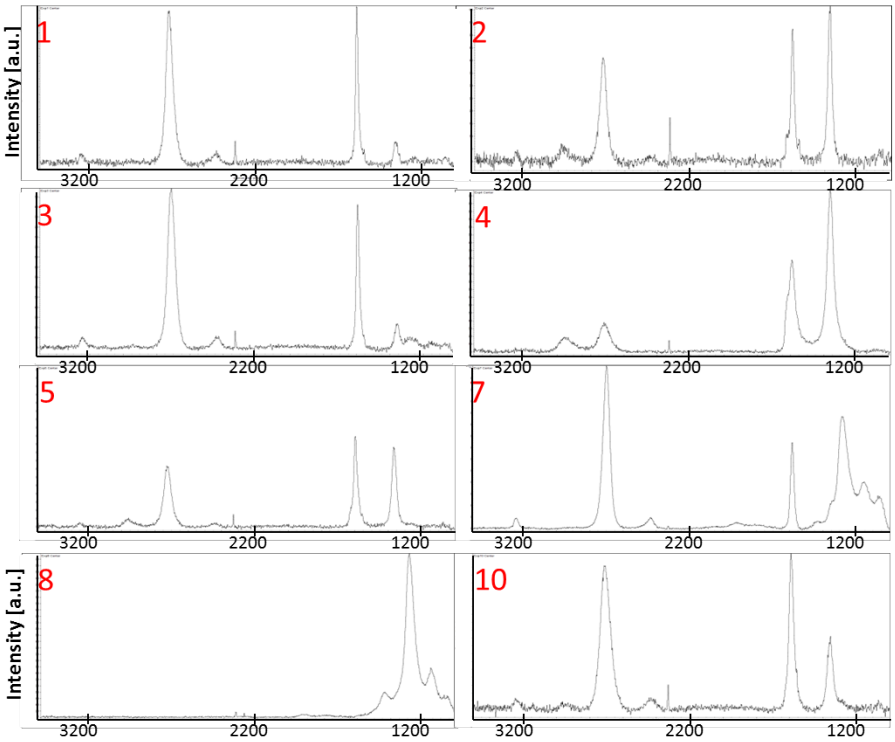

Figure 5.5: Shows Raman spectra of experiments (1-5,7,8,10) carried out in the DOE. Very different D/G ratios, FWHM(G), and 2D/G ratios are seen. A huge variation is seen in the Raman spectra as expected from the SEM images. The graphene seen from SEM in experiment 8 are so small, they are not detected by Raman. In terms of nucleation density experiment 1 and 3 are the best.

A Raman map was collected on a sample grown at conditions resembling experiment 13. The optical image, Raman D/G ratio, 2D/G ratio, and FWHM(G) maps are shown in figure 5.7. The graphene was grown under the following conditions to achieve a partial coverage of graphene: 27% bottom heater power, 70% top heater power, 1000 sccm of Ar and H_2, 5 sccm CH_4, 20 mbar pressure, and 30 second growth time, after a 30 minute annealing in a hydrogen and argon atmosphere. The Raman spectra were collected using a blue 455 nm excitation laser, 3 mW laser power, and three spectra were averaged using 10 second collection time for each. The D/G ratio is generally on the order of 0.1-0.2, with a few outliers reaching a ratio of 1. Since the graphene is only partially covering the copper a high D/G ratio is expected. The FWHM(G) shows little to no narrowing, meaning a low doping level. The 2D/G ratio is very close to 1 throughout the mapped area, meaning predominantly single layer graphene was grown.

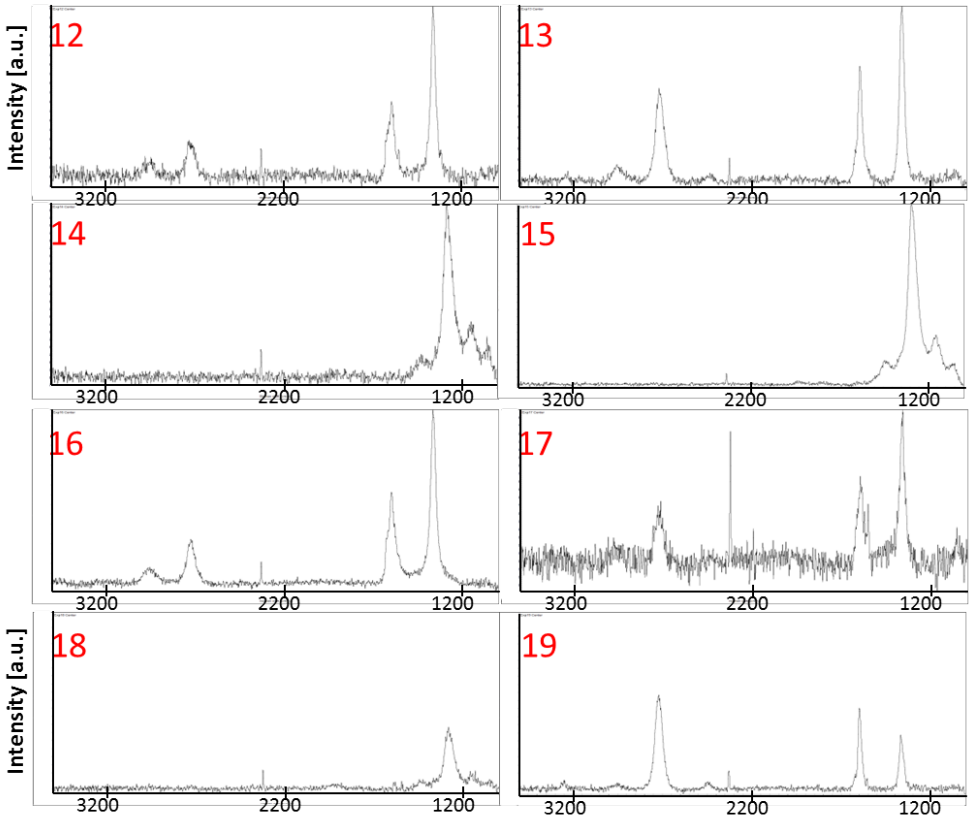

Figure 5.6: Shows Raman spectra of experiments (12-19) carried out in the DOE. Very different D/G ratios, FWHM(G), and 2D/G ratios are seen. Large D peaks are seen in all of the experiments, except for 14, 15, and 18, where no graphene is observed.

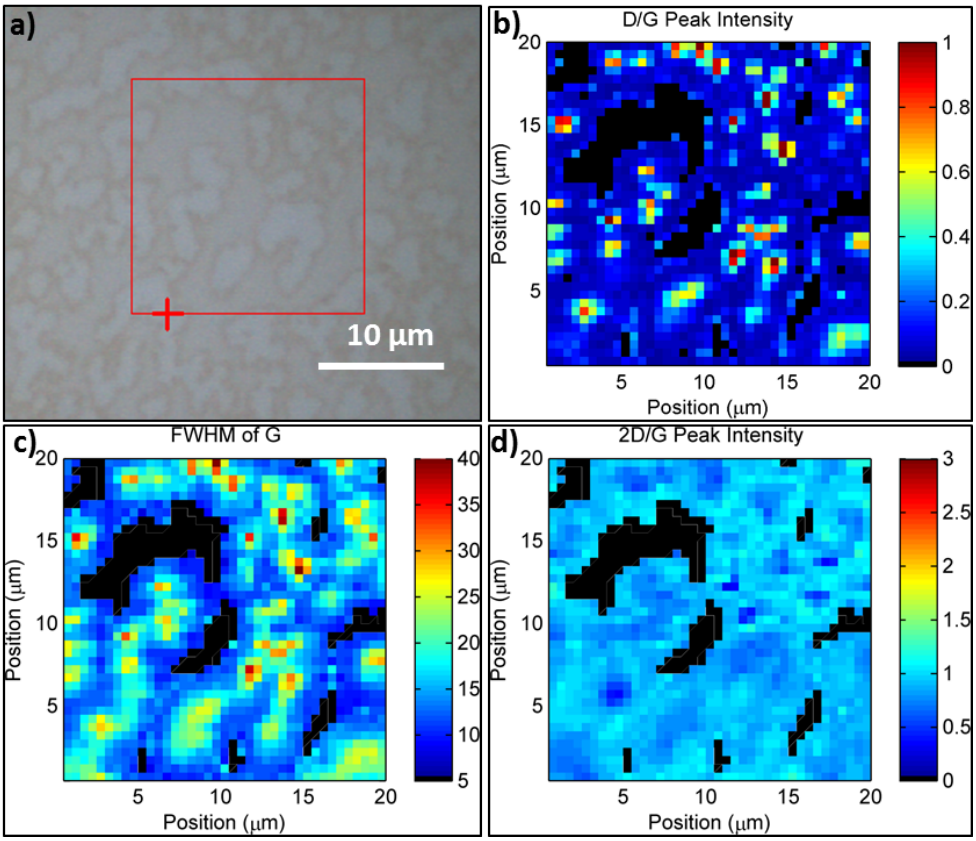

Figure 5.7: CVD graphene from a short growth time to achieve partial coverage. a) Optical image showing the region where the Raman map was collected. b) Raman D/G ratio map. c) Map of the FHWM of the G peak. d) 2D/G peak ratio map. Black corresponds to no signal/no graphene.

5.3 DOE results

Using the SAS JMP 11 software, to model the responses found from the experiments, the predicted coverage and nucleation densities are found in figures 5.8 and 5.9. The R_{sq} value is found to be 0.91 with a p-value of P=0.027 for coverage for a 5 % level of significance. For the nucleation density the R_{sq} = 0.97 with P=0.0002 for a 5 % level of significance. The solid red line corresponds to the mean of the model prediction, while between the dotted red lines are P<0.05. The center points are all outside the 5 % level of significance for the predicted nucleation density and graphene coverage.

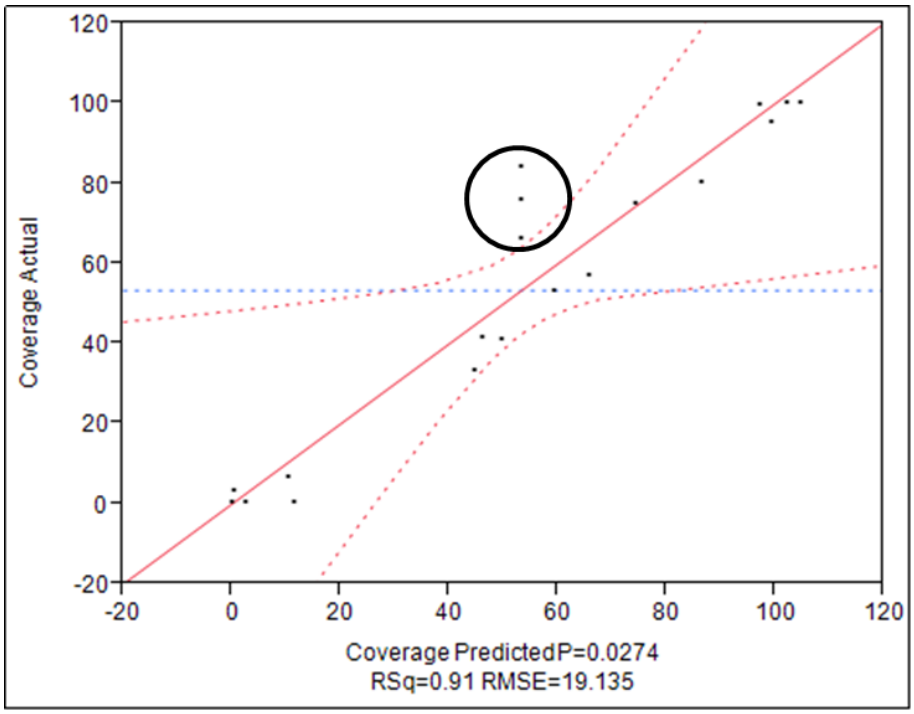

Figure 5.8: DOE coverage response vs model prediction. The three points circled in black are the center points that have a higher response than the model prediction. This could be due to a parabolic effect of the mass flow controllers, since the high and low values, of hydrogen and methane, might be too close to the limit of the controllers.

The nucleation density response is plotted as contours of bottom heater power vs top heater power, Ar flow rate, H_2 flow rate, and CH_4 flow rate,

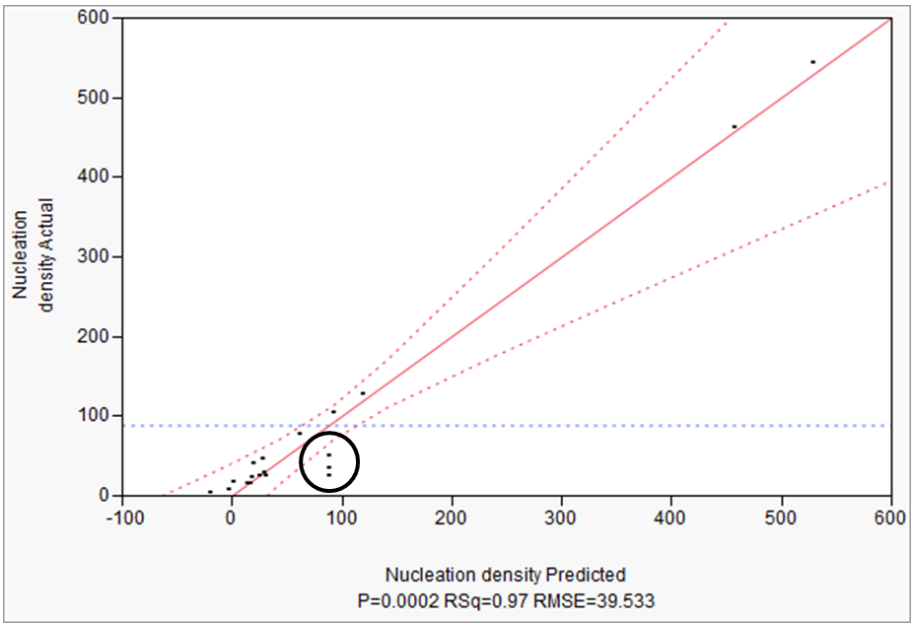

Figure 5.9: DOE nucleation density response vs model prediction. The three points circled in black are the center points that have a lower response than the model prediction. The nucleation density in this plot corresponds to the actual number of nucleation sites in a fixed area, not the density.

in figure 5.10 a, b, c and d respectively. The response is also plottet as hydrogen vs Ar flow rate, top heater power, and CH_4 flow rate, in figure 5.11 a, b, and c respectively. The response as function of Ar flow rate vs CH_4 and top power is plottet in figure 5.11 d and e.

From the contour plots of bottom heater power it is seen that increasing the power will result in a decrease of the nucleation density, regardless of variation in the other four parameters.

The contours of hydrogen flow rate vs argon flow rate, top power, and methane flow rate, shows that a low nucleation density is achieved when hydrogen and methane have a high flow rate, figure 5.11 c. Figure 5.11 d shows that for high methane flow rate the argon flow rate should be low. For a high hydrogen flow rate the argon flow rate and the top power should be low, figure 5.11 a and b. Reducing both the top power and the argon flow rate results in decreased nucleation density as seen in figure 5.11 e. For a low flow rate of methane the corresponding hydrogen flow rate should be low, while for high methane flow rate the hydrogen flow rate should be high, to achieve a low nucleation density.

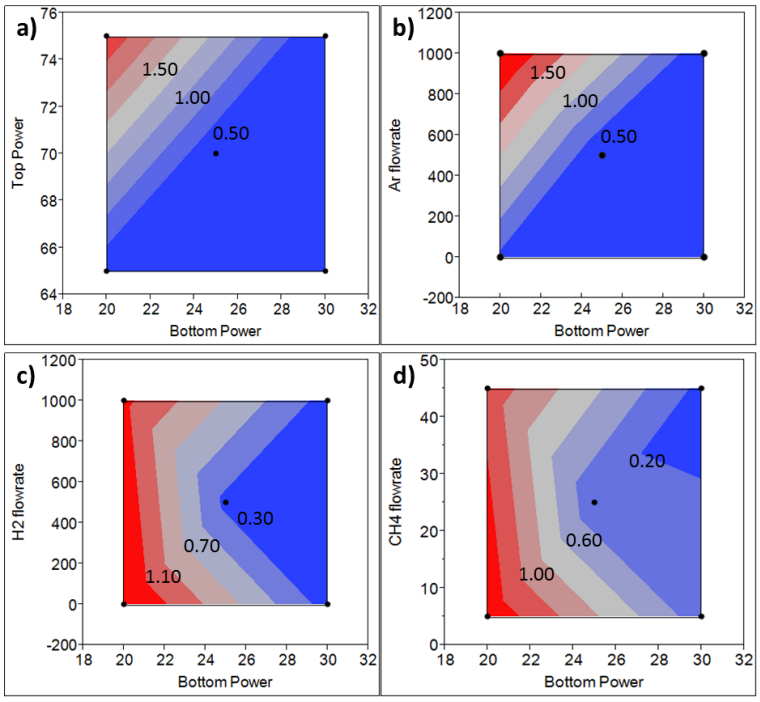

Figure 5.10: Contour plot of the nucleation density for bottom power vs top power, Ar-, H_2-, and CH_4 flow rates.

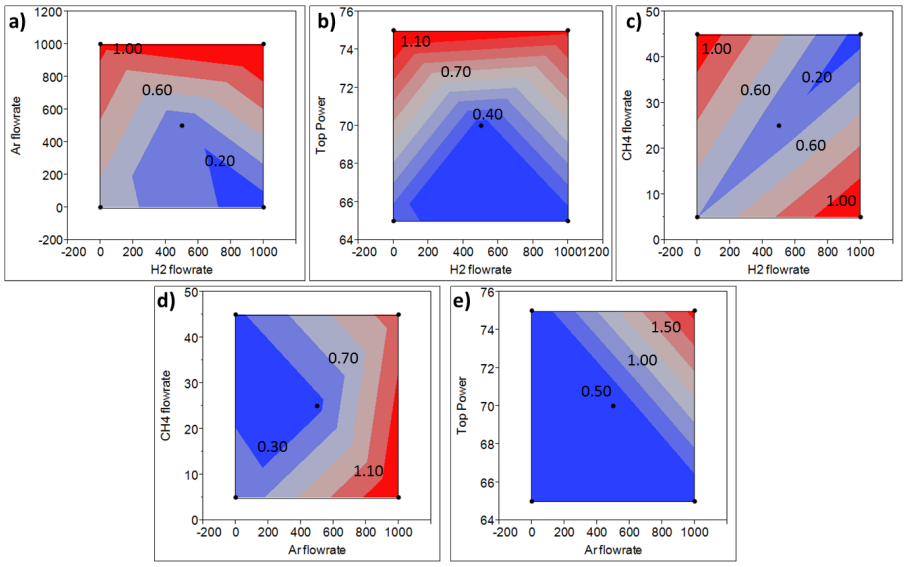

Figure 5.11: Contour plot for the nucleation density for H_2 flow rate vs Ar flow rate, top power, and CH_4 flow rate. Ar flow rate vs CH_4 flow rate and top power.

5.3.1 Summary

In order to achieve a low nucleation density the bottom heater power must be high, and the methane flow rate should be proportional to the hydrogen flow rate. A high coverage is achieved when the temperature is high as well as the partial pressure of methane. A flow of argon should be avoided during CVD growth of graphene. Table 5.2 lists the optimum parameters for low nucleation density. High coverage of graphene is simply achieved by increasing the growth time.

		Minimum Nucleation density
Bottom Power	[%]	30
Top power	[%]	75
Ar flow rate	[sccm]	0
H_2 flow rate	[sccm]	1000
CH_4 flow rate	[sccm]	45

Table 5.2: Minimum values of nucleation density for CVD growth of graphene on Cu/sapphire. The values are based on DOE with a constant background pressure of 20 mbar, and a growth time of 30 seconds.

5.4 Discussion

This work aimed at optimizing a graphene growth recipe in the BM using DOE. The graphene nucleation density and coverage responses were characterized by SEM on the copper surface.

Utilizing DOE to investigate the parameter space, showed that too large ranges in parameters were chosen. Growth patterns obtained varied from very little to no growth up to full coverage (with some second layer growth), as seen in figure 5.3. This meant that the nucleation density, could not be measured with the chosen parameters, for experiments 2, 3, 4, 7 and 12, due to individual graphene grains being indistinguishable. An indication of the optimum parameters for further study into the growth was found.

Annealing of a 1.5 µm thin sputtered copper film on a sapphire (0001) wafer yielded almost 100% Cu(111) on the surface. This was confirmed by EBSD and light microscopy, as well as previously mentioned in literature [48] [46] [56] [44]. This gives a great starting point for developing a graphene recipe with the potential of growing graphene on a cheap 4" diameter single crystal copper wafer. Growing graphene on single crystal copper foil is useless for mass production of graphene, due to the high cost of single crystal foils. The surface is well understood since only one crystal orientation is present (Cu(111)), and almost no grain boundaries are not present across a 4-inch wafer, seen in figure 5.1.

The SEM characterization of the grown graphene responses shows a very large variation in the different experiments. The coverage ranges from no coverage to full coverage, and the nucleation density ranges from 0.03 to 4.26 μm^{-2}. From the experiments, where full coverage is observed a nucleation density could not be estimated. From the DOE center points it was found that the stability and wafer to wafer uniformity was improved compared to PID controlled temperature, seen in chapter 3 (CVD graphene on Cu foils). Some variations in the responses were seen in the center point experiments, which could be explained by variations in the wafers, due to deposition variations, different handling, etc.

Raman characterization was not used as a primary technique in this optimization routine, due to the fact that the graphene quality changes with a transfer. The quality change of the graphene also depend on the transfer method e.g. chemical etching or electrochemical bubbling.

An interesting result of the DOE was that an argon flow during the growth of graphene is detrimental to the quality. this is opposite what was found in a study from 2010, where they found that a high argon flow rate resulted in higher quality graphene compared to a low flow (APCVD) [6].

Measuring the copper mass loss from graphene growth under various conditions i.e. high and low temperatures, and large changes in gas flow rates, showed that about 1 % or $\sim 1 \cdot 10^{19}$ atoms of the copper is lost to evaporation. The wetting of the copper layer on the sapphire is much improved compared to copper on SiO_2, since no pinholes were seen, even for very high temperatures and long processing times. This means that the thickness of the copper can be greatly reduced. Previous work has observed that 400 nm is sufficient for graphene growth and avoiding de-wetting of the copper from the sapphire wafer [97]. Another observation found that a minimum of 500 nm is needed for graphene growth on SiO_2/Si, due to the poor wetting of copper on SiO_2 [67]. I have observed that a thickness of 500 nm Cu on SiO_2 is insufficient to grow grow high quality graphene. A much thicker Cu layer is needed to achieve large grains due to the energetics of the Cu grain evolution found in chapter 4. This is another reason, why growing graphene on Cu on sapphire is a positive step towards reducing the cost of fabrication by reducing the amount of copper needed for graphene growth.

Chapter 6

GFET Measurements

CVD graphene grown on copper foil and on copper film on SiO_2/Si was transferred via electrochemical bubbling and chemical etching. The CVD graphene sample grown on copper film on sapphire was transferred using chemical etching. Following the transfer, the samples were patterned via e-beam lithography, metal deposition, and RIE etching, into a GFET device, described in chapter 1 (Introduction). The corresponding two-point I_{DS} vs V_{gate} measurements are shown in the following sections for the different copper substrates. The measurements have all been carried out for different temperatures, using liquid nitrogen for low temperature measurements and the built in heater for high temperature measurements.

An SEM image of a CVD graphene Hall bar device is shown in figure 6.1. The image shows the active graphene region and where the graphene has been etched away revealing the SiO_2 gate dielectric.

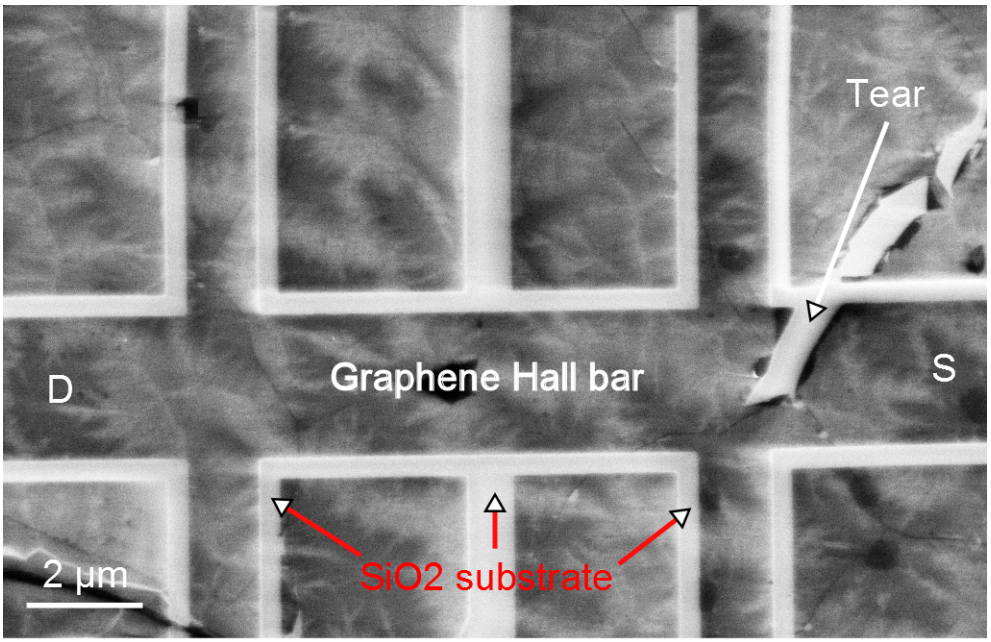

Figure 6.1: SEM image of the graphene Hall bar in a GFET device. The image is recorded before the gold contacts have been added to the graphene Hall bar. The bright lines are SiO_2 indicated by red arrows.

6.1 CVD graphene from Cu foil

Two-point I_{DS} vs V_{gate} measurements are shown in figure 6.2(top for etching transfer and bottom for bubbling transfer). Graphene from etching transfer show a mobility of ∼162 $cm^2/(V{\cdot}s)$, estimated from the slope of the dotted line in figure 6.2 (top) and equation 1.2. The charge neutrality point was estimated to be at ∼28 V. Graphene from electrochemical bubbling transfer show a mobility of ∼970 $cm^2/(V{\cdot}s)$, estimated from the slope of the dotted line in figure 6.2 (bottom) and equation 1.2. The charge neutrality point was estimated to be at ∼25 V.

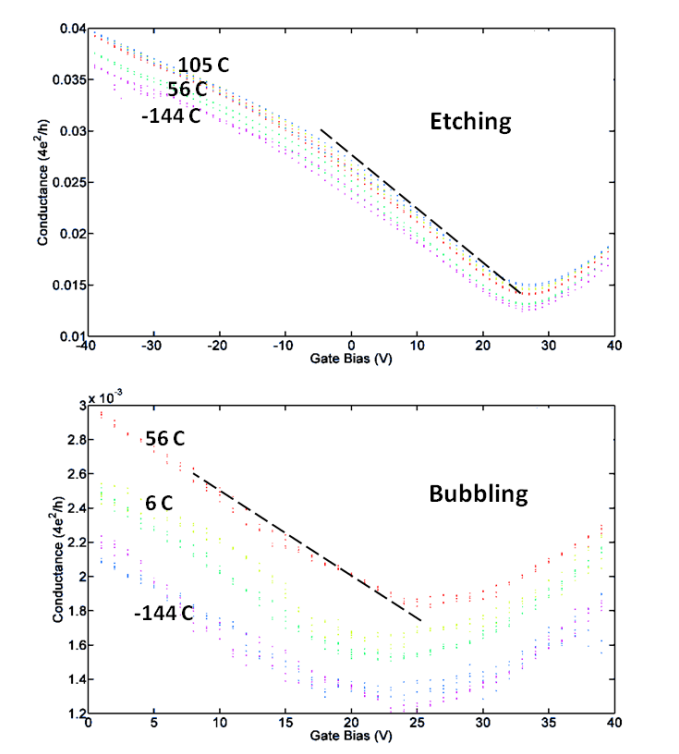

Figure 6.2: Two-terminal conductance [$4e^2/h$] vs V_{gate} measurements for different temperatures. Top: Graphene transferred using chemical etching. Bottom: graphene transferred using electrochemical bubbling. A mobility of ∼162 $cm^2/(V{\cdot}s)$ (etching), and ∼970 $cm^2/(V{\cdot}s)$ (bubbling) was estimated from the slope of the dotted lines.

6.2 CVD graphene from Cu film on SiO_2

The two-terminal and four-terminal (I_{DS} vs V_{gate}) measurements are shown in figure 6.3 for graphene transferred via electrochemical bubbling. Figure 6.4 shows two-terminal measurements for graphene transferred via Cu etching. A four-terminal mobility of ~2500 $cm^2/(V{\cdot}s)$ was estimated from the slope of the dotted line in figure 6.3 (bottom) and equation 1.2. A two-terminal mobility of ~585 $cm^2/(V{\cdot}s)$ was estimated from the slope of the dotted line in figure 6.3 (top). The sample in figure 6.4 has an estimated mobility of ~890 $cm^2/(V{\cdot}s)$. The charge neutrality point lies at ~27 V for the sample in figure 6.3 and ~38 V for the sample in figure 6.4.

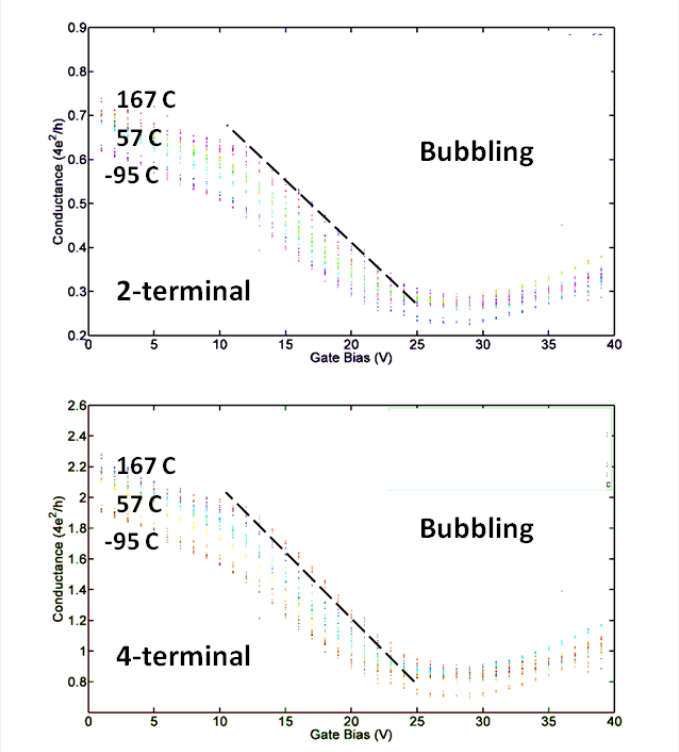

Figure 6.3: TOP: Two-terminal conductance [$4e^2/h$] vs V_{gate} measurements for different temperatures. Bottom: Four-terminal measurements for different temperatures. The graphene was transferred using electrochemical bubbling. The four-terminal carrier mobility is ~2500 $cm^2/(V{\cdot}s)$ and the two-terminal carrier mobility is ~585 $cm^2/(V{\cdot}s)$, estimated from the slope of the dotted lines.

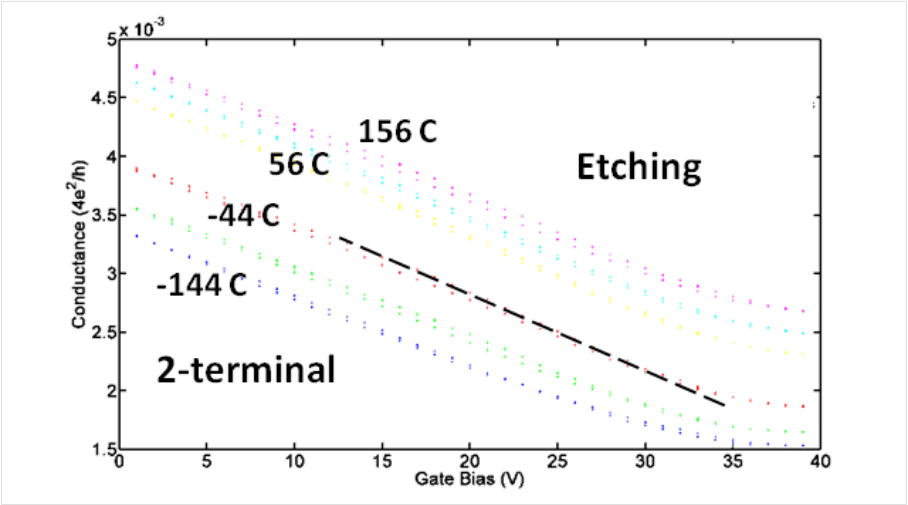

Figure 6.4: Two-terminal conductance $[4e^2/h]$ vs V_{gate} measurements for different temperatures. The graphene was transferred using chemical etching of the Cu. A mobility of $\sim 890\ cm^2/(V{\cdot}s)$ was estimated from the slope of the dotted line.

6.3 CVD graphene from Cu film on sapphire

Two-terminal measurements resulted in an estimated mobility of ∼1395 $cm^2/(V{\cdot}s)$, from the slope of the dotted line in figure 6.5 and equation 1.2. The charge neutrality point was estimated to be at 26 V for the sample in figure 6.5.

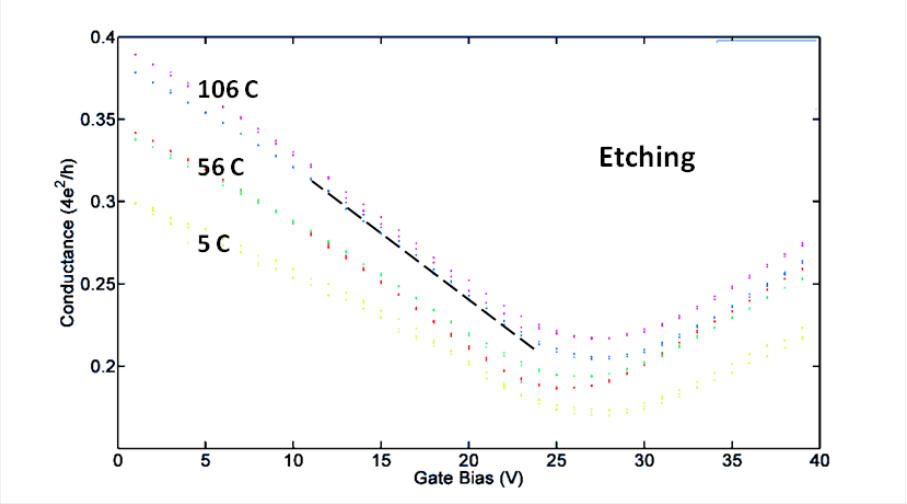

Figure 6.5: Two-terminal conductance $[4e^2/h]$ vs V_{gate} measurements for different temperatures. The graphene was transferred using chemical etching of the Cu. A mobility of ∼1195 $cm^2/(V{\cdot}s)$ was estimated from the slope of the dotted line.

6.4 Discussion

GFET devices were fabricated and characterized. A carrier mobility of ∼162 $cm^2/(V{\cdot}s)$ was found from the two-terminal measurements, of graphene grown on copper foil and transferred using chemical etching of the copper. One possible explanation, why the carrier mobility was so low could be due to line defects, as found in [107]. another reason could be that the chemical etching of the copper induced a lot of defects in the graphene or left Cu residues on the graphene creating scattering centers. The carrier mobility of the graphene transferred using electrochemical bubbling was ∼970 $cm^2/(V{\cdot}s)$, which is much larger than for the etching transfer.

The carrier mobilities of graphene grown on copper on Si_2 and transferred using electrochemical bubbling, was found from the two- and four-terminal measurements to be ∼585 $cm^2/(V{\cdot}s)$ to ∼2500 $cm^2/(V{\cdot}s)$ respectively. This could be due to a difference in contact resistance since the Schottky barrier is negligible for the four-terminal measurement. The mobility of the graphene transferred using chemical etching was found to be ∼890 $cm^2/(V{\cdot}s)$. This is reverse of what was observed for the graphene grown on copper foil. The difference could be due to the fact that the copper film is much cleaner and smoother than the copper foil leaving less particles after transfer.

The two-terminal carrier mobility of graphene grown on copper film on sapphire, transferred using chemical etching, was found to be ∼1395 $cm^2/(V{\cdot}s)$ and the highest two-terminal carrier mobility of all of the samples measured. If the difference in contact resistance observed between the two- and four-terminal measurements in this chapter is any indication, the expected four-terminal measurements of the two-terminal measurements would be about four times higher.

A huge variation is seen in the carrier mobilities of the CVD GFET devices. Five Hall bar devices out of 100 planned, were measurable. A yield of 5 % just shows how difficult it is to fabricate CVD GFET devices. The transfer methods are not very reliable and possibly damage the graphene in the process. After the graphene transfer the lithographic processing has potential for damaging the graphene even further through e.g. doping from the polymers, electron beam damage during e-beam lithography, intense heating during metal deposition and physical damage from the RIE etc. All of these lithography steps requires that some kind of material i.e. resist or metal is deposited on top of the graphene and these have to be removed, potentially removing some part of the graphene in the process.

Chapter 7

Conclusion

Optimization of recipes for LPCVD growth of graphene on copper foil, copper thin film on SiO_2/Si wafers, and copper thin films on sapphire wafers was carried out. CVD growth of graphene on commercially available copper foil showed that the aluminium oxide particles present on the surface act as nucleation sites for graphene growth. The dominating influence of the particles made general observations of the growth parameters inconclusive. The number of particles on the surface also reduces the potential size of each graphene flake grown. It was not possible to assess the influence of the range of gas flows explored, due to the influence of the particles in determining the number density of nucleation sites. I also determined that it is not possible to perform Raman characterization on graphene grown on copper foils using either a 633 nm or a 532 nm excitation source, due to the large fluorescence background and low signal to noise ratio introducing severe errors in the peak fitting algorithm.

Growing graphene on copper foil showed that the nucleation density was very much dependent on the amount of aluminium oxide particles on the surface of the foil. Replacing the copper foil with a copper thin film deposited on a SiO_2/Si wafer produced a catalyst layer which was free of aluminium oxide particles. An increase in the size of the graphene flakes was achieved on copper film compared to copper foil, thanks to enhanced control over the number density of nucleation sites. Since copper thin films on SiO_2 produces a polycrystalline layer with many grain boundaries it is apparent that these boundary sites would lead more nucleation sites than a single crystalline copper film would, as in the case of copper on sapphire.

From Raman spectroscopy mapping and electron backscatter diffraction analysis it was found that the nucleation density depends on the copper crystal orientation, with Cu(111) producing the fewest nucleation sites. The growth rate of the graphene flakes was also found to be the lowest for Cu(111). Though in this study a clear conclusion concerning the defect density dependence on the copper crystal orientation was not found. It could be argued that with a lower nucleation density on Cu(111), compared with the other main orientations, fewer grain boundaries would be present leading to fewer line defects. defects.

The grain sizes in polycrystalline copper thin films on SiO_2 was found to be highly dependent on the annealing temperature over the range 900 to 1000 °C. Varying the annealing time between 5 and 180 minutes did not show an appreciable effect on the grain size, as assessed by optical microscopic inspection of the copper surface, assisted by digital image processing techniques including thresholding and Voronoi subdivision of the surface. Higher temperatures lead to larger mean grain sizes, and a resulting bimodal distribution in the grain sizes. It was observed that the larger the copper grains the greater the probability of them being Cu(111) orientation. By changing the carrier wafer from SiO_2 to c-plane sapphire it was possible to increase the copper grain size significantly. The copper thin film on sapphire showed almost exclusively Cu(111) behaviour across an entire 4 inch wafer after graphene growth. These observations confirm the first hypothesis that, the copper grain sizes and orientations depends on the surface energy between the carrier wafer and the deposited copper thin film and the annealing temperature.

Design of experiment (DOE) analysis was used to optimize a process recipe, for growing high quality graphene on copper thin film on sapphire wafers. The DOE aimed at minimizing the graphene nucleation density and maximizing the coverage. The ranges chosen for the gas flow rates of argon, hydrogen and methane proved to be too great resulting in either no growth or complete growth of graphene, making measurements of graphene coverage and nucleation density impossible for these extreme cases. Estimations based on previous observations were added to the model. This resulted in an incomplete set of data for the DOE experiments, which resulted in an incomplete model. A complete and detailed model can easily be achieved with the addition of more experiments, in the relevant range.

From the DOE experiments it was found that different growth conditions did lead to strong variations in the size and shape of the grown graphene

crystals. Since the surface of the Cu catalyst layers on sapphire (0001) wafers were highly uniform, almost completely Cu(111) in orientation and very low degree of roughness, it is argued that only the chamber conditions during the growth of graphene influence the shape and size of the graphene crystals. Previous studies also support these observations that the shape of graphene crystals can be manipulated at will by changing the gas composition at APCVD conditions [79].

It was possible to show that the nucleation density decreased at high temperature through these DOE experiments, and additionally the methane flow rate should be comparable to the hydrogen flow rate. A decrease in the nucleation density was also observed for low partial pressures of argon during growth of graphene. A high coverage was achieved when the temperature was high and a high partial pressure of methane was present. These observations indicate that the defect density of cvd graphene is dependent on the growth parameters e.g. temperature and gas flow.

Graphene field effect transistor (GFET) devices were fabricated from CVD grown graphene on copper foil and copper thin film on wafers (SiO_2/Si and c-plane sapphire). The CVD graphene was patterned to a Hall bar geometry using e-beam lithography and RIE etching. Metal contacts were added through a lift-off process. Graphene transferred using chemical etching showed two-terminal room temperature mobilities of 1395 $cm^2/(V{\cdot}s)$ for graphene grown on copper on sapphire, 585 $cm^2/(V{\cdot}s)$ for graphene grown on copper on SiO_2/Si, and 162 $cm^2/(V{\cdot}s)$ for graphene grown on copper foil. The device made from graphene grown on copper on SiO_2/Si showed a four-terminal mobility of 2500 $cm^2/(V{\cdot}s)$. The large difference in mobilities measured on the different samples could be due to line defects across the graphene Hall bar device [107]. These measurements do show that, CVD growth of graphene is a viable way of fabricating GFET devices with a high carrier mobility. While the measured mobilities of CVD graphene do not approach those for exfoliated graphene, the room temperature two-terminal electron mobility found from graphene grown on Cu on sapphire showed great promise. Improving the growth conditions, the lithographic patterning processes, and especially the transfer process could change the fact.

Chapter 8

Outlook

CVD fabrication of graphene is already used in industry for large area transparent electrodes. The price of fabrication is still high and the quality of a transparent graphene electrode has not reached its potential yet. By continued research into the optimization of CVD grown graphene the cost of fabrication will decrease and the quality of the film increase.

Further investigation of CVD growth of graphene on metal thin films deposited on wafers is needed for better understanding of the growth kinetics. Specifically graphene growth where a lower flow rate of methane can be used and a higher degree of control over the temperature. The following transfer process, and device fabrication e.g. GFETs or transparent electrodes also needs further investigation. A transfer process where a higher degree of coverage can be obtained as well as improving the time of transfer, which can be more than 12 hours for etching of thin copper layers.

Further optimizations of graphene growth on copper foils have two paths to follow. One is to perform extensive chemical, electro-chemical or mechanical polishing of the foils before using them for CVD graphene growth. The other route would be to fabricate the copper foils in a way, where this harsh mechanical polishing is not necessary. This could be achieved by deposition of a thin high purity copper layer on a silicon wafer followed by electroplating a thicker copper layer as carrier. The wafer can then be removed from the copper foil and the foil side facing the silicon wafer used for CVD growth of graphene. Early prototype substrates has been fabricated by Andrei Andreiuvski and graphene growth performed by Filippo Pizzochero with excellent results obtained.

One scientific research area, where graphene can contribute is micro- and nano-fluidic systems. The number of applications, that can be simplified and reduced in size and cost, such as lab-on-a-chip devices, where a liquid sample is injected and analyzed. Micro-fluidic devices are also of interest for cell culture on-chip, and for this purpose cell biologists are using ITO as an electrode for heating the sample to the culture temperature, but ITO has the downside that it fluoresces at wavelengths which are commonly used for detection of biomarkers. By replacing the ITO electrode with graphene, which does not fluoresce at those wavelengths, it would be possible to achieve more accurate measurements.

Another interesting micro-fluidic application would be to use graphene as an acoustophoretic transducer for particle separation or trapping. By applying an alternating potential across a graphene electrode in a micro-fluidic device, it would be possible to create a standing wave between the sidewalls of the channel, creating a nodal point/line in the channel. Particles of a certain size would travel to the nodal point/line and larger or smaller particles will move away from it. Increasing the average domain size of CVD grown graphene by tuning the catalytic material is also going to be part of future works.

Bibliography

[1] A. Atkinson, A. Donev, R. T. (2007). *Optimum Experimental Designs, With SAS* (Oxford Sta ed.). Oxford University Press.

[2] Aixtron (2011). Black Magic 4-inch system manual.

[3] An, J., E. Voelkl, J. W. Suk, X. Li, C. W. Magnuson, L. Fu, P. Tiemeijer, M. Bischoff, B. Freitag, E. Popova, and R. S. Ruoff (2011, April). Domain (grain) boundaries and evidence of "twinlike" structures in chemically vapor deposited grown graphene. *ACS nano 5*(4), 2433–9.

[4] Bae, S., H. Kim, Y. Lee, X. Xu, J.-S. Park, Y. Zheng, J. Balakrishnan, T. Lei, H. R. Kim, Y. I. Song, Y.-J. Kim, K. S. Kim, B. Ozyilmaz, J.-H. Ahn, B. H. Hong, and S. Iijima (2010, August). Roll-to-roll production of 30-inch graphene films for transparent electrodes. *Nature nanotechnology 5*(8), 574–8.

[5] Banhart, F., J. Kotakoski, and A. V. Krasheninnikov (2011, January). Structural defects in graphene. *ACS nano 5*(1), 26–41.

[6] Bhaviripudi, S., X. Jia, M. S. Dresselhaus, and J. Kong (2010, October). Role of kinetic factors in chemical vapor deposition synthesis of uniform large area graphene using copper catalyst. *Nano letters 10*(10), 4128–33.

[7] Biró, L. P. and P. Lambin (2013, March). Grain boundaries in graphene grown by chemical vapor deposition. *New Journal of Physics 15*(3), 035024.

[8] Blake, P., E. W. Hill, a. H. Castro Neto, K. S. Novoselov, D. Jiang, R. Yang, T. J. Booth, and a. K. Geim (2007). Making graphene visible. *Applied Physics Letters 91*(6), 063124.

[9] Calizo, I., D. Teweldebrhan, W. Bao, F. Miao, C. N. Lau, and a. a. Balandin (2008, March). Spectroscopic raman nanometrology of graphene and graphene multilayers on arbitrary substrates. *Journal of Physics: Conference Series 109*, 012008.

[10] Cançado, L. G., a. Jorio, E. H. M. Ferreira, F. Stavale, C. a. Achete, R. B. Capaz, M. V. O. Moutinho, a. Lombardo, T. S. Kulmala, and a. C. Ferrari (2011, August). Quantifying defects in graphene via Raman spectroscopy at different excitation energies. *Nano letters 11*(8), 3190–6.

[11] Casiraghi, C. (2012). *Spectroscopic Properties of Inorganic Organometallic Compounds*. RCS Publishing.

[12] Celebi, K. (2013). *CHEMICAL VAPOR DEPOSITION OF GRAPHENE ON COPPER*. Ph. D. thesis.

[13] Chen, H., W. Zhu, and Z. Zhang (2010, May). Contrasting Behavior of Carbon Nucleation in the Initial Stages of Graphene Epitaxial Growth on Stepped Metal Surfaces. *Physical Review Letters 104*(18), 186101.

[14] Chen, S., W. Cai, R. D. Piner, J. W. Suk, Y. Wu, Y. Ren, J. Kang, and R. S. Ruoff (2011, September). Synthesis and characterization of large-area graphene and graphite films on commercial Cu-Ni alloy foils. *Nano letters 11*(9), 3519–25.

[15] Chen, Z., Y.-M. Lin, M. J. Rooks, and P. Avouris (2007, December). Graphene nano-ribbon electronics. *Physica E: Low-dimensional Systems and Nanostructures 40*(2), 228–232.

[16] Cheng, R., J. Bai, L. Liao, H. Zhou, Y. Chen, L. Liu, Y.-C. Lin, S. Jiang, Y. Huang, and X. Duan (2012, July). High-frequency self-aligned graphene transistors with transferred gate stacks. *Proceedings of the National Academy of Sciences*, 1–5.

[17] Chung, T. F., T. Shen, H. Cao, L. a. Jauregui, W. Wu, Q. Yu, D. Newell, and Y. P. Chen (2013, April). Synthetic Graphene Grown By Chemical Vapor Deposition on Copper Foils. *International Journal of Modern Physics B 27*(10), 1341002.

[18] Chung, T F; Shen, T; Cao, H; Jauregui, L A; Wu, W; Yu, Q; Newell, D; Chen, Y. (2013). SYNTHETIC GRAPHENE GROWN BY CHEMICAL VAPOR DEPOSITION ON COPPER FOILS.

[19] Civile, I., M. Diceam, and U. Mediterranea (2013). High-Temperature Growth of Graphene Films on Copper Foils by Ethanol Chemical Vapor Deposition.

[20] Corporation, D. C. (2002). THERMOCOUPLE PROPERTIES AND CONSIDERATIONS WHEN BEING USED IN VERY HIGH TEMPERATURE CLAUS REACTORS, GASSIFIERS AND POX UNITS.

[21] Costa, Sara D; Righi, Ariete; Fantini, Christiano; Hao, Yufeng; Magnusson, Carl; Colombo, Luigi; Ruoff, Rodney S; Pimenta, M. A. (2012). Resonant Raman spectroscopy of graphene grown on copper substrates. *Solid State Communications 152*, 1317–1320.

[22] Cote, L. J., F. Kim, and J. Huang (2009, January). Langmuir-Blodgett assembly of graphite oxide single layers. *Journal of the American Chemical Society 131*(3), 1043–9.

[23] Das, A., B. Chakraborty, and A. K. Sood (2007). Raman spectroscopy of graphene on different substrates and influence of defects. *Bulletin of Materials Science 31*(3), 6.

[24] Das, Anindya; Chakraborty, Biswanath; Sood, A. K. (2008). Raman spectroscopy of graphene on different substrates and influence of defects. *Bulletin of Materials Science 31*(3), 579–584.

[25] Dean, C. R., a. F. Young, I. Meric, C. Lee, L. Wang, S. Sorgenfrei, K. Watanabe, T. Taniguchi, P. Kim, K. L. Shepard, and J. Hone (2010, October). Boron nitride substrates for high-quality graphene electronics. *Nature nanotechnology 5*(10), 722–6.

[26] Ding, F., H. Ji, Y. Chen, A. Herklotz, K. Dörr, Y. Mei, A. Rastelli, and O. G. Schmidt (2010, September). Stretchable graphene: a close look at fundamental parameters through biaxial straining. *Nano letters 10*(9), 3453–8.

[27] Eckmann, A., A. Felten, A. Mishchenko, L. Britnell, R. Krupke, K. S. Novoselov, and C. Casiraghi (2012, August). Probing the nature of defects in graphene by Raman spectroscopy. *Nano letters 12*(8), 3925–30.

[28] Eigler, S. (2014, August). Mechanistic insights into the reduction of graphene oxide addressing its surfaces. *Physical chemistry chemical physics : PCCP 16*, 19832–19835.

[29] Ferrari, a. and J. Robertson (2000, May). Interpretation of Raman spectra of disordered and amorphous carbon. *Physical Review B 61*(20), 14095–14107.

[30] Ferrari, a. and J. Robertson (2001, July). Resonant Raman spectroscopy of disordered, amorphous, and diamondlike carbon. *Physical Review B 64*(7), 075414.

[31] Ferrari, A. C. (2007, July). Raman spectroscopy of graphene and graphite: Disorder, electron-phonon coupling, doping and nonadiabatic effects. *Solid State Communications 143*(1-2), 47–57.

[32] Ferrari, A. C. and D. M. Basko (2013, April). Raman spectroscopy as a versatile tool for studying the properties of graphene. *Nature nanotechnology 8*(4), 235–46.

[33] Ferrari, a. C., J. C. Meyer, V. Scardaci, C. Casiraghi, M. Lazzeri, F. Mauri, S. Piscanec, D. Jiang, K. S. Novoselov, S. Roth, and a. K. Geim (2006, October). Raman Spectrum of Graphene and Graphene Layers. *Physical Review Letters 97*(18), 187401.

[34] Ferrari, A. C. and J. Robertson (2004, November). Raman spectroscopy of amorphous, nanostructured, diamond-like carbon, and nanodiamond. *Philosophical transactions. Series A, Mathematical, physical, and engineering sciences 362*(1824), 2477–512.

[35] Fu, C., G. Zhao, H. Zhang, and S. Li (2013). Evaluation and Characterization of Reduced Graphene Oxide Nanosheets as Anode Materials for Lithium-Ion Batteries. *8*, 6269–6280.

[36] Galib, A. (2012). *Graphene grown by chemical vapor deposition on evaporated copper thin films*. Ph. D. thesis.

[37] Gao, L., W. Ren, H. Xu, L. Jin, Z. Wang, T. Ma, L.-P. Ma, Z. Zhang, Q. Fu, L.-M. Peng, X. Bao, and H.-M. Cheng (2012, January). Repeated growth and bubbling transfer of graphene with millimetre-size single-crystal grains using platinum. *Nature communications 3*, 699.

[38] Geim, a. K. and K. S. Novoselov (2007, March). The rise of graphene. *Nature materials 6*(3), 183–91.

[39] Goh, T. N. (2010). A pragmatic approach to experimental design in industry. (September 2014), 37–41.

[40] Graf, D., F. Molitor, K. Ensslin, C. Stampfer, a. Jungen, C. Hierold, and L. Wirtz (2007, March). Spatially resolved Raman spectroscopy of single- and few-layer graphene. *Nano letters 7*(2), 238–42.

[41] Gupta, a., G. Chen, P. Joshi, S. Tadigadapa, and P. C. Eklund (2006, December). Raman scattering from high-frequency phonons in supported n-graphene layer films. *Nano letters 6*(12), 2667–73.

[42] Han, M., B. Özyilmaz, Y. Zhang, and P. Kim (2007, May). Energy Band-Gap Engineering of Graphene Nanoribbons. *Physical Review Letters 98*(20), 206805.

[43] Hibino, H., S. Tanabe, S. Mizuno, and H. Kageshima (2012, April). Growth and electronic transport properties of epitaxial graphene on SiC. *Journal of Physics D: Applied Physics 45*(15), 154008.

[44] Howsare, C. a., X. Weng, V. Bojan, D. Snyder, and J. a. Robinson (2012, April). Substrate considerations for graphene synthesis on thin copper films. *Nanotechnology 23*(13), 135601.

[45] Hsieh, Y.-P., Y.-W. Wang, C.-C. Ting, H.-C. Wang, K.-Y. Chen, and C.-C. Yang (2013). Effect of Catalyst Morphology on the Quality of CVD Grown Graphene. *Journal of Nanomaterials 2013*, 1–6.

[46] Hu, B., H. Ago, Y. Ito, K. Kawahara, M. Tsuji, E. Magome, K. Sumitani, N. Mizuta, K.-i. Ikeda, and S. Mizuno (2012a, January). Epitaxial growth of large-area single-layer graphene over Cu(111)/sapphire by atmospheric pressure CVD. *Carbon 50*(1), 57–65.

[47] Hu, B., H. Ago, Y. Ito, K. Kawahara, M. Tsuji, E. Magome, K. Sumitani, N. Mizuta, K.-i. Ikeda, and S. Mizuno (2012b, January). Epitaxial growth of large-area single-layer graphene over Cu(111)/sapphire by atmospheric pressure CVD. *Carbon 50*(1), 57–65.

[48] Hu, Baoshan; Ago, Hiroki; Orofeo, Carlo M.; Ogawa, Y. and M. Tsuji (2012). On the nucleation of graphene by chemical vapor deposition.

[49] Huang, H., W. Chen, S. Chen, A. Thye, and S. Wee (2008). Bottom-up Growth of Epitaxial. *2*(12), 2513–2518.

[50] Huang, P. Y., C. S. Ruiz-Vargas, A. M. van der Zande, W. S. Whitney, M. P. Levendorf, J. W. Kevek, S. Garg, J. S. Alden, C. J. Hustedt, Y. Zhu, J. Park, P. L. McEuen, and D. a. Muller (2011, January). Grains

and grain boundaries in single-layer graphene atomic patchwork quilts. *Nature 469*(7330), 389–92.

[51] Humphreys, F. J., M. Materials, and S. Centre (2001). Grain and subgrain characterisation by electron backscatter diffraction. *6*, 3833–3854.

[52] Hwang, J.-Y., C.-C. Kuo, L.-C. Chen, and K.-H. Chen (2010, November). Correlating defect density with carrier mobility in large-scaled graphene films: Raman spectral signatures for the estimation of defect density. *Nanotechnology 21*(46), 465705.

[53] Iqbal, M. W., A. K. Singh, M. Z. Iqbal, and J. Eom (2012, August). Raman fingerprint of doping due to metal adsorbates on graphene. *Journal of physics. Condensed matter : an Institute of Physics journal 24*(33), 335301.

[54] IUPAC (2014). *Compendium of Chemical Terminology* (2nd ed.). IUPAC.

[55] Jobst, J., D. Waldmann, F. Speck, R. Hirner, D. K. Maude, T. Seyller, and H. B. Weber (2010, May). Quantum oscillations and quantum Hall effect in epitaxial graphene. *Physical Review B 81*(19), 195434.

[56] Kennefick, C. M., R. Raj, and B. Hall (1989). ON SAPPHIRE : STABILITY THIN FILMS AT 0 . 7 T ,. *37*(11).

[57] Kidambi, Piran R; Ducati, Caterina; Dlubak, Bruno; Gardiner, Damian; Weatherup, Robert S.; Martin, Marie-Blandine; Seneor, Pierre; Coles, Harry; Hofmann, S. (2012). The Parameter Space of Graphene Chemical Vapor Deposition on Polycrystalline Cu.

[58] Kim, S.-H., S. Z. Han, C. J. Kim, I.-Y. Hwang, and F. Yin (2009). Evolution of Rolling Textures of Cold Rolled Copper Foils. *Materials Transactions 50*(3), 537–543.

[59] Kim, S. M., A. Hsu, Y.-H. Lee, M. Dresselhaus, T. Palacios, K. K. Kim, and J. Kong (2013, September). The effect of copper pre-cleaning on graphene synthesis. *Nanotechnology 24*(36), 365602.

[60] Kim, HoKwon; Mattevi, Cecilia; Calvo, M. Reyes; Oberg, Jenny C.; Artiglia, Luca; Agnoli, Stefano; Hirjibehedin, Cyrus F.; Chhowalla, Manish; Saiz, E. (2012). Activation Energy Paths for Graphene Nucleation and Growth on Cu.

[61] Klar, P; Lidorokis, E; Eckmann, A; Verzhbitskiy, I A; Ferrari, A C; Casiraghi, C. (2013). Raman scattering efficiency of graphene. *Physical Review B 87*, 205435–1–7.

[62] Klarskov, M. B. (2012). *Fabrication and Multiprobe Electrical Characterization of Nanostructures*. Ph. D. thesis, DTU.

[63] Kukovecz, A., D. Méhn, E. Nemes-Nagy, R. Szabó, and I. Kiricsi (2005, November). Optimization of CCVD synthesis conditions for single-wall carbon nanotubes by statistical design of experiments (DoE). *Carbon 43*(14), 2842–2849.

[64] Kumar, A. and C. H. Lee (2013). Synthesis and Biomedical Applications of Graphene : Present and Future Trends.

[65] Larsen, M. B. B., D. M. Mackenzie, J. M. Caridad, P. Bø ggild, and T. J. Booth (2014, June). Transfer induced compressive strain in graphene: Evidence from Raman spectroscopic mapping. *Microelectronic Engineering 121*, 113–117.

[66] Lemme, M. C., S. Member, T. J. Echtermeyer, M. Baus, and H. Kurz (2007). A Graphene Field-Effect Device. *28*(4), 282–284.

[67] Levendorf, M. P., C. S. Ruiz-Vargas, S. Garg, and J. Park (2009, December). Transfer-free batch fabrication of single layer graphene transistors. *Nano letters 9*(12), 4479–83.

[68] Li, X., W. Cai, J. An, S. Kim, J. Nah, D. Yang, R. Piner, A. Velamakanni, I. Jung, E. Tutuc, S. K. Banerjee, L. Colombo, and R. S. Ruoff (2009, June). Large-area synthesis of high-quality and uniform graphene films on copper foils. *Science (New York, N.Y.) 324*(5932), 1312–4.

[69] Li, X., C. W. Magnuson, A. Venugopal, J. An, J. W. Suk, B. Han, M. Borysiak, W. Cai, A. Velamakanni, Y. Zhu, L. Fu, E. M. Vogel, E. Voelkl, L. Colombo, and R. S. Ruoff (2010, November). Graphene films with large domain size by a two-step chemical vapor deposition process. *Nano letters 10*(11), 4328–34.

[70] Lin, Y., C. Dimitrakopoulos, K. A. Jenkins, D. B. Farmer, H. Chiu, A. Grill, and P. Avouris (2010). 100-GHz Transistors from Wafer-Scale Epitaxial Graphene. *Science*, 662.

[71] Lindahl, N. (2012). *Nanoelectromechanical Systems from Carbon Nanotubes and Graphene Nanoelectromechanical Systems from Carbon Nanotubes and Graphene*.

[72] Lipatov, A., A. Varezhnikov, P. Wilson, V. Sysoev, A. Kolmakov, and A. Sinitskii (2013, June). Highly selective gas sensor arrays based on thermally reduced graphene oxide. *Nanoscale 5*(12), 5426–34.

[73] Lu, Y.-F., S.-T. Lo, J.-C. Lin, W. Zhang, J.-Y. Lu, F.-H. Liu, C.-M. Tseng, Y.-H. Lee, C.-T. Liang, and L.-J. Li (2013, August). Nitrogen-doped graphene sheets grown by chemical vapor deposition: synthesis and influence of nitrogen impurities on carrier transport. *ACS nano 7*(8), 6522–32.

[74] Lv, R., Q. Li, A. R. Botello-Méndez, T. Hayashi, B. Wang, A. Berkdemir, Q. Hao, A. L. Elías, R. Cruz-Silva, H. R. Gutiérrez, Y. A. Kim, H. Muramatsu, J. Zhu, M. Endo, H. Terrones, J.-C. Charlier, M. Pan, and M. Terrones (2012, January). Nitrogen-doped graphene: beyond single substitution and enhanced molecular sensing. *Scientific reports 2*, 586.

[75] Madras, G. and B. J. McCoy (2001). Distribution kinetics theory of Ostwald ripening. *The Journal of Chemical Physics 115*(14), 6699.

[76] Madras, G. and B. J. McCoy (2002). Ostwald ripening with size-dependent rates: Similarity and power-law solutions. *The Journal of Chemical Physics 117*(17), 8042.

[77] Mattevi, C., H. Kim, and M. Chhowalla (2011). A review of chemical vapour deposition of graphene on copper. *Journal of Materials Chemistry 21*(10), 3324.

[78] Mayorov, A. S., R. V. Gorbachev, S. V. Morozov, L. Britnell, R. Jalil, L. a. Ponomarenko, P. Blake, K. S. Novoselov, K. Watanabe, T. Taniguchi, and a. K. Geim (2011, June). Micrometer-scale ballistic transport in encapsulated graphene at room temperature. *Nano letters 11*(6), 2396–9.

[79] Meca, E., J. Lowengrub, H. Kim, C. Mattevi, and V. B. Shenoy (2013, January). Epitaxial graphene growth and shape dynamics on copper: phase-field modeling and experiments. *Nano letters 13*(11), 5692–7.

[80] Miller, D. L., M. W. Keller, J. M. Shaw, A. N. Chiaramonti, and R. R. Keller (2012). Epitaxial (111) films of Cu, Ni, and CuxNiy on αâˆ'Al2O3

(0001) for graphene growth by chemical vapor deposition. *Journal of Applied Physics 112*(6), 064317.

[81] Mø lgaard, M., M. Larsen, and T. Booth (2013). Copper grains for graphene growth. Technical Report July, DTU.

[82] Mohiuddin, T., a. Lombardo, R. Nair, a. Bonetti, G. Savini, R. Jalil, N. Bonini, D. Basko, C. Galiotis, N. Marzari, K. Novoselov, a. Geim, and a. Ferrari (2009, May). Uniaxial strain in graphene by Raman spectroscopy: G peak splitting, Grüneisen parameters, and sample orientation. *Physical Review B 79*(20), 205433.

[83] Montgomery, D. C. (2008). *Design and analysis of experiments* (7th ed.). Wiley.

[84] Nair, R. R.; Blake, P.; Grigorenko, A. N.; Novoselov, K. S.; Booth, T. J.; Stauber, T; Peres, N. M. R.; Geim, A. K. (2008, June). Fine structure constant defines visual transparency of graphene. *Science (New York, N.Y.) 320*(5881), 1308.

[85] Nemanich, R. J., X. Palo, P. Alto, and S. A. Solin (1977). Infrared active optical vibrations of graphite. *Solid 23*(2), 117–120.

[86] Niu, T., M. Zhou, J. Zhang, Y. Feng, and W. Chen (2013, June). Growth intermediates for CVD graphene on Cu(111): carbon clusters and defective graphene. *Journal of the American Chemical Society 135*(22), 8409–14.

[87] Novoselov, K. S., A. K. Geim, S. V. Morozov, and D. Jiang (2004). Electric Field Effect in Atomically Thin Carbon Films. *306*(October), 666–669.

[88] Novoselov, K. S., D. Jiang, F. Schedin, T. J. Booth, V. V. Khotkevich, S. V. Morozov, and a. K. Geim (2005, July). Two-dimensional atomic crystals. *Proceedings of the National Academy of Sciences of the United States of America 102*(30), 10451–3.

[89] Novoselov, K. S., Z. Jiang, Y. Zhang, S. V. Morozov, H. L. Stormer, U. Zeitler, J. C. Maan, G. S. Boebinger, P. Kim, and A. K. Geim (2007). Room-Temperature Quantum Hall. *315*(March), 2007.

[90] Ostwald, W. (1896). *Lehrbuch der Allgemeinen Chemie* (Vol. 2 par ed.). Leipzig.

[91] Pallecchi, E., F. Lafont, V. Cavaliere, F. Schopfer, D. Mailly, W. Poirier, and a. Ouerghi (2014, January). High Electron Mobility in Epitaxial Graphene on 4H-SiC(0001) via post-growth annealing under hydrogen. *Scientific reports 4*, 4558.

[92] Peng, Z., Z. Yan, Z. Sun, and J. M. Tour (2011, October). Direct growth of bilayer graphene on SiOâ,, substrates by carbon diffusion through nickel. *ACS nano 5*(10), 8241–7.

[93] Petrone, N., C. R. Dean, I. Meric, A. M. van der Zande, P. Y. Huang, L. Wang, D. Muller, K. L. Shepard, and J. Hone (2012, June). Chemical vapor deposition-derived graphene with electrical performance of exfoliated graphene. *Nano letters 12*(6), 2751–6.

[94] Pizzocchero, F., P. BoÌ¸ggild, and T. J. Booth (2013). Carbon mediated reduction of silicon dioxide and growth of copper silicide particles in uniform width channels. *Journal of Applied Physics 114*(11), 114303.

[95] Pizzocchero, F., B. S. Jessen, P. R. Whelan, N. Kostesha, S. Lee, J. D. Buron, I. Petrushina, M. B. Larsen, P. Greenwood, W. J. Cha, K. Teo, P. U. Jepsen, J. Hone, P. Bø ggild, and T. J. Booth (2015, April). Non-destructive electrochemical graphene transfer from reusable thin-film catalysts. *Carbon 85*, 397–405.

[96] Ratke, Lorenz; Voorhees, P. W. (2002). *Growth and Coarsening: Ostwald Ripening in Material Processing*. Springer Science & Business Media.

[97] Reddy, K. M., A. D. Gledhill, C.-H. Chen, J. M. Drexler, and N. P. Padture (2011). High quality, transferrable graphene grown on single crystal Cu(111) thin films on basal-plane sapphire. *Applied Physics Letters 98*(11), 113117.

[98] Riedl, C., C. Coletti, and U. Starke (2010, September). Structural and electronic properties of epitaxial graphene on SiC(0001): a review of growth, characterization, transfer doping and hydrogen intercalation. *Journal of Physics D: Applied Physics 43*(37), 374009.

[99] Rollett, A., F. Humphreys, G. S. Rohrer, and M. Hatherly (2004). *Recrystallization and Related Annealing Phenomena* (2nd ed.). Pergamon.

[100] Ryu, J., Y. Kim, D. Won, N. Kim, J. S. Park, E.-K. Lee, D. Cho, S.-P. Cho, S. J. Kim, G. H. Ryu, H.-A.-S. Shin, Z. Lee, B. H. Hong, and S. Cho (2014, January). Fast synthesis of high-performance graphene films by

hydrogen-free rapid thermal chemical vapor deposition. *ACS nano 8*(1), 950–6.

[101] Sato, K., R. Saito, Y. Oyama, J. Jiang, L. Cançado, M. Pimenta, a. Jorio, G. Samsonidze, G. Dresselhaus, and M. Dresselhaus (2006, August). D-band Raman intensity of graphitic materials as a function of laser energy and crystallite size. *Chemical Physics Letters 427*(1-3), 117–121.

[102] Schedin, F., a. K. Geim, S. V. Morozov, E. W. Hill, P. Blake, M. I. Katsnelson, and K. S. Novoselov (2007, September). Detection of individual gas molecules adsorbed on graphene. *Nature materials 6*(9), 652–5.

[103] Schubert, E. F. (2014). Room temperature properties of Si, Ge, and GaAs Quantity.

[104] Schwierz, F. (2010, July). Graphene transistors. *Nature nanotechnology 5*(7), 487–96.

[105] Schwierz, F. (2013, July). Graphene Transistors: Status, Prospects, and Problems. *Proceedings of the IEEE 101*(7), 1567–1584.

[106] Simons, G. (2004). *Mechanical Size Effects in Thin Copper Foils : An Experimental Study*. Ph. D. thesis.

[107] Song, H. S., S. L. Li, H. Miyazaki, S. Sato, K. Hayashi, a. Yamada, N. Yokoyama, and K. Tsukagoshi (2012, January). Origin of the relatively low transport mobility of graphene grown through chemical vapor deposition. *Scientific reports 2*, 337.

[108] Tang, B., H. Guoxin, and H. Gao (2010, September). Raman Spectroscopic Characterization of Graphene. *Applied Spectroscopy Reviews 45*(5), 369–407.

[109] Tao, L., J. Lee, H. Chou, M. Holt, R. S. Ruoff, and D. Akinwande (2012, March). Synthesis of high quality monolayer graphene at reduced temperature on hydrogen-enriched evaporated copper (111) films. *ACS nano 6*(3), 2319–25.

[110] Tao, L., J. Lee, M. Holt, H. Chou, S. J. Mcdonnell, D. A. Ferrer, G. Babenco, R. M. Wallace, S. K. Banerjee, R. S. Ruo, and D. Akinwande (2012). Uniform Wafer-Scale Chemical Vapor Deposition of Graphene on Evaporated Cu (111) Film with Quality Comparable to Exfoliated Monolayer. (111).

[111] Thompson, C. V. and R. Carel (1996, May). Stress and grain growth in thin films. *Journal of the Mechanics and Physics of Solids 44*(5), 657–673.

[112] Tsurumi, J., Y. Saito, and P. Verma (2013, February). Evaluation of the interlayer interactions of few layers of graphene. *Chemical Physics Letters 557*, 114–117.

[113] Venezuela, P., M. Lazzeri, and F. Mauri (2011, March). Theory of double-resonant Raman spectra in graphene: intensity and line shape of defect-induced and two-phonon bands. pp. 1–28.

[114] Vlassiouuk, Ivan; Smirnov, Sergei; Regmi, Murari; Surwade, Sumedh P.; Srivastava, Nishtha; Feenstra, Randall; Eres, Gyula; Parish, Chad; Lavrik, Nick; Datskos, Panos; Dai, Sheng; Fulvio, P. (2013). Graphene Nucleation Density on Copper: Fundamental Role of Background Pressure.

[115] Wall, M. (2012). Raman Spectroscopy Optimizes Graphene Characterization. (April).

[116] Wang, C., W. Chen, C. Han, G. Wang, B. Tang, C. Tang, Y. Wang, W. Zou, X.-A. Zhang, S. Qin, S. Chang, and L. Wang (2014, January). Growth of millimeter-size single crystal graphene on Cu foils by circumfluence chemical vapor deposition. *Scientific reports 4*, 4537.

[117] Wang, H., G. Wang, P. Bao, S. Yang, W. Zhu, X. Xie, and W.-J. Zhang (2012, February). Controllable synthesis of submillimeter single-crystal monolayer graphene domains on copper foils by suppressing nucleation. *Journal of the American Chemical Society 134*(8), 3627–30.

[118] Wang, Y., Z. Ni, T. Yu, Z. X. Shen, H. Wang, Y. Wu, W. Chen, A. Thye, and S. Wee (2008). Raman Studies of Monolayer Graphene : The Substrate Effect. (0001), 10637–10640.

[119] Warman, M. (2013). CES 2013: Samsung flexible phone prototype unveiled.

[120] Wei, D., Y. Liu, Y. Wang, H. Zhang, L. Huang, and G. Yu (2009, May). Synthesis of N-doped graphene by chemical vapor deposition and its electrical properties. *Nano letters 9*(5), 1752–8.

[121] Wirtz, C., K. Lee, T. Hallam, and G. S. Duesberg (2014, March). Growth optimisation of high quality graphene from ethene at low temperatures. *Chemical Physics Letters 595-596*, 192–196.

[122] Wood, J. D., S. W. Schmucker, A. S. Lyons, E. Pop, and J. W. Lyding (2011). Effects of Polycrystalline Cu Substrate on Graphene Growth by Chemical Vapor Deposition. *Nano letters 11*, 4547–4554.

[123] Wright, S. I. and M. M. Nowell (2006). EBSD Image Quality Mapping. *Microscopy Microanalysis 12*, 72–84.

[124] Wu, B., D. Geng, Z. Xu, Y. Guo, L. Huang, Y. Xue, J. Chen, G. Yu, and Y. Liu (2013, February). Self-organized graphene crystal patterns. *NPG Asia Materials 5*(2), e36.

[125] Wu, P., W. Zhang, Z. Li, J. Yang, and J. G. Hou (2010, August). Communication: Coalescence of carbon atoms on Cu (111) surface: Emergence of a stable bridging-metal structure motif. *The Journal of chemical physics 133*(7), 071101.

[126] Yoon, D., H. Moon, and H. Cheong (2009). Variations in the Raman Spectrum as a Function of the Number of Graphene Layers. *55*(3), 1299–1303.

[127] Yu, Q., L. a. Jauregui, W. Wu, R. Colby, J. Tian, Z. Su, H. Cao, Z. Liu, D. Pandey, D. Wei, T. F. Chung, P. Peng, N. P. Guisinger, E. a. Stach, J. Bao, S.-S. Pei, and Y. P. Chen (2011, June). Control and characterization of individual grains and grain boundaries in graphene grown by chemical vapour deposition. *Nature materials 10*(6), 443–9.

[128] Yuan, W. and G. Shi (2013). Graphene-based gas sensors. *Journal of Materials Chemistry A 1*(35), 10078.

[129] Zabel, J., R. R. Nair, A. Ott, T. Georgiou, A. K. Geim, K. S. Novoselov, and C. Casiraghi (2012). Raman Spectroscopy of graphene and bilayer under biaxial strain : bubbles and balloons.

[130] Zhang, W., P. Wu, Z. Li, and J. Yang (2011, September). First-Principles Thermodynamics of Graphene Growth on Cu Surfaces. *The Journal of Physical Chemistry C 115*(36), 17782–17787.

[131] Zhang, X., J. Ning, X. Li, B. Wang, L. Hao, M. Liang, M. Jin, and L. Zhi (2013, September). Hydrogen-induced effects on the CVD growth of high-quality graphene structures. *Nanoscale 5*(18), 8363–6.

[132] Zhang, Y., Z. Li, P. Kim, L. Zhang, and C. Zhou (2012, January). Anisotropic hydrogen etching of chemical vapor deposited graphene. *ACS nano 6*(1), 126–32.

[133] Zhang, Y., Y.-W. Tan, H. L. Stormer, and P. Kim (2005, November). Experimental observation of the quantum Hall effect and Berry's phase in graphene. *Nature 438*(7065), 201–4.

[134] Zhao, J., S. Pei, W. Ren, L. Gao, and H.-M. Cheng (2010, September). Efficient preparation of large-area graphene oxide sheets for transparent conductive films. *ACS nano 4*(9), 5245–52.

[135] Zhao, P., A. Kumamoto, S. Kim, X. Chen, B. Hou, S. Chiashi, E. Einarsson, Y. Ikuhara, and S. Maruyama (2013, May). Self-Limiting Chemical Vapor Deposition Growth of Monolayer Graphene from Ethanol. *The Journal of Physical Chemistry C 117*(20), 10755–10763.

[136] Zielinski, E. M., R. P. Vinci, and J. C. Bravman (1994). Effects of barrier layer and annealing on abnormal grain growth in copper thin films. *Journal of Applied Physics 76*(8), 4516.

List of Tables

List of Figures

Appendices

Appendix A

Peak Fitting Script

The Matlab script used for fitting of Raman data is shown in the following section. Each spectrum is fitted using the script in A.1, and the peak heights, widths, areas, ratios, etc are analyzed using the the script in A.2.

A.1 Raman Peak Fitting

```
function
[FitResults,LowestError,BestStart,xi,yi]=peakfit(signal,center,window,NumPeaks,peakshape,extra,NumTrials
,start,AUTOZERO)

% Version 2.2: October, 2011. Fits Gaussian, equal-width Gaussians, exponentially-broadened

% Gaussian, Lorentzian, equal-width Lorentzians, Pearson, Logistic, exponential

% pulse, abd sigmoid shapes (expandable to other shapes).

%

% PEAKFIT(signal,center,window,NumPeaks,peakshape);

% Specifies the peak shape of the model: "peakshape" = 1-5.

% (1=Gaussian (default), 2=Lorentzian, 3=logistic, 4=Pearson,

% 5=exponentionally broadened Gaussian; 6=equal-width Gaussians;

% 7=Equal-width Lorentzians; 8=exponentionally broadened equal-width

% Gaussian, 9=exponential pulse, 10=sigmoid).

%

% [FitResults,MeanFitError]=PEAKFIT(signal,center,window...)

% Returns the FitResults vector in the order peak number, peak

% position, peak height, peak width, and peak area), and the MeanFitError

% (the percent RMS difference between the data and the model in the

% selected segment of that data) of the best fit.

%

% Optional output parameters

% 1. FitResults: a table of model peak parameters, one row for each peak,

%    listing Peak number, Peak position, Height, Width, and Peak area.

% 2. LowestError: The rms fitting error of the best trial fit.

% 3. BestStart: the starting guesses that gave the best fit.

% 4. xi: vector containing 100 interploated x-values for the model peaks.

% 5. yi: matrix containing the y values of each model peak at each xi.
```

```
%    Type plot(xi,yi(1,:)) to plot peak 1 or plot(xi,yi) to plot all peaks
%
% T. C. O'Haver (toh@umd.edu). Version 2.2
%
%
% Example 4:
% >> y=lorentzian(1:100,50,2);peakfit(y,50,100,1,2)
% Create and fit Lorentzian located at x=50, height=1, width=2.
%
%       Peak number  Peak position   Height     Width      Peak area
%           1          50      0.99974       1.9971       3.1079


%
% For more details, see
% http://terpconnect.umd.edu/~toh/spectrum/CurveFittingC.html and
% http://terpconnect.umd.edu/~toh/spectrum/InteractivePeakFitter.htm
%



% Remove baseline from data segment (alternative code)
% lxx=length(xx);
% bkgsize=10;
% if AUTOZERO==1,  % linear autozero operation
%    XX1=xx(1:round(lxx/bkgsize));
%    XX2=xx((lxx-round(lxx/bkgsize)):lxx);
%    Y1=yy(1:round(length(xx)/bkgsize));
```

```
%    Y2=yy((lxx-round(lxx/bkgsize)):lxx);
%    bkgcoef=polyfit([XX1,XX2],[Y1,Y2],1);  % Fit straight line to sub-group of points
%    bkg=polyval(bkgcoef,xx);
%    yy=yy-bkg;
% end % if

% Remove baseline from data segment
X1=min(xx);X2=max(xx);Y1=min(Y);Y2=max(Y);
if AUTOZERO==1, % linear autozero operation
  Y1=mean(yy(1:length(xx)/20));
  Y2=mean(yy((length(xx)-length(xx)/20):length(xx)));
  yy=yy-((Y2-Y1)/(X2-X1)*(xx-X1)+Y1);
end % if

if AUTOZERO==2, % Quadratic autozero operation
   XX1=xx(1:round(lxx/bkgsize));
   XX2=xx((lxx-round(lxx/bkgsize)):lxx);
   Y1=yy(1:round(length(xx)/bkgsize));
   Y2=yy((lxx-round(lxx/bkgsize)):lxx);
   bkgcoef=polyfit([XX1,XX2],[Y1,Y2],2);  % Fit parabola to sub-group of points
   bkg=polyval(bkgcoef,xx);
   yy=yy-bkg;
end % if autozero

% Perform peak fitting for selected peak shape using fminsearch function
options = optimset('TolX',.00001,'Display','off' );
```

```
LowestError=1000; % or any big number greater than largest error expected
FitParameters=zeros(1,NumPeaks.*2);
BestStart=zeros(1,NumPeaks.*2);
height=zeros(1,NumPeaks);
bestmodel=zeros(size(yy));
for k=1:NumTrials,
   % disp(['Trial number ' num2str(k) ] ) % optionally prints the current trial number as progress indicator
  switch peakshape
    case 2
       TrialParameters=fminsearch(@fitlorentzian,newstart,options,xx,yy);
       ShapeString='Lorentzian';
    end % switch peakshape

% Construct model from Trial parameters
A=zeros(NumPeaks,n);
for m=1:NumPeaks,
   switch peakshape

    case 2
       A(m,:)=lorentzian(xx,TrialParameters(2*m-1),TrialParameters(2*m));
    end % switch

switch NumPeaks % adds random variation to non-linear parameters
      case 1
        newstart=[newstart(1)*(1+randn/50) newstart(2)*(1+randn/10)];
      case 2
```

```
        newstart=[newstart(1)*(1+randn/50) newstart(2)*(1+randn/10) newstart(3)*(1+randn/50)
newstart(4)*(1+randn/10)];

      case 3

        newstart=[newstart(1)*(1+randn/50) newstart(2)*(1+randn/10) newstart(3)*(1+randn/50)
newstart(4)*(1+randn/10) newstart(5)*(1+randn/50) newstart(6)*(1+randn/10)];

      case 4

        newstart=[newstart(1)*(1+randn/50) newstart(2)*(1+randn/10) newstart(3)*(1+randn/50)
newstart(4)*(1+randn/10) newstart(5)*(1+randn/50) newstart(6)*(1+randn/10)  newstart(7)*(1+randn/50)
newstart(8)*(1+randn/10)];

      case 5

        newstart=[newstart(1)*(1+randn/50) newstart(2)*(1+randn/10) newstart(3)*(1+randn/50)
newstart(4)*(1+randn/10) newstart(5)*(1+randn/50) newstart(6)*(1+randn/10)  newstart(7)*(1+randn/50)
newstart(8)*(1+randn/10)  newstart(9)*(1+randn/50) newstart(10)*(1+randn/10)];

      otherwise

    end % switch NumPeaks

end % for

% Multiplies each row by the corresponding amplitude and adds them up

model=PEAKHEIGHTS'*A;


% Compare trial model to data segment and compute the fit error

  MeanFitError=100*norm(yy-model)./(sqrt(n)*max(yy));

  % Take only the single fit that has the lowest MeanFitError

  if MeanFitError<LowestError,

     if min(PEAKHEIGHTS)>0,  % Consider only fits with positive peak heights

       LowestError=MeanFitError;  % Assign LowestError to the lowest MeanFitError

       FitParameters=TrialParameters;  % Assign FitParameters to the fit with the lowest MeanFitError

       BestStart=newstart; % Assign BestStart to the start with the lowest MeanFitError

       height=PEAKHEIGHTS; % Assign height to the PEAKHEIGHTS with the lowest MeanFitError

       bestmodel=model; % Assign bestmodel to the model with the lowest MeanFitError
```

```
    end % if min(PEAKHEIGHTS)>0
  end % if MeanFitError<LowestError
end % for k (NumTrials)
%
% Construct model from best-fit parameters
AA=zeros(NumPeaks,100);
xxx=linspace(min(xx),max(xx));
for m=1:NumPeaks,
   switch peakshape

    case 2
       AA(m,:)=lorentzian(xxx,FitParameters(2*m-1),FitParameters(2*m));
       otherwise
  end % switch
end % for

% Multiplies each row by the corresponding amplitude and adds them up
heightsize=size(height');
AAsize=size(AA);
if heightsize(2)==AAsize(1),
   mmodel=height'*AA;
else
    mmodel=height*AA;
end

% Put results into a matrix, one row for each peak, showing peak index number,
```

```
% position, amplitude, and width.
for m=1:NumPeaks,
   if m==1,
      if peakshape==6||peakshape==7||peakshape==8, % equal-width peak models
        FitResults=[[round(m) FitParameters(m)+xoffset height(m) abs(FitParameters(NumPeaks+1))
area(m)]];
      else
        FitResults=[[round(m) FitParameters(2*m-1)+xoffset height(m) abs(FitParameters(2*m)) area(m)]];
      end % if peakshape
   else
      if peakshape==6||peakshape==7||peakshape==8, % equal-width peak models
        FitResults=[FitResults ; [round(m) FitParameters(m)+xoffset height(m)
abs(FitParameters(NumPeaks+1)) area(m)]];
      else
        FitResults=[FitResults ; [round(m) FitParameters(2*m-1)+xoffset height(m) abs(FitParameters(2*m))
area(m)]];
      end % if peakshape
    end % m==1
end % for m=1:NumPeaks

% ------------------------------------------------------------------
function start=calcstart(xx,NumPeaks,xoffset)
 n=max(xx)-min(xx);
 start=[];
 startpos=[n/(NumPeaks+1):n/(NumPeaks+1):n-(n/(NumPeaks+1))]+min(xx);
 for marker=1:NumPeaks,
    markx=startpos(marker)+ xoffset;
    start=[start markx n/5];
```

```
  end % for marker
% --------------------------------------------------------------------
function [index,closestval]=val2ind(x,val)
% Returns the index and the value of the element of vector x that is closest to val
% If more than one element is equally close, returns vectors of indicies and values
% Tom O'Haver (toh@umd.edu) October 2006
% Examples: If x=[1 2 4 3 5 9 6 4 5 3 1], then val2ind(x,6)=7 and val2ind(x,5.1)=[5 9]
% [indices values]=val2ind(x,3.3) returns indices = [4 10] and values = [3 3]
dif=abs(x-val);
index=find((dif-min(dif))==0);
closestval=x(index);
% --------------------------------------------------------------------
% --------------------------------------------------------------------
function err = fitlorentzian(lambda,t,y)
%                   Fitting function for single lorentzian, lambda(1)=position, lambda(2)=width
%                   Fitgauss assumes a lorentzian function
global PEAKHEIGHTS
A = zeros(length(t),round(length(lambda)/2));
for j = 1:length(lambda)/2,
   A(:,j) = lorentzian(t,lambda(2*j-1),lambda(2*j))';
end
PEAKHEIGHTS = A\y';
z = A*PEAKHEIGHTS;
err = norm(z-y');
% --------------------------------------------------------------------
function g = lorentzian(x,position,width)
```

```
% lorentzian(x,position,width) Lorentzian function.
% where x may be scalar, vector, or matrix
% position and width scalar
% T. C. O'Haver, 1988
% Example: lorentzian([1 2 3],2,2) gives result [0.5 1 0.5]
g=ones(size(x))./(1+((x-position)./(0.5.*width)).^2);
% ---------------------------------------------------------------------
```

A.2 Raman Data Analysis

```
%% Plots Raman map data from Omnic software- previous analyised by
run_spectrum_analysis_multi.m
clc;
clear all;
[matfilename, pathname] = uigetfile('*.mat', 'Select .mat-file','MultiSelect',
'off');
% Convert to readable format
tempstr = load(matfilename); %for testing only
tempcell=struct2cell(tempstr);
master=cell2mat(tempcell);


ErrorThreshold=15; %Error threshold in percent
DErrorThreshold=ErrorThreshold;
DDErrorThreshold=ErrorThreshold;
GErrorThreshold=ErrorThreshold; % Just in case you need to change on invidually...

threshold=1e5; %% Over this value of counts and it's assumes to be an error.

stepsize=input('Step size in nm: ');
h = input('Width of Map in steps: ');
jj=size(master);
w=jj(2)/h;
k=1;
%Allows Matlab to plot the scales correctly
ylength=(1:w)*stepsize;
xlength=(1:h)*stepsize;
for i=1:w
    for j=1:h
         D(i,j) = master(3,k);
         G(i,j) = master(7,k);
         DD(i,j) = master(11,k);
         Dpos(i,j) = master(2,k);
         Gpos(i,j) = master(6,k);
         DDpos(i,j) = master(10,k);
         Derror(i,j) = master(5,k);
         Gerror(i,j) = master(9,k);
         DDerror(i,j) = master(13,k);
         FWHMG(i,j) = master(8,k);
         FWHMDD(i,j) = master(12,k);
         k = k+1;
    end
end


   for i=1:w
    for j=1:h
                if Gerror(i,j)>GErrorThreshold
            D(i,j)=0.0;
            G(i,j)=0.0;
            DD(i,j)=0.0;
            FWHMG(i,j)=0.0;
            FWHMDD(i,j)=0.0;
```

```
            Gpos(i,j)=0.0;
            Dpos(i,j)=0.0;
            DDpos(i,j)=0.0;
        else
            D(i,j)=D(i,j);
            G(i,j)=G(i,j);
            DD(i,j)=DD(i,j);
            FWHMG(i,j)=FWHMG(i,j);
            FWHMDD(i,j)=FWHMDD(i,j);
            Gpos(i,j)=Gpos(i,j);
            Dpos(i,j)=Dpos(i,j);
            DDpos(i,j)=DDpos(i,j);
        end
    end
   end


for i=1:w
    for j=1:h
        if D(i,j)>100;
            D(i,j)=0;
        elseif D(i,j)==0
                        D(i,j)=0;
        else
            D(i,j)=D(i,j);
        end
    end
end
for i=1:w
    for j=1:h
        if G(i,j)>threshold;
             G(i,j)=1;
        elseif G(i,j)==0
             G(i,j)=1;
        else
             G(i,j)=G(i,j);
        end
    end
end
for i=1:w
    for j=1:h
        if DD(i,j)>threshold;
             DD(i,j)=1;
        elseif  DD(i,j)==0
             DD(i,j)=0;
        else
             DD(i,j)=DD(i,j);
        end
    end
end

%Define even more varaibles
 DDoverG=DD./G;
 DoverG=D./G;
```

```
 for i=1:w
    for j=1:h
        chip=isinf(DoverG(i,j));
        if chip==1
            DoverG(i,j)=0;
        else
            DoverG(i,j)=DoverG(i,j);
        end
    end
end


 for i=1:w
    for j=1:h
        chip=isinf(DDoverG(i,j));
        if chip==1
            DDoverG(i,j)=0;
        else
            DDoverG(i,j)=DDoverG(i,j);
        end
    end
 end

% Exclude values which are just noise of the substrate
DoverGThreshold=10;DDoverGThreshold=5;
 for i=1:w
    for j=1:h
        if DoverG(i,j)==0.0
            DoverG(i,j)=-0.1;
        else
            DoverG(i,j)=DoverG(i,j);
        end
    end
end
% surf

 for i=1:w
    for j=1:h
                if DDoverG(i,j)>DDoverGThreshold
            DDoverG(i,j)=0.0;
        else
            DDoverG(i,j)=DDoverG(i,j);
        end
    end
 end
  for i=1:w
    for j=1:h
                if abs(Dpos(i,j))>1380
            Dpos(i,j)=0.0;
        else
            Dpos(i,j)=Dpos(i,j);
```

```
        end
    end
 end
   for i=1:w
    for j=1:h
                if abs(DDpos(i,j))>2750
            DDpos(i,j)=0.0;
        else
            DDpos(i,j)=DDpos(i,j);
        end
    end
   end
   for i=1:w
    for j=1:h
                if abs(Gpos(i,j))>1630
            Gpos(i,j)=0.0;
        else
            Gpos(i,j)=Gpos(i,j);
        end
    end
   end
   for i=1:w
    for j=1:h
                if (FWHMG(i,j))>75
            FWHMG(i,j)=0.0;
        else
            FWHMG(i,j)=FWHMG(i,j);
        end
    end
   end
    for i=1:w
    for j=1:h
                if (FWHMDD(i,j))>100
            FWHMDD(i,j)=0.0;
        else
            FWHMDD(i,j)=FWHMDD(i,j);
        end
    end
    end

   % Plot Shift in G peak
%
%
figure1 = figure('Colormap',...
[0 0 0;0 0 0.625;0 0 0.6875;0 0 0.75;0 0 0.8125;0 0 0.875;0 0 0.9375;0 0 1;0 0.0625
1;0 0.125 1;0 0.1875 1;0 0.25 1;0 0.3125 1;0 0.375 1;0 0.4375 1;0 0.5 1;0 0.5625
1;0 0.625 1;0 0.6875 1;0 0.75 1;0 0.8125 1;0 0.875 1;0 0.9375 1;0 1 1;0.0625 1
0.9375;0.125 1 0.875;0.1875 1 0.8125;0.25 1 0.75;0.3125 1 0.6875;0.375 1
0.625;0.4375 1 0.5625;0.5 1 0.5;0.5625 1 0.4375;0.625 1 0.375;0.6875 1 0.3125;0.75
1 0.25;0.8125 1 0.1875;0.875 1 0.125;0.9375 1 0.0625;1 1 0;1 0.9375 0;1 0.875 0;1
0.8125 0;1 0.75 0;1 0.6875 0;1 0.625 0;1 0.5625 0;1 0.5 0;1 0.4375 0;1 0.375 0;1
0.3125 0;1 0.25 0;1 0.1875 0;1 0.125 0;1 0.0625 0;1 0 0;0.949999988079071
0.025000000372529 0;0.899999976158142 0.0500000007450581 0;0.850000023841858
0.0750000029802322 0;0.800000011920929 0.100000001490116 0;0.75 0.125
```

```
0;0.700000047683716 0.150000005960464 0;0.650000035762787 0.174999997019768
0;0.600000023841858 0.200000002980232 0]);
axes1 = axes('Parent',figure1,'LineWidth',2,'FontSize',24,'CLim',[1570 1630]);
grid(axes1,'on');
hold(axes1,'all');
% Create surf
surf(xlength./1000,ylength./1000,Gpos,'Parent',axes1,'EdgeColor','none');
% Create xlabel
xlabel('Position (\mum)','FontSize',24);
% Create ylabel
ylabel('Position (\mum)','FontSize',24);
% Create zlabel
zlabel('Intensity (arb. units)','FontSize',24);
% Create title
title('G peak position [cm^{-1}]','FontSize',24);
xlim(axes1,[0 stepsize*h/1000]);ylim(axes1,[0 stepsize*w/1000]);
colorbar('peer',axes1);
axis equal;axis tight
hold on
style
filepath = 'C:\Users\mbar\Dropbox\DTU\PhD\Raman\Pressure\Matlab\Gpos\';
filename = matfilename;
set(gcf,'color',[1 1 1])
export_fig(fullfile(filepath,filename),'-png','-pdf','-m3.0')

% Plot Shift in D peak
figure2 = figure('Colormap',...
[0 0 0;0 0 0.625;0 0 0.6875;0 0 0.75;0 0 0.8125;0 0 0.875;0 0 0.9375;0 0 1;0 0.0625
1;0 0.125 1;0 0.1875 1;0 0.25 1;0 0.3125 1;0 0.375 1;0 0.4375 1;0 0.5 1;0 0.5625
1;0 0.625 1;0 0.6875 1;0 0.75 1;0 0.8125 1;0 0.875 1;0 0.9375 1;0 1 1;0.0625 1
0.9375;0.125 1 0.875;0.1875 1 0.8125;0.25 1 0.75;0.3125 1 0.6875;0.375 1
0.625;0.4375 1 0.5625;0.5 1 0.5;0.5625 1 0.4375;0.625 1 0.375;0.6875 1 0.3125;0.75
1 0.25;0.8125 1 0.1875;0.875 1 0.125;0.9375 1 0.0625;1 1 0;1 0.9375 0;1 0.875 0;1
0.8125 0;1 0.75 0;1 0.6875 0;1 0.625 0;1 0.5625 0;1 0.5 0;1 0.4375 0;1 0.375 0;1
0.3125 0;1 0.25 0;1 0.1875 0;1 0.125 0;1 0.0625 0;1 0 0;0.9375 0 0;0.875 0 0;0.8125
0 0;0.75 0 0;0.6875 0 0;0.625 0 0;0.5625 0 0;0.5 0 0]);
axes2 = axes('Parent',figure2,'LineWidth',2,'FontSize',24,'CLim',[1320 1380]);
grid(axes2,'on');
hold(axes2,'all');
% Create surf
surf(xlength./1000,ylength./1000,Dpos,'Parent',axes2,'EdgeColor','none');
% Create xlabel
xlabel('Position (\mum)','FontSize',24);
% Create ylabel
ylabel('Position (\mum)','FontSize',24);
% Create zlabel
zlabel('Intensity (arb. units)','FontSize',24);
% Create title
title('D peak position [cm^{-1}]','FontSize',24);
xlim(axes2,[0 stepsize*h/1000]);ylim(axes2,[0 stepsize*w/1000]);
colorbar('peer',axes2);
axis equal;axis tight
hold on
style
```

```
filepath = 'C:\Users\mbar\Dropbox\DTU\PhD\Raman\Pressure\Matlab\Dpos\';
filename = matfilename;
set(gcf,'color',[1 1 1])
export_fig(fullfile(filepath,filename),'-png','-pdf','-m3.0')


% Plot Shift in 2D peak
figure3 = figure('Colormap',...
[0 0 0;0 0 0.625;0 0 0.6875;0 0 0.75;0 0 0.8125;0 0 0.875;0 0 0.9375;0 0 1;0 0.0625
1;0 0.125 1;0 0.1875 1;0 0.25 1;0 0.3125 1;0 0.375 1;0 0.4375 1;0 0.5 1;0 0.5625
1;0 0.625 1;0 0.6875 1;0 0.75 1;0 0.8125 1;0 0.875 1;0 0.9375 1;0 1 1;0.0625 1
0.9375;0.125 1 0.875;0.1875 1 0.8125;0.25 1 0.75;0.3125 1 0.6875;0.375 1
0.625;0.4375 1 0.5625;0.5 1 0.5;0.5625 1 0.4375;0.625 1 0.375;0.6875 1 0.3125;0.75
1 0.25;0.8125 1 0.1875;0.875 1 0.125;0.9375 1 0.0625;1 1 0;1 0.9375 0;1 0.875 0;1
0.8125 0;1 0.75 0;1 0.6875 0;1 0.625 0;1 0.5625 0;1 0.5 0;1 0.4375 0;1 0.375 0;1
0.3125 0;1 0.25 0;1 0.1875 0;1 0.125 0;1 0.0625 0;1 0 0;0.9375 0 0;0.875 0 0;0.8125
0 0;0.75 0 0;0.6875 0 0;0.625 0 0;0.5625 0 0;0.5 0 0]);
axes3 = axes('Parent',figure3,'LineWidth',2,'FontSize',24,'CLim',[2650 2750]);
grid(axes3,'on');
hold(axes3,'all');
% Create surf
surf(xlength./1000,ylength./1000,DDpos,'Parent',axes3,'EdgeColor','none');
% Create xlabel
xlabel('Position (\mum)','FontSize',24);
% Create ylabel
ylabel('Position (\mum)','FontSize',24);
% Create zlabel
zlabel('Intensity (arb. units)','FontSize',24);
% Create title
title('2D peak position [cm^{-1}]','FontSize',24);
xlim(axes3,[0 stepsize*h/1000]);ylim(axes3,[0 stepsize*w/1000]);
colorbar('peer',axes3);
axis equal;axis tight
hold on
style
filepath = 'C:\Users\mbar\Dropbox\DTU\PhD\Raman\Pressure\Matlab\2Dpos\';
filename = matfilename;
set(gcf,'color',[1 1 1])
export_fig(fullfile(filepath,filename),'-png','-pdf','-m3.0')


% Make Ze Figures- 2D over G
figure4 = figure('Colormap',[0 0 0;0 0 0.625;0 0 0.6875;0 0 0.75;0 0 0.8125;0 0
0.875;0 0 0.9375;0 0 1;0 0.0625 1;0 0.125 1;0 0.1875 1;0 0.25 1;0 0.3125 1;0 0.375
1;0 0.4375 1;0 0.5 1;0 0.5625 1;0 0.625 1;0 0.6875 1;0 0.75 1;0 0.8125 1;0 0.875
1;0 0.9375 1;0 1 1;0.0625 1 0.9375;0.125 1 0.875;0.1875 1 0.8125;0.25 1 0.75;0.3125
1 0.6875;0.375 1 0.625;0.4375 1 0.5625;0.5 1 0.5;0.5625 1 0.4375;0.625 1
0.375;0.6875 1 0.3125;0.75 1 0.25;0.8125 1 0.1875;0.875 1 0.125;0.9375 1 0.0625;1 1
0;1 0.9375 0;1 0.875 0;1 0.8125 0;1 0.75 0;1 0.6875 0;1 0.625 0;1 0.5625 0;1 0.5
0;1 0.4375 0;1 0.375 0;1 0.3125 0;1 0.25 0;1 0.1875 0;1 0.125 0;1 0.0625 0;1 0
0;0.9375 0 0;0.875 0 0;0.8125 0 0;0.75 0 0;0.6875 0 0;0.625 0 0;0.5625 0 0;0.5 0
0]);
% Create axes
axes4 = axes('Parent',figure4,'LineWidth',2,'FontSize',24,'CLim',[0 3]);
```

```
grid(axes4,'on');
hold(axes4,'all');
% Create surf
surf(xlength./1000,ylength./1000,DDoverG,'Parent',axes4,'EdgeColor','none');
% Create xlabel
xlabel('Position (\mum)','FontSize',24);
% Create ylabel
ylabel('Position (\mum)','FontSize',24);
% Create zlabel
zlabel('Intensity (arb. units)','FontSize',24);
% Create title
title('2D/G Peak Intensity','FontSize',24);
xlim(axes4,[0 stepsize*h/1000]);ylim(axes4,[0 stepsize*w/1000]);
colorbar('peer',axes4);
axis equal;axis tight
hold on
style
filepath = 'C:\Users\mbar\Dropbox\DTU\PhD\Raman\Pressure\Matlab\2D-G\';
filename = matfilename;
set(gcf,'color',[1 1 1])
export_fig(fullfile(filepath,filename),'-png','-pdf','-m3.0')


% Make Ze Figure- D over G
figure5 = figure('Colormap',[0 0 0;0 0 0.625;0 0 0.6875;0 0 0.75;0 0 0.8125;0 0
0.875;0 0 0.9375;0 0 1;0 0.0625 1;0 0.125 1;0 0.1875 1;0 0.25 1;0 0.3125 1;0 0.375
1;0 0.4375 1;0 0.5 1;0 0.5625 1;0 0.625 1;0 0.6875 1;0 0.75 1;0 0.8125 1;0 0.875
1;0 0.9375 1;0 1 1;0.0625 1 0.9375;0.125 1 0.875;0.1875 1 0.8125;0.25 1 0.75;0.3125
1 0.6875;0.375 1 0.625;0.4375 1 0.5625;0.5 1 0.5;0.5625 1 0.4375;0.625 1
0.375;0.6875 1 0.3125;0.75 1 0.25;0.8125 1 0.1875;0.875 1 0.125;0.9375 1 0.0625;1 1
0;1 0.9375 0;1 0.875 0;1 0.8125 0;1 0.75 0;1 0.6875 0;1 0.625 0;1 0.5625 0;1 0.5
0;1 0.4375 0;1 0.375 0;1 0.3125 0;1 0.25 0;1 0.1875 0;1 0.125 0;1 0.0625 0;1 0
0;0.9375 0 0;0.875 0 0;0.8125 0 0;0.75 0 0;0.6875 0 0;0.625 0 0;0.5625 0 0;0.5 0
0]);
% Create axes
axes5 = axes('Parent',figure5,'LineWidth',2,'FontSize',24,'CLim',[0 1]);
grid(axes5,'on');
hold(axes5,'all');
% Create surf
surf(xlength./1000,ylength./1000,DoverG,'Parent',axes5,'EdgeColor','none');
% Create xlabel
xlabel('Position (\mum)','FontSize',24);
% Create ylabel
ylabel('Position (\mum)','FontSize',24);
% Create zlabel
zlabel('Intensity (arb. units)','FontSize',24);
% Create title
title('D/G Peak Intensity','FontSize',24);
xlim(axes5,[0 stepsize*h/1000]);ylim(axes5,[0 stepsize*w/1000]);
colorbar('peer',axes5);
axis equal;axis tight
hold on
style
filepath = 'C:\Users\mbar\Dropbox\DTU\PhD\Raman\Pressure\Matlab\D-G\';
```

```
filename = matfilename;
set(gcf,'color',[1 1 1])
export_fig(fullfile(filepath,filename),'-png','-pdf','-m3.0')


% Plot D peak only
%
%
figure6 = figure('Colormap',...
[0 0 0;0 0 0.625;0 0 0.6875;0 0 0.75;0 0 0.8125;0 0 0.875;0 0 0.9375;0 0 1;0 0.0625
1;0 0.125 1;0 0.1875 1;0 0.25 1;0 0.3125 1;0 0.375 1;0 0.4375 1;0 0.5 1;0 0.5625
1;0 0.625 1;0 0.6875 1;0 0.75 1;0 0.8125 1;0 0.875 1;0 0.9375 1;0 1 1;0.0625 1
0.9375;0.125 1 0.875;0.1875 1 0.8125;0.25 1 0.75;0.3125 1 0.6875;0.375 1
0.625;0.4375 1 0.5625;0.5 1 0.5;0.5625 1 0.4375;0.625 1 0.375;0.6875 1 0.3125;0.75
1 0.25;0.8125 1 0.1875;0.875 1 0.125;0.9375 1 0.0625;1 1 0;1 0.9375 0;1 0.875 0;1
0.8125 0;1 0.75 0;1 0.6875 0;1 0.625 0;1 0.5625 0;1 0.5 0;1 0.4375 0;1 0.375 0;1
0.3125 0;1 0.25 0;1 0.1875 0;1 0.125 0;1 0.0625 0;1 0 0;0.9375 0 0;0.875 0 0;0.8125
0 0;0.75 0 0;0.6875 0 0;0.625 0 0;0.5625 0 0;0.5 0 0]);
axes6 = axes('Parent',figure6,'LineWidth',2,'FontSize',24);
grid(axes6,'on');
hold(axes6,'all');
% Create surf
surf(xlength./1000,ylength./1000,D,'Parent',axes6,'EdgeColor','none');
% Create xlabel
xlabel('Position (\mum)','FontSize',24);
% Create ylabel
ylabel('Position (\mum)','FontSize',24);
% Create zlabel
zlabel('Intensity (arb. units)','FontSize',24);
% Create title
title('D Peak Intensity','FontSize',24);
xlim(axes6,[0 stepsize*h/1000]);ylim(axes6,[0 stepsize*w/1000]);
colorbar('peer',axes6);
axis equal;axis tight
hold on
style
filepath = 'C:\Users\mbar\Dropbox\DTU\PhD\Raman\Pressure\Matlab\Dpeak\';
filename = matfilename;
set(gcf,'color',[1 1 1])
export_fig(fullfile(filepath,filename),'-png','-pdf','-m3.0')

% Plot G peak only
%
%
figure7 = figure('Colormap',...
[0 0 0;0 0 0.625;0 0 0.6875;0 0 0.75;0 0 0.8125;0 0 0.875;0 0 0.9375;0 0 1;0 0.0625
1;0 0.125 1;0 0.1875 1;0 0.25 1;0 0.3125 1;0 0.375 1;0 0.4375 1;0 0.5 1;0 0.5625
1;0 0.625 1;0 0.6875 1;0 0.75 1;0 0.8125 1;0 0.875 1;0 0.9375 1;0 1 1;0.0625 1
0.9375;0.125 1 0.875;0.1875 1 0.8125;0.25 1 0.75;0.3125 1 0.6875;0.375 1
0.625;0.4375 1 0.5625;0.5 1 0.5;0.5625 1 0.4375;0.625 1 0.375;0.6875 1 0.3125;0.75
1 0.25;0.8125 1 0.1875;0.875 1 0.125;0.9375 1 0.0625;1 1 0;1 0.9375 0;1 0.875 0;1
0.8125 0;1 0.75 0;1 0.6875 0;1 0.625 0;1 0.5625 0;1 0.5 0;1 0.4375 0;1 0.375 0;1
0.3125 0;1 0.25 0;1 0.1875 0;1 0.125 0;1 0.0625 0;1 0 0;0.9375 0 0;0.875 0 0;0.8125
0 0;0.75 0 0;0.6875 0 0;0.625 0 0;0.5625 0 0;0.5 0 0]);
```

```
axes7 = axes('Parent',figure7,'LineWidth',2,'FontSize',24);
grid(axes7,'on');
hold(axes7,'all');
% Create surf
surf(xlength./1000,ylength./1000,G,'Parent',axes7,'EdgeColor','none');
% Create xlabel
xlabel('Position (\mum)','FontSize',24);
% Create ylabel
ylabel('Position (\mum)','FontSize',24);
% Create zlabel
zlabel('Intensity (arb. units)','FontSize',24);
% Create title
title('G Peak Intensity','FontSize',24);
xlim(axes7,[0 stepsize*h/1000]);ylim(axes7,[0 stepsize*w/1000]);
colorbar('peer',axes7);
axis equal;axis tight
hold on
style
filepath = 'C:\Users\mbar\Dropbox\DTU\PhD\Raman\Pressure\Matlab\Gpeak\';
filename = matfilename;
set(gcf,'color',[1 1 1])
export_fig(fullfile(filepath,filename),'-png','-pdf','-m3.0')


% Plot FWHM G
%
%
figure8 = figure('Colormap',...
[0 0 0;0 0 0.625;0 0 0.6875;0 0 0.75;0 0 0.8125;0 0 0.875;0 0 0.9375;0 0 1;0 0.0625
1;0 0.125 1;0 0.1875 1;0 0.25 1;0 0.3125 1;0 0.375 1;0 0.4375 1;0 0.5 1;0 0.5625
1;0 0.625 1;0 0.6875 1;0 0.75 1;0 0.8125 1;0 0.875 1;0 0.9375 1;0 1 1;0.0625 1
0.9375;0.125 1 0.875;0.1875 1 0.8125;0.25 1 0.75;0.3125 1 0.6875;0.375 1
0.625;0.4375 1 0.5625;0.5 1 0.5;0.5625 1 0.4375;0.625 1 0.375;0.6875 1 0.3125;0.75
1 0.25;0.8125 1 0.1875;0.875 1 0.125;0.9375 1 0.0625;1 1 0;1 0.9375 0;1 0.875 0;1
0.8125 0;1 0.75 0;1 0.6875 0;1 0.625 0;1 0.5625 0;1 0.5 0;1 0.4375 0;1 0.375 0;1
0.3125 0;1 0.25 0;1 0.1875 0;1 0.125 0;1 0.0625 0;1 0 0;0.9375 0 0;0.875 0 0;0.8125
0 0;0.75 0 0;0.6875 0 0;0.625 0 0;0.5625 0 0;0.5 0 0]);
axes8 = axes('Parent',figure8,'LineWidth',2,'FontSize',24,'CLim',[5 40]);
grid(axes8,'on');
hold(axes8,'all');
% Create surf
surf(xlength./1000,ylength./1000,FWHMG,'Parent',axes8,'EdgeColor','none');
% Create xlabel
xlabel('Position (\mum)','FontSize',24);
% Create ylabel
ylabel('Position (\mum)','FontSize',24);
% Create zlabel
zlabel('Intensity (arb. units)','FontSize',24);
% Create title
title('FWHM of G','FontSize',24);
xlim(axes8,[0 stepsize*h/1000]);ylim(axes8,[0 stepsize*w/1000]);
colorbar('peer',axes8);
axis equal;axis tight
hold on
```

```
style
filepath = 'C:\Users\mbar\Dropbox\DTU\PhD\Raman\Pressure\Matlab\FWHMG\';
filename = matfilename;
set(gcf,'color',[1 1 1])
export_fig(fullfile(filepath,filename),'-png','-pdf','-m3.0')


% Plot FWHM 2D
%
%
figure9 = figure('Colormap',...
[0 0 0;0 0 0.625;0 0 0.6875;0 0 0.75;0 0 0.8125;0 0 0.875;0 0 0.9375;0 0 1;0 0.0625
1;0 0.125 1;0 0.1875 1;0 0.25 1;0 0.3125 1;0 0.375 1;0 0.4375 1;0 0.5 1;0 0.5625
1;0 0.625 1;0 0.6875 1;0 0.75 1;0 0.8125 1;0 0.875 1;0 0.9375 1;0 1 1;0.0625 1
0.9375;0.125 1 0.875;0.1875 1 0.8125;0.25 1 0.75;0.3125 1 0.6875;0.375 1
0.625;0.4375 1 0.5625;0.5 1 0.5;0.5625 1 0.4375;0.625 1 0.375;0.6875 1 0.3125;0.75
1 0.25;0.8125 1 0.1875;0.875 1 0.125;0.9375 1 0.0625;1 1 0;1 0.9375 0;1 0.875 0;1
0.8125 0;1 0.75 0;1 0.6875 0;1 0.625 0;1 0.5625 0;1 0.5 0;1 0.4375 0;1 0.375 0;1
0.3125 0;1 0.25 0;1 0.1875 0;1 0.125 0;1 0.0625 0;1 0 0;0.9375 0 0;0.875 0 0;0.8125
0 0;0.75 0 0;0.6875 0 0;0.625 0 0;0.5625 0 0;0.5 0 0]);
axes9 = axes('Parent',figure9,'LineWidth',2,'FontSize',24,'CLim',[20 60]);
grid(axes9,'on');
hold(axes9,'all');
% Create surf
surf(xlength./1000,ylength./1000,FWHMDD,'Parent',axes9,'EdgeColor','none');
% Create xlabel
xlabel('Position (\mum)','FontSize',24);
% Create ylabel
ylabel('Position (\mum)','FontSize',24);
% Create zlabel
zlabel('Intensity (arb. units)','FontSize',24);
% Create title
title('FWHM of 2D','FontSize',24);
xlim(axes9,[0 stepsize*h/1000]);ylim(axes9,[0 stepsize*w/1000]);
colorbar('peer',axes9);
axis equal;axis tight
hold on
style
filepath = 'C:\Users\mbar\Dropbox\DTU\PhD\Raman\Pressure\Matlab\FWHM2D\';
filename = matfilename;
set(gcf,'color',[1 1 1])
export_fig(fullfile(filepath,filename),'-png','-pdf','-m3.0')
```

Appendix B

Example recipes for LPCVD growth of graphene

B.1 Example Recipe for CVD Graphene on Cu Foil

COMM H2, CH4, Ar, Ar
VALV 1 OPEN
WAIT PRES < 0.05
VALV 1 CLOSE
TUNE PCON pecvd at 6mbar
PCON ON 20.0 1.0
TUNE HTTC 1000C DTU
TUNE TOPH HT 1000C stable
TOPH ON 1000.0 200.0
HEAT ON 1000.0 200.0
WAIT TIME > 300
COMM wait for heater stabilisation
WAIT TEMP > 995.0
COMM start annealing
FLOW 6 ON 20
FLOW 2 ON 0
WAIT TIME > 600
COMM start growth
FLOW 3 ON 10
WAIT TIME > 600

COMM set growth time
TOPH OFF
HEAT OFF
PCON OFF
VALV 1 OPEN
COMM adding argon and hydrogen to cool
WAIT TEMP < 180.0
FLOW 2 OFF
FLOW 3 OFF
FLOW 6 OFF
WAIT PRES < 0.05

B.2 Example Recipe for CVD Graphene on Cu Film on SiO_2/Si

COMM H2, CH4, Ar, Ar
VALV 1 OPEN
TUNE PCON Fully open
PCON ON 1.0 1.0
FLOW 2 ON 1000
WAIT TIME > 15
FLOW 2 OFF
WAIT PRES < 0.20
VALV 1 CLOSE
FLOW 2 ON 1000
VALV 1 OPEN
WAIT TIME > 15
FLOW 2 OFF
WAIT PRES < 0.20
VALV 1 CLOSE
FLOW 6 ON 1000
TUNE PCON 25 MBAR AT 1000 SCCM
PCON ON 25.0 1.0
TUNE HTTC 950C 40 POWER
TUNE TOPH 900C 40 POWER
TOPH ON 500.0 150.0
HEAT ON 500.0 150.0
WAIT TIME > 30

WAIT TEMP > 495.0
WAIT TIME > 905
HEAT ON 950.0 50.0
TOPH ON 950.0 50.0
TUNE HTTC 1000C DTU
TUNE TOPH HT 1000C stable
WAIT TEMP > 955.0
WAIT TIME > 900
COMM start growth
FLOW 6 OFF
VALV 1 OPEN
WAIT TIME > 90
WAIT PRES < 0.40
TUNE PCON Graphene lowest pressure
PCON ON 1.0 1.0
FLOW 3 ON 4
FLOW 6 ON 800
WAIT TIME > 10
FLOW 3 OFF
VALV 1 CLOSE
COMM set cool down rate
TOPH ON 400.0 50.0
HEAT ON 400.0 50.0
WAIT TEMP < 500.0
HEAT OFF
TOPH OFF
PCON ON 50.0 1.0
FLOW 1 ON 500
FLOW 2 ON 500
WAIT TEMP < 200.0
PCON OFF
VALV 1 OPEN
WAIT TEMP < 120.0
FLOW 2 OFF
FLOW 1 OFF
WAIT PRES < 0.05

B.3 DOE Recipe for CVD Graphene on Cu Film on Sapphire

COMM Ar, Ar, CH4, x, x, H2
COMM FlushingChamber
VALV 1 OPEN
FLOW 2 ON 1000
WAIT TIME > 60
FLOW 2 OFF
WAIT PRES < 0.05
VALV 1 CLOSE
TUNE PCON Graphene bumpstop 15-90mbar
PCON ON 20.0 1.0
COMM Annealing
FLOW 6 ON 1000
FLOW 2 ON 1000
WAIT TIME > 120
COMM Initialise heaters
TUNE HTTC 00pcbumpstop
TUNE TOPH 00pcbumpstop
COMM Initialise heaters
COMM Heaters on - power limited!
HEAT ON 1200.0 200.0
TOPH ON 1200.0 200.0
TUNE HTTC 30pcbumpstop
TUNE TOPH 75pcbumpstop
WAIT TIME > 390
WAIT TEMP > 900.0
WAIT TIME > 1800
FLOW 2 ON 1000
FLOW 6 ON 1000
WAIT TIME > 60
FLOW 3 ON 5
WAIT TIME > 120
FLOW 3 OFF
COMM CoolDown
HEAT OFF
TOPH OFF
FLOW 6 OFF

FLOW 1 ON 2000
WAIT TEMP < 500.0
PCON OFF
VALV 1 OPEN
FLOW 2 ON 2000
WAIT TEMP < 130.0
FLOW 2 OFF
FLOW 1 OFF
WAIT PRES < 0.05

Appendix C

EDX data from Alfa Aesar copper foil and Goodfellow copper foil

Goodfellow copper foil before annealing

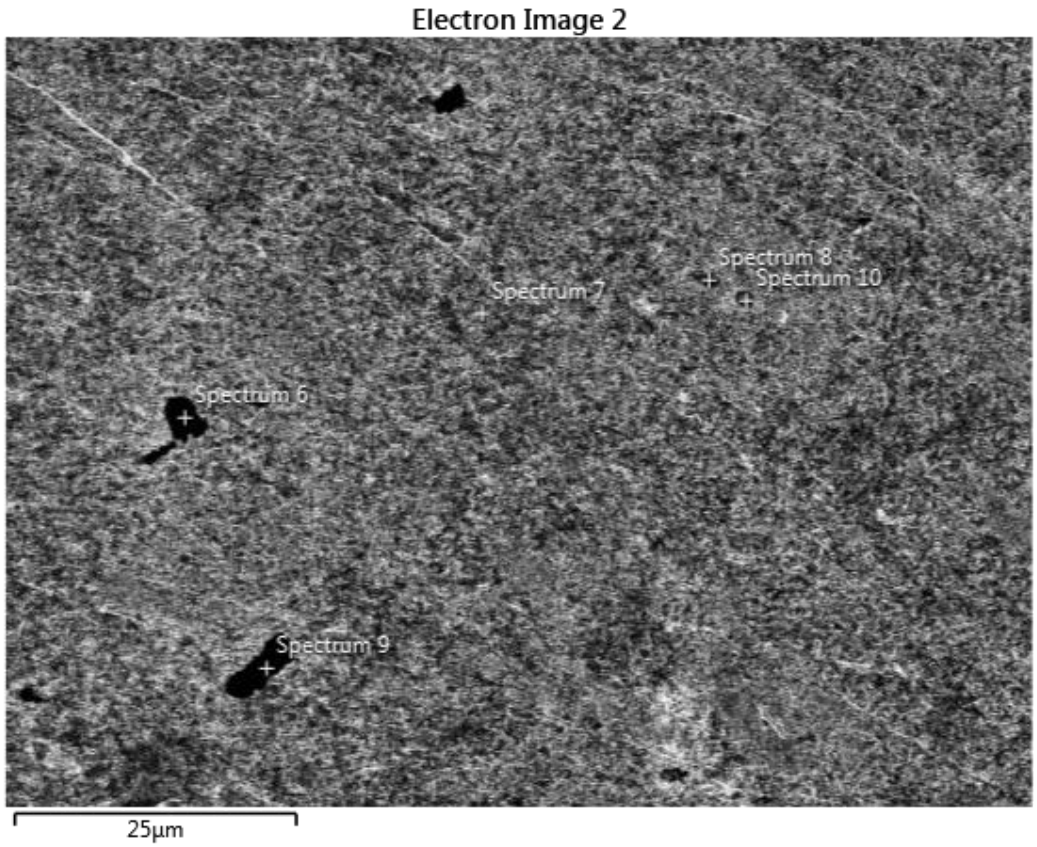

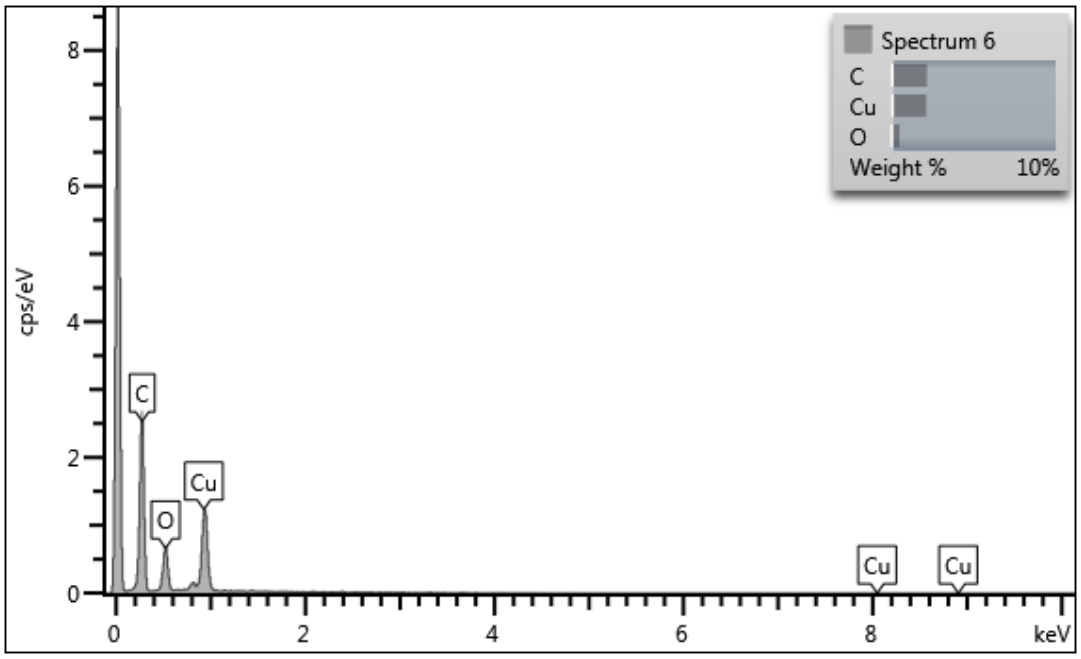

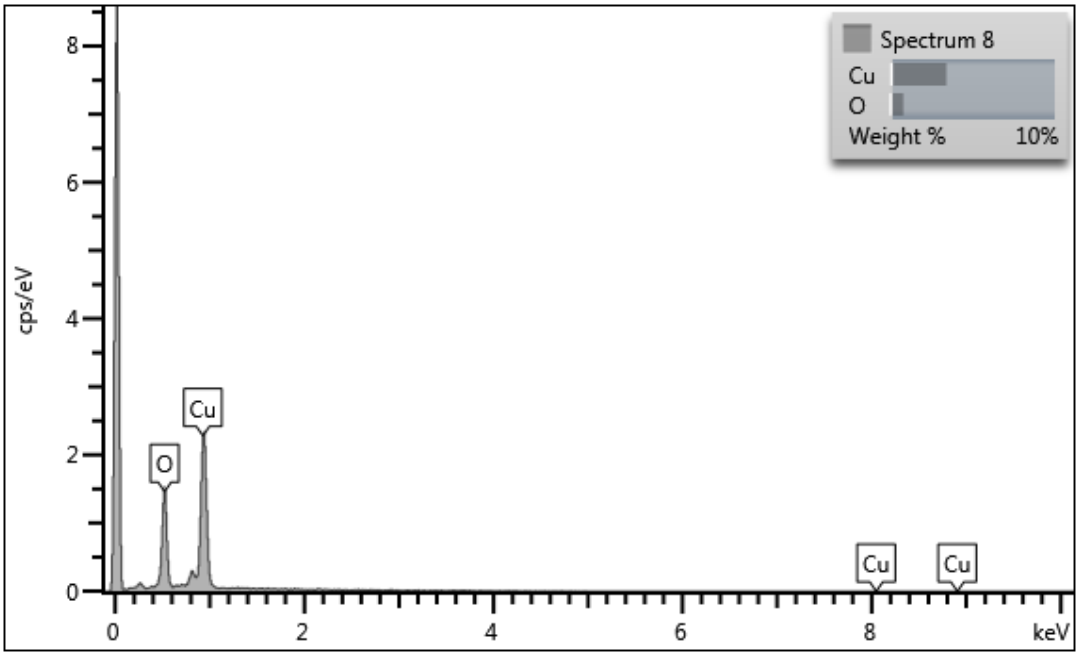

Goodfellow copper foil after annealing

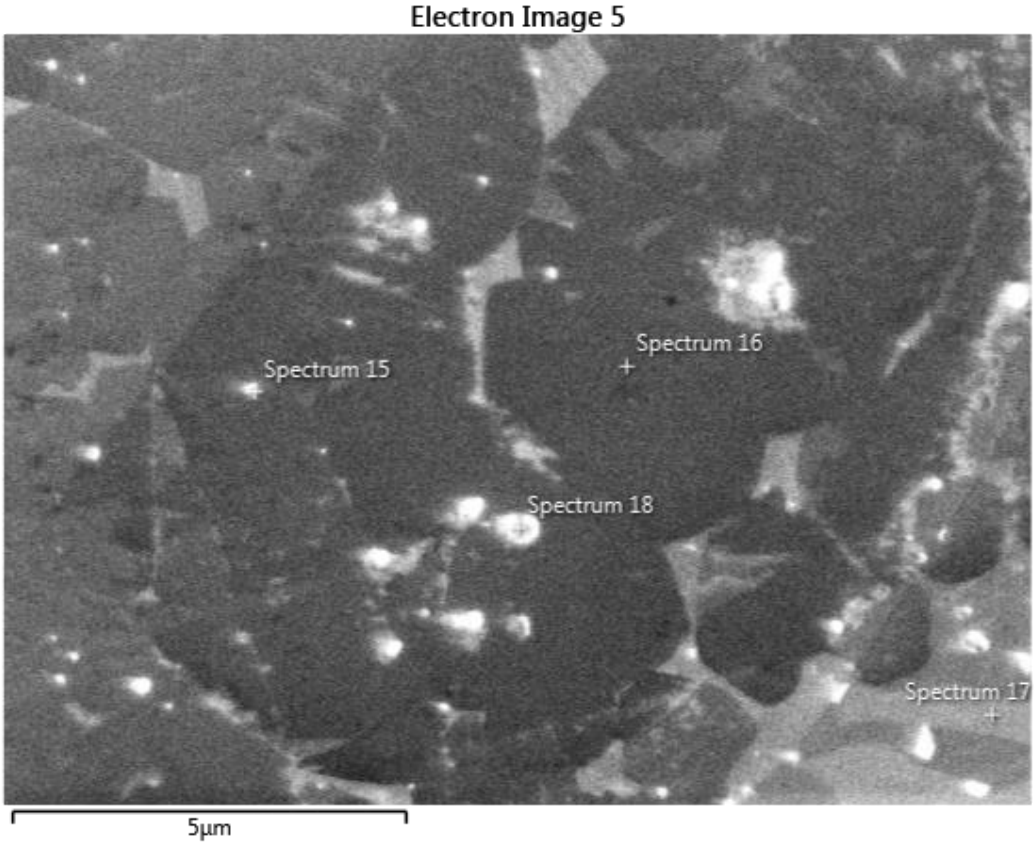

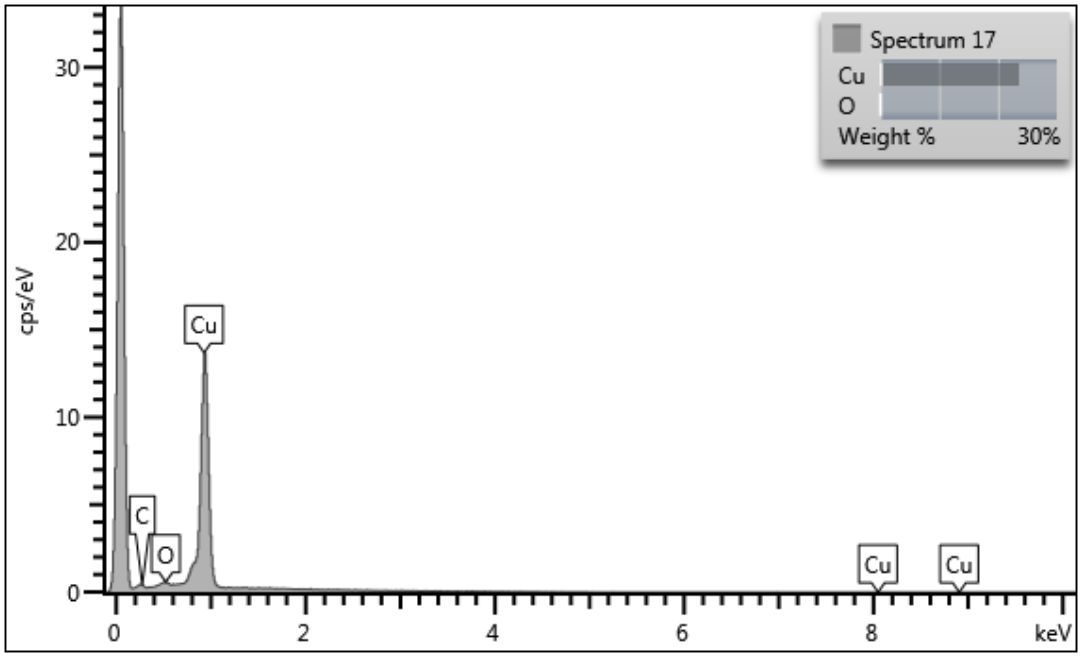
Spectrum 17
Cu
O
Weight %
30%
cps/eV
30
20
10
0
Cu
C
O
Cu
Cu
0
2
4
6
8
keV

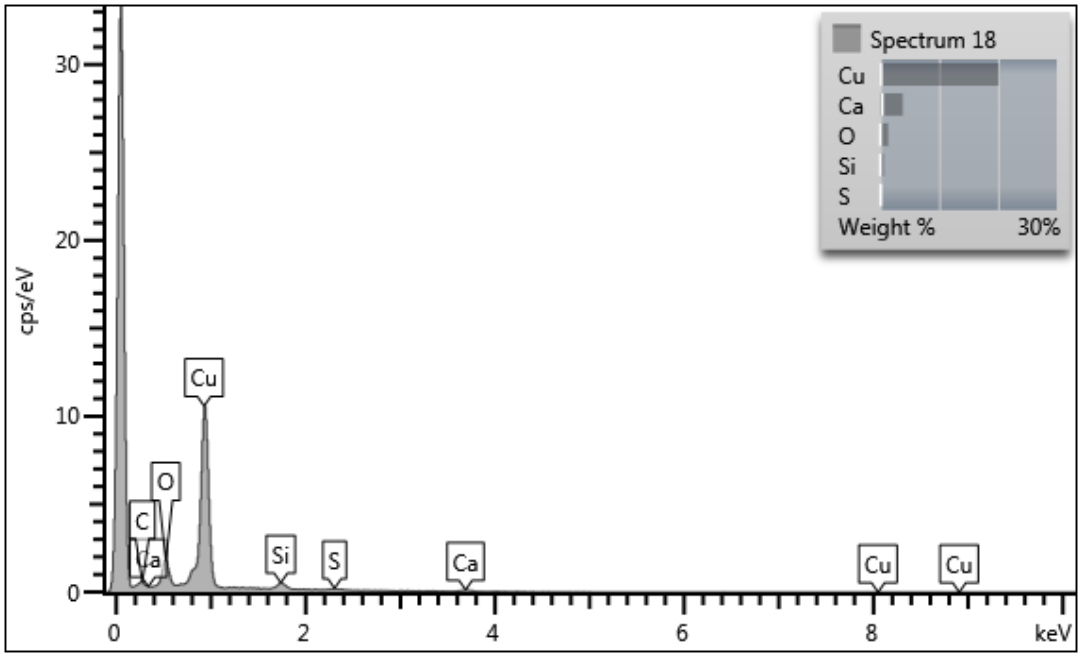
Spectrum 18
Cu
Ca
O
Si
S
Weight %
30%
cps/eV
30
20
10
0
Cu
O
C
Ca
Si
S
Ca
Cu
Cu
0
2
4
6
8
keV

Alfa Aesar copper foil before annealing

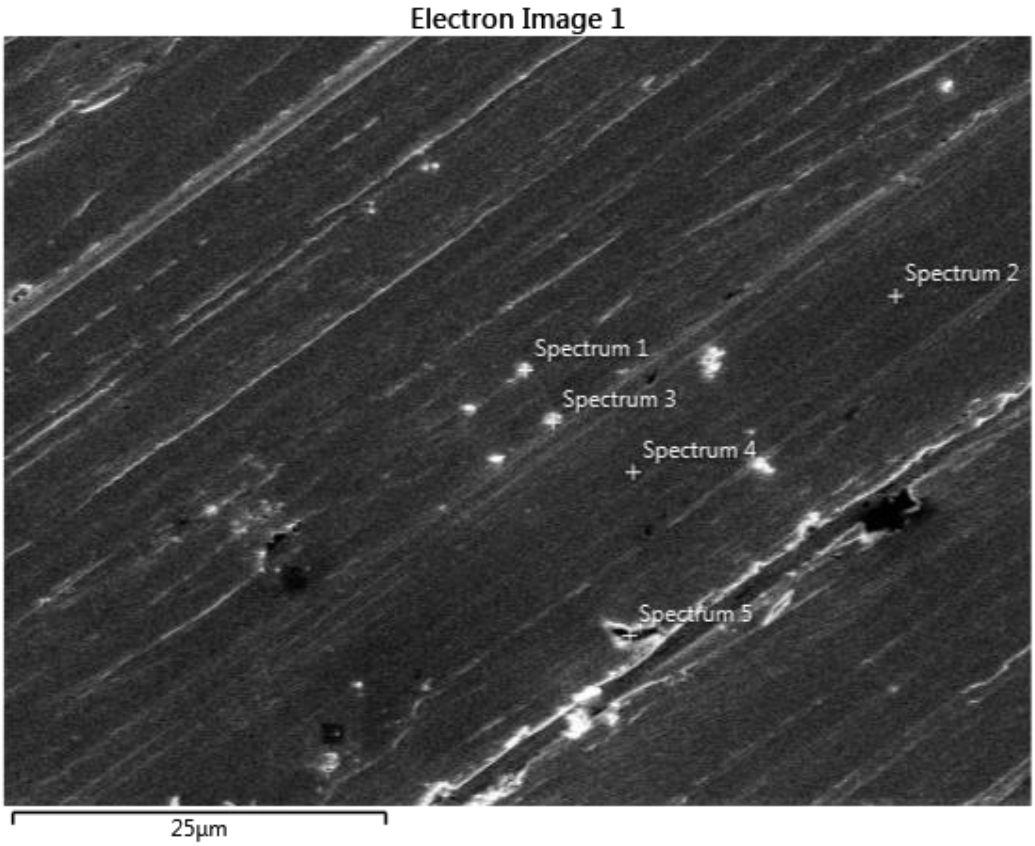

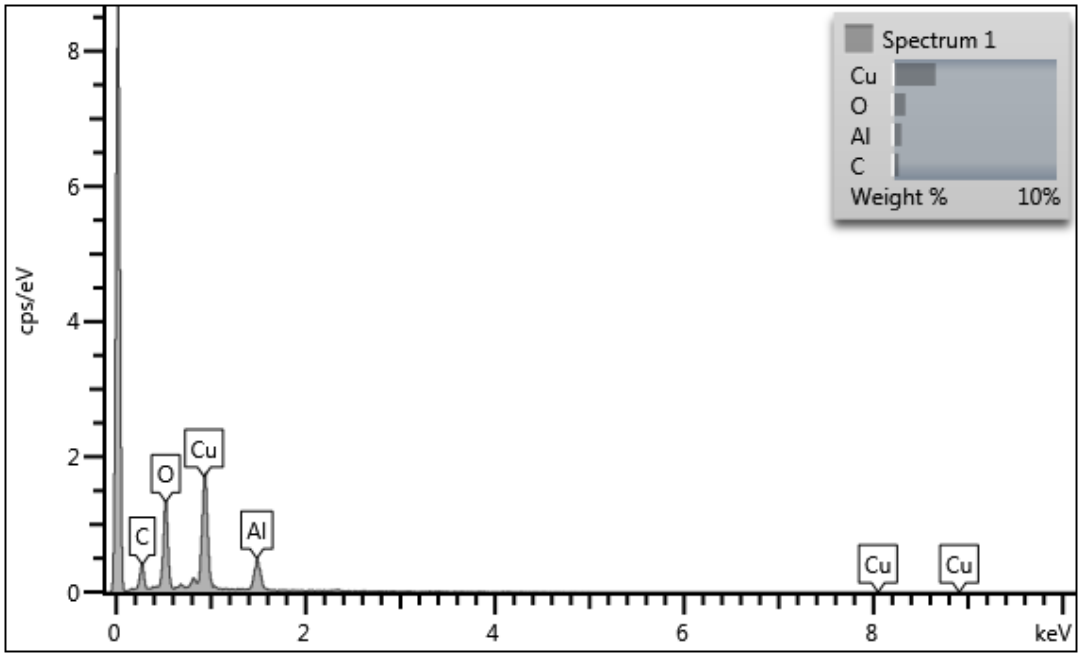

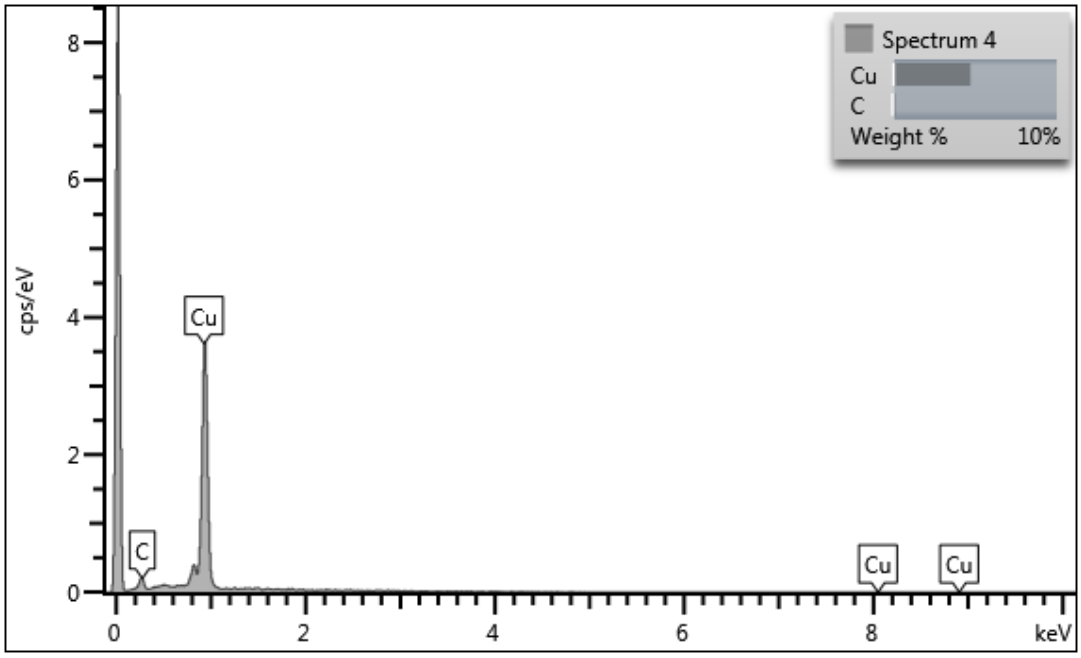

Alfa Aesar copper foil after annealing

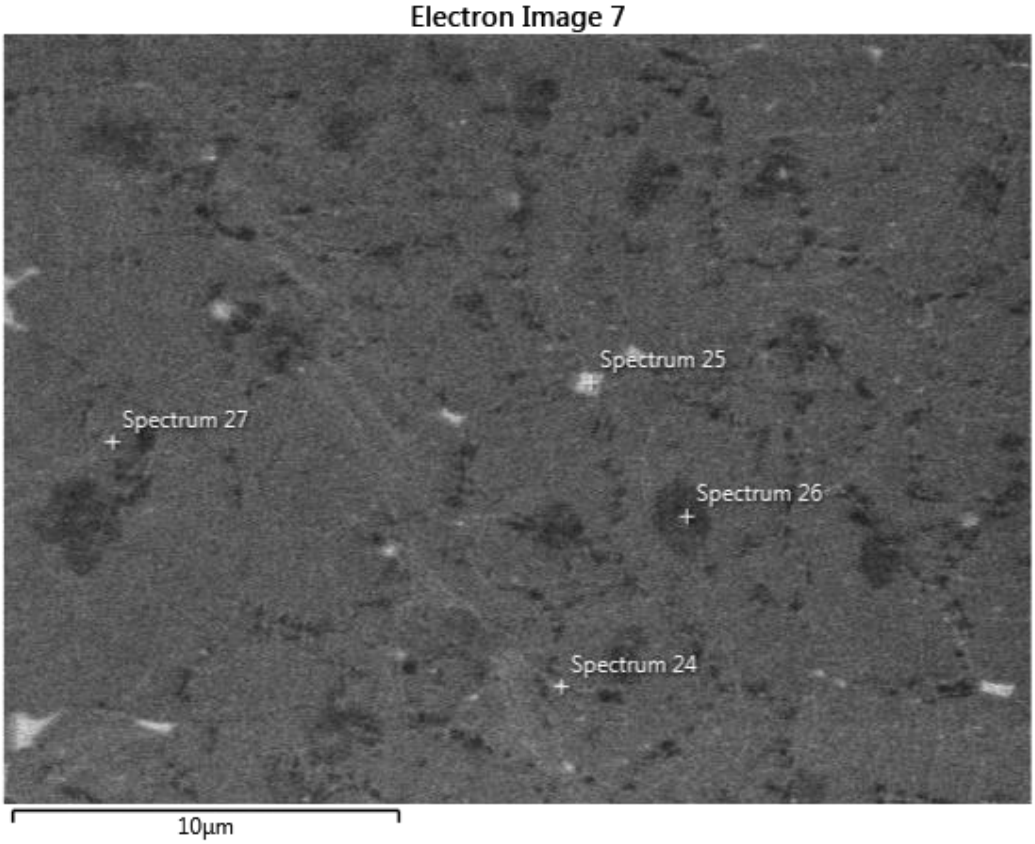

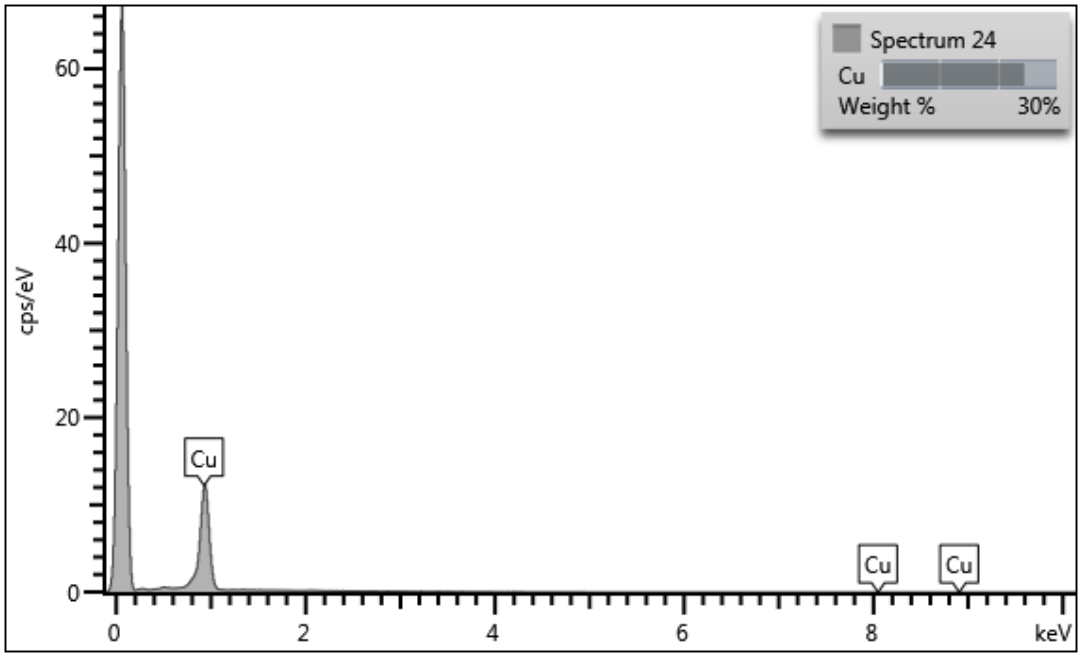

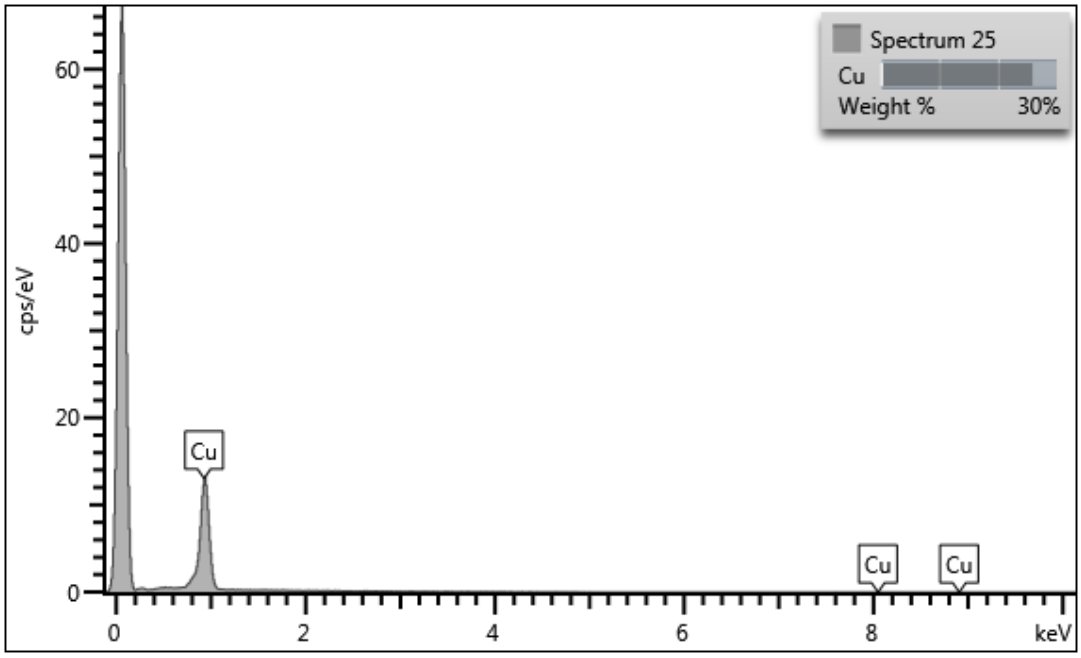

Appendix D

The Influence of a Transfer Process on the Strain and Doping Variation in Chemical Vapor Deposited Graphene

Microelectronic Engineering 121 (2014) 113–117

Contents lists available at ScienceDirect

Microelectronic Engineering

journal homepage: www.elsevier.com/locate/mee

Transfer induced compressive strain in graphene: Evidence from Raman spectroscopic mapping

Martin Benjamin B.S. Larsen *, David M.A. Mackenzie, José M. Caridad, Peter Bøggild, Timothy J. Booth

DTU Nanotech, Ørsteds Plads 345 B, Kgs. Lyngby 2800, Denmark

ARTICLE INFO

Article history:
Received 29 October 2013
Received in revised form 22 April 2014
Accepted 24 April 2014
Available online 5 May 2014

Keywords:
CVD graphene
Exfoliated graphene
Graphene transfer
Raman mapping
Cu catalysts
Comparison

ABSTRACT

We have used spatially resolved micro Raman spectroscopy to map the full width at half maximum (FWHM) of the graphene G-band and the 2D and G peak positions, for as-grown graphene on copper catalyst layers, for transferred CVD graphene and for micromechanically exfoliated graphene, in order to characterize the effects of a transfer process on graphene properties. Here we use the FWHM(G) as an indicator of the doping level of graphene, and the ratio of the shifts in the 2D and G bands as an indicator of strain. We find that the transfer process introduces an isotropic, spatially uniform, compressive strain in graphene, and increases the carrier concentration.

1. Introduction

Raman spectroscopy is a widely used technique for the non-destructive characterization of the properties of graphene [1,2]. The frequency, relative intensity, width, shape and position of characteristic peaks in the Raman spectrum of graphene provide information on the strain [4], doping [5] and presence of defects [3,6]. It is also possible to characterize the number of layers in the case of Bernal stacked graphene multilayers using the shape of the 2D peak [7]. The spatial variation of these properties can be mapped by scanning the excitation laser across the sample surface – this provides important information beyond that which can be obtained from single point spectra.

The interpretation of Raman spectra is complicated by the influence of the substrate supporting the graphene and the excitation energy used [1,7,8]. This is particularly relevant in the case of chemical vapor deposition (CVD) growth of graphene on metallic catalysts. In many practical applications, subsequent transfer of graphene to insulating substrates after growth is necessary. As it happens, variations in the Raman spectra obtained before and after transfer cannot immediately be ascribed to the influence of the particular substrate, to the effect of the transfer process or to the intrinsic properties of the graphene. Nevertheless, it would be useful to know the quality of graphene on insulator that can be expected from graphene on catalyst before transfer, and in particular whether the transfer process has a detrimental effect on the properties of the transferred graphene.

Here we use maps of the position of the 2D band and the G band, their shift direction and the full width at half maximum (FWHM) of the G band, in order to provide spatial information on the level of strain or doping in CVD grown graphene films on copper and transferred to oxidized silicon, and compare with mechanically exfoliated graphene layers on silicon dioxide.

2. Materials and methods

Graphene was deposited in an Aixtron 4-inch Black Magic CVD system. The process starts with a low temperature annealing step at 500 degrees C with 1000 sccm H_2 for 30 min and 25 mbar pressure, followed by a high temperature annealing step at 975 °C with the same gas flow rate and pressure. The system is then evacuated until a pressure of 0.5 mbar is reached and a CH_4 flowrate of 10 sccm for 5 min is introduced [3]. The catalyst substrate is a 4 inch silicon wafer with a 1 μm thick thermal oxide with a 1.5 μm thin sputtered copper layer on top; the copper deposition is done in a Polyteknik Cryofox physical vapor deposition system. Mechanically exfoliated graphene was produced following Refs [9,10]. The CVD graphene was transferred from the copper to a silicon wafer with a 90 nm SiO_2 layer, using electrochemical transfer [11].

The Raman characterization was carried out using a DXR Raman Microscope from Thermo Scientific, using three different excitation

* Corresponding author. Tel.: +45 4525 5788.
E-mail addresses: martin.larsen@nanotech.dtu.dk (M.B.B.S. Larsen), david.mackenzie@nanotech.dtu.dk (D.M.A. Mackenzie), peter.boggild@nanotech.dtu.dk (P. Bøggild), tim.booth@nanotech.dtu.dk (T.J. Booth).

http://dx.doi.org/10.1016/j.mee.2014.04.038
0167-9317/

lasers, with 445 nm, 532 nm and 633 nm wavelength using a 100× objective. Excitation lasers were exchanged without moving the sample in order to produce maps of nearly identical regions for each excitation.

Raman peaks from individual spatial points were fitted with a single symmetrical Lorentzian function plus a linear background, using a least-squares regression adapted from [12]. In this way the relative intensity of the peaks, position and full-width at half maximum can be plotted for each point of the sample surface. Due to the self-limiting nature of CVD fabrication of graphene on a copper catalyst, we do not expect changes in the shape of the 2D peak due to AB stacked multilayers.

We do not observe G peak splitting in our datasets due to low values of strain here ($\ll$0.3%) and the probable absence of uni-axial strain [14].

3. Results

Fig. 1 shows the FWHM(G) for each excitation wavelength and for the as-grown and transferred CVD graphene, as well as for mechanically exfoliated graphene. It can be seen that the FWHM(G) decreases after transfer of graphene from the catalytic growth substrate to an oxide layer (Fig. 1b–d vs. f–h). Small regions where FWHM(G) varies around 15 cm^{-1} indicate locally lower carrier concentrations for transferred graphene and exfoliated graphene (Fig. 1f–h and j–l). The FWHM(G) also shows comparable distribution for both transferred CVD graphene on oxide and exfoliated graphene. The measurements of the FWHM(G) for graphene on copper show broadening of the G band, particularly in the case of the 633 nm excitation (Fig. 1d).

Fig. 2 shows the shift in the 2D (ΔPos(2D)) and G (ΔPos(G)) positions. While the shift in the 2D and G bands vary around zero for CVD graphene on copper and exfoliated graphene (Fig 2a–c and j–l), transferred CVD graphene shows shifts towards larger wavenumbers for both the 2D and G bands (Fig. 2d–f and m–o). The shifts in the 2D and G band positions are notably more uniform for CVD graphene on SiO_2 than for CVD graphene on copper and for exfoliated graphene on oxide. These trends are independent of the excitation laser used.

The ratio ΔPos(2D)/ΔPos(G) of the peak shifts of 2D and G peaks is plotted in Fig. 3. Wide variation in this ratio is seen for CVD graphene on copper and exfoliated graphene – in the latter case distinct ridges are observed in the flake, which potentially correspond to wrinkles or folds (e.g. Fig. 3h). CVD graphene transferred to oxide shows a more uniform distribution of these values, and ΔPos(2D)/ΔPos(G) closer to ~2 (Fig. 3d–f).

Fig. 4 shows selected Raman spectra of neutral, doped, and strained regions on the same exfoliated graphene flake, at the indicated positions. The shift in the G and the 2D peaks indicated strain, but their intensities remain similar to that of neutral graphene. The doped graphene has a decreased 2D peak, while the G peak has narrowed compared to neutral graphene.

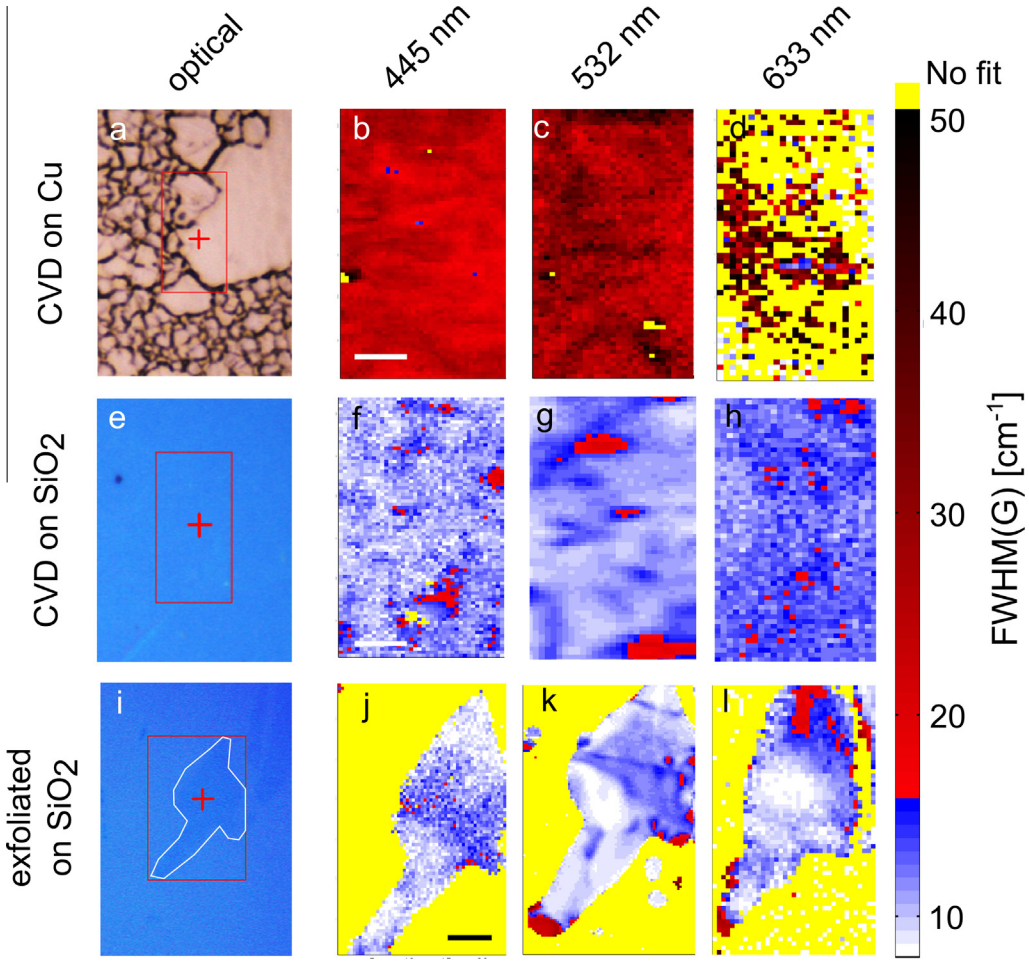

Fig. 1. Shows optical micrographs and the Raman FWHM(G) for CVD graphene on Cu (a–d), CVD graphene transferred to SiO_2 (e–h) and for exfoliated graphene on SiO_2 (i–l) for three different laser excitation wavelengths. The yellow color corresponds to no fitting, meaning no graphene or too poor signal to noise. The optical images as well as the Raman maps are collected with a 100× objective; the scale bars correspond to 5 μm. The map for CVD graphene on Cu is not considered due to poor signal to noise, but is added for consistency. (For interpretation of the references to color in this figure legend, the reader is referred to the web version of this article.)

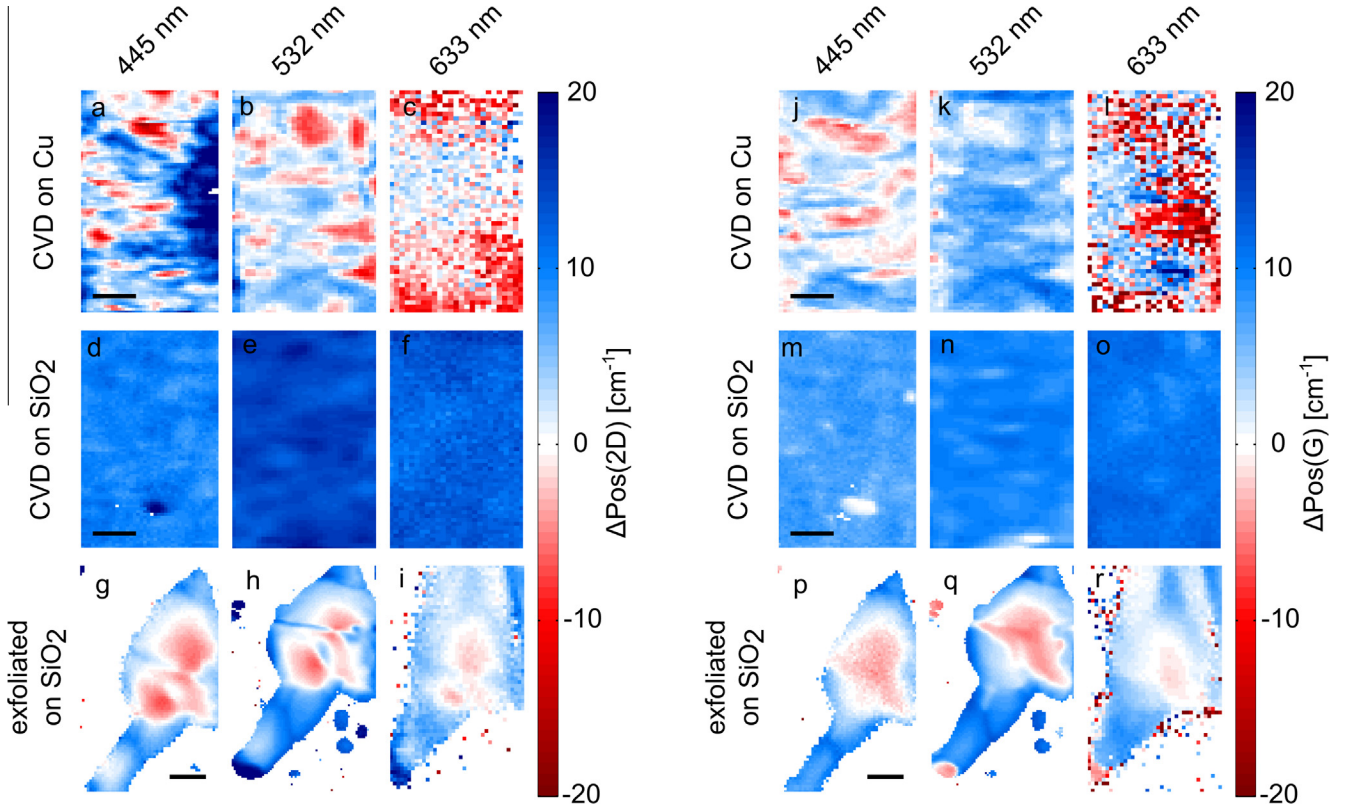

Fig. 2. Shows the relative shift in the 2D (a–i) and G (j–r) peak positions for CVD graphene on Cu, CVD graphene transferred to SiO_2 and exfoliated graphene on SiO_2. The shift is found as the measured values minus the theoretical values of 1588 cm^{-1} for the G peak and 2640 cm^{-1}, 2675 cm^{-1} and 2720 cm^{-1} for 445 nm, 532 nm, and 633 nm [13].

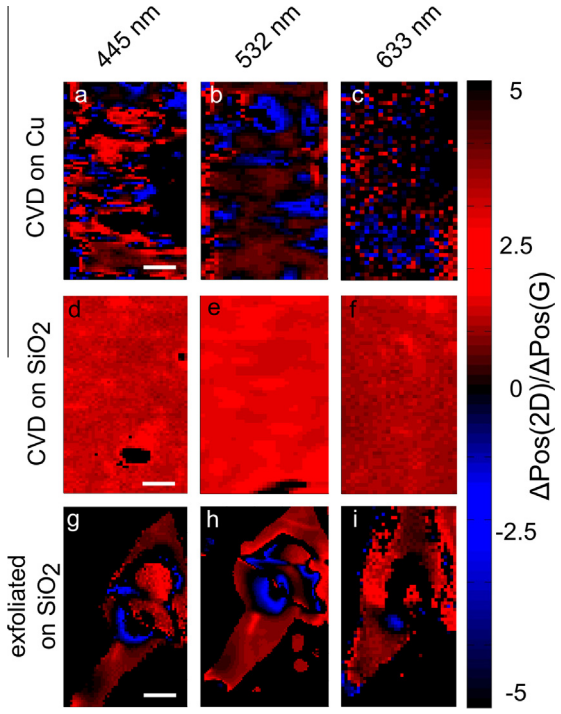

Fig. 3. Shows the ratio between the 2D peak shift and the G peak shift for CVD graphene on Cu(a–c), CVD graphene transferred to SiO_2(d–f) and exfoliated graphene on SiO_2(g–i) for the three laser wavelengths. The blue and red colors indicate regions of high strain, whereas the black regions indicate low to zero strain in the graphene films. The map for CVD graphene on Cu is not considered due to poor signal to noise, but is added for consistency. (For interpretation of the references to color in this figure legend, the reader is referred to the web version of this article.)

Poor signal to noise ratio in the 633 nm maps prevents adequate fitting of the peaks in the Raman spectra. We attribute the poor signal to noise to the fluorescence due to the interband transition in copper at around 650 nm [13]. Maps at the 445 nm and the 532 nm are indistinguishable within the spatial and spectral resolution of the spectrometer. The 445 nm laser shows higher sensitivity to DeltaPos(2D)/DeltaPos(G) for CVD graphene on Cu compared to the other two excitation energies.

In the case of CVD graphene transferred to SiO_2 there is no significant variation in the FWHM(G) for the three different excitation energies. The charge puddles are consistently seen with all of the lasers. Differences in the maps can be ascribed to the spatial resolution of the different excitation lasers. For CVD graphene transferred to SiO_2 we see a very similar level of strain with the 445 nm, the 532 nm and the 633 nm lasers, which we attribute to strain induced by the transfer process.

For exfoliated graphene on SiO_2 all three laser show the same tendencies of the FWHM(G), but the signal to noise combined with the poor resolution of the 633 nm laser makes this laser less suited for mapping due to the very long collection times and spatial resolution obtained. The strain observed in exfoliated graphene on SiO_2 is very similar for all three excitation energies.

4. Discussion

It is known that the doping level and the strain in graphene are reflected in changes of the 2D band and the G band from those expected for intrinsic graphene [4]. A FWHM(G) of ~15 cm^{-1} indicates carrier concentrations close to 0 [15], with a narrower FWHM of down to 8 cm^{-1} indicating greater doping. The 2D peak position enables the sign of the doping to be determined as well, since this peak upshifts in the case of hole doping, and downshifts for

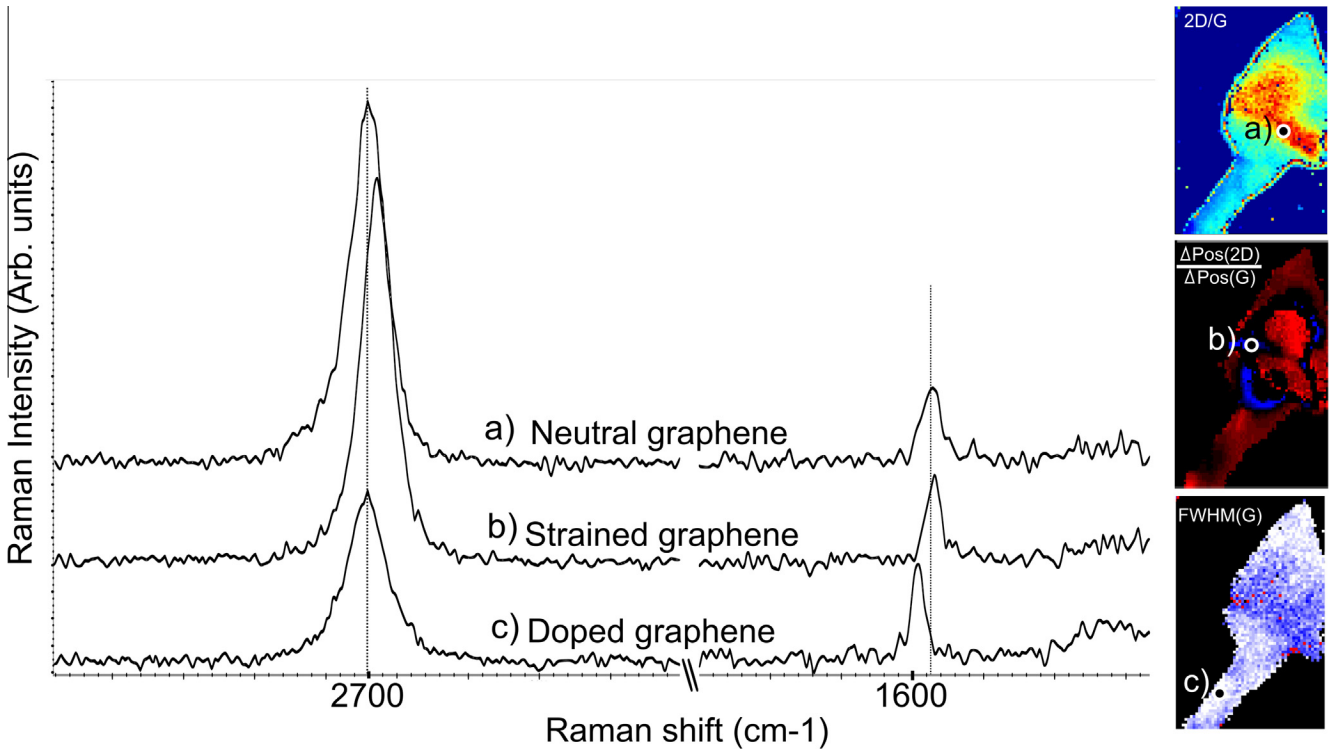

Fig. 4. Shows a raw spectrum of neutral graphene, doped graphene and strained graphene. The doped and strained spectra are extracted in regions where there is only one influence on the Raman spectrum, e.g. the strained graphene is not doped etc. The dotted lines are to guide the eye.

electron doping [5]. The effect of strain in suspended graphene has been also been studied – isotropic (biaxial) tensile strain results in downshifting of the G and 2D peaks, with the relative change in the position of the 2D and G bands of ~2 indicating strain rather than doping [4]. G-band splitting has been observed for uniaxial strains greater than ±0.3% [16], and a shift of this band to smaller or larger wavenumbers in the case of tensile or compressive strain respectively.

To summarize, where FWHM(G) is relatively small, doping is indicated, particularly where the ratio of the shifts is less than ~2. The 2D shift direction then indicates the type of doping. Where FWHM(G) is maximal, doping can be discounted, and the shifts in the 2D and G bands can be ascribed to strain. The ratio $\Delta 2D/\Delta G$ in this case should be ~2. The G shift direction then indicates whether the strain is tensile or compressive.

Our observations of the FWHM(G) show an overall decrease when CVD graphene is transferred to oxide. Exfoliated and transferred CVD graphene show similar micron scale "puddles" of lower carrier concentration. The FWHM(G) is distinctly wider for as-grown CVD graphene on copper, which likely represents the effects of charge transfer from the substrate. It is therefore not possible to ascribe the FWHM(G) wholly to the properties of the graphene in the case where it lies on a metal catalyst layer. The variation in the FWHM was similar between the exfoliated graphene and the CVD graphene on copper – however due to the uncertainties introduced by the substrate it is difficult to draw conclusions.

The Pos(2D) and Pos(G) for CVD graphene transferred to oxide both display less variation than is seen in CVD graphene on copper and exfoliated graphene. Additionally, the ratios of the band shifts, $\Delta Pos(2D)/\Delta Pos(G)$, also becomes more uniform and closer to ~2 for transferred CVD graphene. This indicates that the graphene peak variations observed originate from the effects of an isotropic strain introduced during the transfer process. This conclusion is supported by our observations of the $\Delta Pos(2D)/\Delta Pos(G)$ for exfoliated graphene, which show values close to ~2 around wrinkles, corresponding to high strain. CVD graphene grown on Cu and exfoliated graphene have similar variations in $\Delta Pos(2D)/\Delta Pos(G)$ over a few μm^2. The strain in exfoliated graphene is a result of the fabrication process – the strain in CVD graphene on copper results from the roughness of the copper surface and from the different thermal expansion coefficients of graphene and copper (Fig. 1a). Since the 2D and G peaks shift to larger wavenumbers and the ratio of these shifts is ~2, we can determine that our transfer process leads to compressive straining of the graphene.

Thus, either during the CVD growth or transfer process a uniform compressive strain is induced on the CVD graphene transferred to a SiO_2 substrate. A further study has to be undertaken to decide whether this bi-axial strain is induced by the growth or the transfer process.

5. Conclusions

We have used spatially resolved Raman spectroscopy to map the full width at half maximum of the graphene G-band and the 2D and G peak positions, for as-grown graphene on copper catalyst layers, for transferred CVD graphene and for micromechanically exfoliated graphene, in order to characterize the effects of a transfer process on the strain and doping level of graphene.

In general, it is challenging to distinguish between strain and doping in graphene using Raman spectroscopy *a priori* without explicitly introducing these through e.g. mechanical deformation or electrostatic gating. Additionally both strain and doping can vary spatially simultaneously. Here we use the FWHM(G) as an indicator of the doping level of graphene, and the ratio of the shifts in the 2D and G bands as evidence of strain.

We find that the transfer process introduces an isotropic compressive strain in graphene, which is also spatially uniform. Whilst this strain is mostly an undesirable property, the observed

homogeneity could be an advantage in the production of devices where consistency over several hundred μm^2 is more important than having better but inconsistent electronic characteristics.

Relatively low carrier concentrations were observed for CVD graphene on copper, as evidenced by the FWHM(G). However, the transfer process had the effect of significantly increasing the doping level, as determined by a narrowing of the FWHM of the G-peak. However, the resulting doping level was consistent with the average level of doping in graphene exfoliated on identical oxide substrates. Both exfoliated and transferred CVD graphene showed similar several micron wide "puddles" of low doping which were similar to doping levels seen on CVD graphene on Cu. In fact, transferred graphene shows a generally lower doping than exfoliated graphene here, as evidenced by a FWHM(G) closer to 15 cm^{-1} in more areas.

The non-destructive mapping of properties of graphene is important as a control of quality and process consistency at each step of a graphene device production. The Raman spectrum of as-grown graphene on copper should not be considered to be representative of same graphene after transfer to oxidized silicon. Knowledge of the spatial variation of the doping and strain in CVD graphene over large areas will help to increase the consistency and reliability of the resulting devices produced. It is critical that the spatial variation of these properties is considered – point spectra are not adequate for complete characterization of the graphene quality, not even of single crystalline graphene.

Appendix A. Supplementary data

Supplementary data associated with this article can be found, in the online version, at http://dx.doi.org/10.1016/j.mee.2014.04.038.

References

[1] Sara D. Costa, Ariete Righi, Cristiano Fantini, Yufeng Hao, Carl Magnuson, Luigi Colombo, Rodney S. Ruoff, Marcos A. Pimenta, Solid State Commun. 152 (2011) 1317–1320.
[2] L. Tao, J. Lee, M. Holt, H. Chou, S.J. McDonnell, D.A. Ferrer, M.G. Babenco, R.M. Wallace, S.K. Banerjee, R.S. Ruoff, et al., J. Phys. Chem. C 116 (2012) 24068–24074.
[3] P. Klar, E. Lidorikis, A. Eckmann, I.A. Verzhbitskiy, A.C. Ferrari, C. Casiraghi, Phys. Rev. B 87 (2013) 205435.
[4] Jakob Zabel, Rahul R. Nair, Anna Ott, Thanasis Georgiou, Andre K. Geim, Kostya S. Novoselov, Cinzia Casiraghi, Nano Lett. 12 (2012) 617–621.
[5] C. Casiraghia, S. Pisana, K.S. Novoselov, A.K. Geim, A.C. Ferrari, Appl. Phys. Lett. 91 (2007) 233108.
[6] Ado. Jorio, Erlon H. Martins Ferreira, Luiz G. Cançado, Carlos A. Achete, Rodrigo B. Capaz, Measuring disorder in graphene with Raman spectroscopy, in: Sergey Mikhailov (Ed.), Physics and Applications of Graphene – Experiments, InTech, 2011 (ISBN: 978-953-307-217-3).
[7] A.C. Ferrari, Solid State Commun. 143 (2007) 47–57.
[8] K. Sato, R. Saito, Y. Oyama, J. Jiang, L.G. Cancado, M.A. Pimenta, A. Jorio, Ge.G. Samsonidze, G. Dresselhaus, M.S. Dresselhaus, Elsevier Sci. 427 (1–3) (2006) 117–121.
[9] K.S. Novoselov, A.K. Geim, S.V. Morozov, D. Jiang, Y. Zhang, S.V. Dubonos, I.V. Grigorieva, A.A. Firsov, Science 306 (2004) 666.
[10] K.S. Novoselov, D. Jiang, F. Schedin, T.J. Booth, V.V. Khotkevich, S.V. Morozov, A.K. Geim, Proc. Natl. Acad. Sci. 102 (2005) 10451.
[11] Libo Gao, Wencai Ren, Xu Huilong, Li Jin, Zhenxing Wang, Teng Ma, Lai-Peng Ma, Zhiyong Zhang, Fu Qiang, Lian-Mao Peng, Xinhe Bao, Hui-Ming Chenga, Nat. Commun. 3 (2012) 699.
[12] Tom O'Haver. Peak Fitter. www.mathworks.com/matlabcentral. 09 Apr 2009 (Updated 13 Sep 2013).
[13] L.M. Malarda, M.A. Pimentaa, G. Dresselhausb, M.S. Dresselhaus, Phys. Rep. 473 (5–6) (2009) 51–87.
[14] H. Ehrenreich, H.R. Philipp, Phys. Rev. 128 (4) (1962).
[15] Simone Pisana, Michele Lazzeri, Cinzia Casiraghi, Kostya S. Novoselov, A.K. Geim, Andrea C. Ferrari, Francesco Mauri, Nat. Mater. 6 (2007).
[16] T.M.G. Mohiuddin, A. Lombardo, R.R. Nair, A. Bonetti, G. Savini, R. Jalil, N. Bonini, D.M. Basko, C. Galiotis, N. Marzari, K.S. Novoselov, A.K. Geim, A.C. Ferrari, Phys. Rev. B 79 (2009) 205433.

Appendix E

Copper Mass Loss

Copper mass change measured on a high precision scale. The measurements are carried out before and after graphene growth in the Black Magic CVD system.

#	Mass change mg	Mass change %
1	0.36	100.002
2	-1.22	99.994
3	-1.25	99.994
4	-1.03	99.995
5	-0.36	99.998
6	-0.35	99.998
7	-1.63	99.992
8	0.42	100.002
9	-0.72	99.996
10	-6.28	99.970
11	-0.39	99.998
12	-3.05	99.985
13	-1.09	99.995
14	-0.28	99.999
15	-0.26	99.999
16	-0.52	99.997
17	-0.33	99.998
18	-0.57	99.997
19	-1.66	99.992

Table E.1: Table showing the change in copper mass after CVD processing of graphene. Wafer 1 and 8 show an increased mass after processing, possibly due to poor calibration of the scale (an actual increase in mass is implausible). The average mass loss is 1.1 mg corresponding to 1.1% of the copper lost to evaporation.

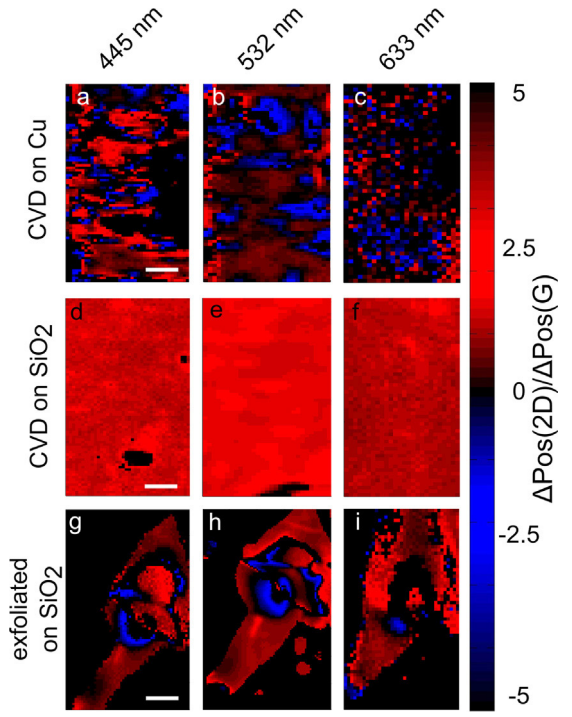

Published by:
DTU Nanotech
Department of Micro- and Nanotechnology
Technical University of Denmark
Ørsteds Plads, building 345B
DK-2800 Kgs. Lyngby